Oxidative Chemical Vapor Deposition of Semiconducting Polymers and Their Use In Organic Photovoltaics

By

David Christopher Borrelli

M.S. Chemical Engineering Practice
Massachusetts Institute of Technology, Cambridge, MA, 2011

B.S. Chemical Engineering
University of Rochester, Rochester, NY, 2009

SUBMITTED TO THE DEPARTMENT OF CHEMICAL ENGINEERING IN PARTIAL
FULFILLMENT OF THE REQUIREMENTS FOR THE DEGREE OF

DOCTOR OF PHILOSOPHY IN CHEMICAL ENGINEERING

AT THE

MASSACHUSETTS INSTITUTE OF TECHNOLOGY

JUNE 2014

Signature redacted

Signature of Author: _____

Department of Chemical Engineering
May 15, 2014

Signature redacted

Certified by: _____

Karen K. Gleason
Professor Chemical Engineering
Thesis Supervisor

Signature redacted

Accepted by: _____

Patrick S. Doyle
Professor of Chemical Engineering
Chairman, Committee for Graduate Students

Oxidative Chemical Vapor Deposition of Semiconducting Polymers and Their Use In Organic Photovoltaics

by

David Christopher Borrelli

Submitted to the Department of Chemical Engineering
on May 15, 2014, in Partial Fulfillment of the Requirement for the Degree of
Doctor of Philosophy in Chemical Engineering

Abstract

Organic photovoltaics (OPVs) have received significant interest for their potential low cost, high mechanical flexibility, and unique functionalities. OPVs employing semiconducting polymers in the photoactive layer have traditionally been fabricated almost exclusively with solution-based techniques due to a lack of suitable alternatives. This has thus limited polymer solar cells and other polymer electronic devices to using polymers that are soluble.

Here we explore the use of oxidative chemical vapor deposition (oCVD), a vacuum-based method, for the deposition of semiconducting polymers. Polymer deposition by oCVD occurs at moderate vacuum (~0.1 Torr) and low temperature (25 – 150 °C). oCVD offers the well-cited processing benefits of vacuum processing, including parallel and sequential deposition, well-defined thickness control and uniformity, and inline integration with other standard vacuum processes (e.g. vacuum thermal evaporation).

Various semiconducting polymers, including insoluble polymers that are difficult to process using conventional methods, are successfully deposited via oCVD by changing the monomer precursor. The optoelectronic properties of unsubstituted polyisothianaphthene (PITN) and unsubstituted polythiophene (PT) are first investigated under various oCVD deposition conditions. Higher stage temperatures are shown to increase conjugation in PITN films, resulting in a significant red-shift in the absorption spectrum and a decrease in the optical bandgap from 1.14 to 1.05 eV. The effects of oCVD chamber pressure on the properties of PT are then investigated. Higher chamber pressures are found to correlate with greater conjugation, increased absorption, and larger field effect mobilities in PT films. oCVD PT films are then successfully integrated into planar heterojunction OPVs as the electron donor layer, achieving power conversion efficiencies up to 0.8%. Several alternative device architectures are investigated as means to improve OPV device performance. Promisingly, a ternary energy cascade device architecture is shown to more than double the OPV device performance to over 2%.

Thesis Supervisor: Karen K. Gleason
Title: Professor of Chemical Engineering

Acknowledgments

I am truly grateful to the entire Organic Nanostructured Electronics Lab. Aside from providing me with access to unique equipment for fabricating and testing organic photovoltaic devices, it also served as a meeting ground for new colleagues, collaborators, and friends. I am especially thankful for help from Patrick Brown, Joel Jean, and Jill Macko for equipment training and maintenance and answering my many questions. I would also like to thank Trisha Andrew, Andrea Maurano, and Geoffrey Supran for help with various lab techniques. Additional thanks go to Apoorva Muraka, Farnaz Niroui, and the rest of the ONE lab for keeping everything running smoothly and being great company in lab. By extension, I'd also like to thank Sehoon Chang for significant effort on various attempted collaborations during my thesis research.

I would also like to thank the MIT staff who have helped make things run smoothly and helped me through many administrative hurdles, especially Gwen Wilcox and Stephen Wetzel.

My family and friends provided much-appreciated support through this entire process. I'm especially grateful to my parents, Thomas and Mary Ann Borrelli, for instilling in me a determination to succeed, a tireless work ethic, and a passion for learning. My siblings, Andrea and T.J. Borrelli, my grandparents and the rest of my family were a constant source of encouragement. I am especially thankful to Alison Schultz for her unwavering support, encouragement, and cheerfulness throughout this process. I'd also like to thank my ChemE classmates and friends for keeping life entertaining.

Finally, I dedicate this thesis and the decades of work it embodies to my Mother.

Table of Contents

7

9

List of Figures

13

List of Tables

List of Abbreviations

BCP	bathocuproine
BHJ	bulk heterojunction
E_g	band gap energy
EQE	external quantum efficiency
$FeCl_3$	iron(III) chloride
FF	fill factor
HOMO	highest occupied molecular orbital
ITO	indium tin oxide
J_{SC}	short circuit current density
LUMO	lowest unoccupied molecular orbital
oCVD	oxidative chemical vapor deposition
OPV	organic photovoltaic
P3HT	poly(3-hexylthiophene)
PCBM	6,6-phenyl C_{61}-butyric acid methyl ester
PCE	power conversion efficiency
PEDOT	poly(3,4-ethylenedioxythiophene)
PITN	poly(isothianaphthene)
PM-HJ	planar-mixed heterojunction
PT	polythiophene
UV-vis	ultraviolet-visible spectroscopy
V_{oc}	open circuit voltage

Chapter 1

Introduction

1.1 Motivation

The increasing threat of climate change and the tremendous potential of the solar resource has resulted in intense research efforts on photovoltaic technologies. A vast array of photovoltaic technologies have consequently emerged, each with their own advantages and disadvantages. Organic photovoltaics (OPVs) have been of great interest due to their potential low cost, high mechanical flexibility, wide array of functionalities, and well-understood structure-composition-property relationships.[1-4] They can also provide unique properties, such as being highly transparent in the visible part of the solar spectrum,[5, 6] for new applications.

OPVs are fabricated with active layers consisting of conjugated molecules ranging in size from low molecular weight small molecules to long semiconducting polymer chains. Despite different processing methods and materials, both solution-printed polymer solar cells and vacuum-deposited small molecule organic solar cells have independently reached record certified efficiencies of over 10% despite,[7, 8] through careful materials selection and device architecture engineering. Although small molecule organics can be processed both in solution and with thermal evaporation, polymers for photovoltaic applications have traditionally been deposited almost exclusively with solution-based techniques. The high temperatures necessary to physically deposit polymers by vacuum thermal evaporation leads to polymer degradation,[9] limiting materials to low-molecular-weight organics. Instead, polymers are cast from a solution, which requires the addition of solubilizing side chains. For example, unsubstituted polythiophenes are intractable and insoluble in all solvents except mixtures of arsenic trifluoride and arsenic pentafluoride.[10] However, poly(3-hexylthiophene), a popular derivative of PT, is soluble in chlorinated solvents such as chloroform, chlorobenzene, and 1,2-dichlorobenzene.[11] Significant effort is aimed at structurally modifying monomer molecules or synthesizing new monomer precursors to make the resulting polymers soluble in commonly-used solvents. However, the use of solvents also raises

concerns over solvent toxicity and compatibility between the solvent and substrate so as to not damage or dissolve the substrate. Additionally, solution-processing typically requires that the electron donor and electron acceptor materials are both sufficiently soluble in the same solvent.

These difficulties may be overcome by depositing polymer thin films directly from the vapor phase, as solubility of the conjugated polymer is no longer required. This can be accomplished using chemical vapor deposition (CVD). In general, CVD processes employ vapor phase precursors that chemically react at a surface to generate a thin, solid film. This method is widely used in the semiconductor industry and is considered to be scalable from bench to plant.[12] CVD offers many advantages to the field of organic photovoltaics. The film properties can be easily and systematically tuned by changing the deposition conditions and composition of the feed gas. Vapor deposition of polymers by CVD can also provide the unique ability to conformally coat micro- and nano-scale surface features, which is not possible with solution methods because of the surface tension inherent in liquid-phase systems.[12] Uniform coatings over large areas can be achieved by controlling the gas flow profiles. Additionally, CVD allows for the deposition of insoluble polymers, which are believed to be more stable for organic electronic device applications.[13, 14]

Different CVD variants have been used to deposit several different conjugated polymers, including polyphenylenes,[15, 16] polyacetylenes,[17] polyanilines,[18, 19] polyimides,[20] polypyrroles,[21, 22] and polythiophenes.[23, 24] In most published studies the polymers' electronic properties were measured, but they were not used in OPVs. Additionally many of the CVD techniques used require high temperatures or high energy input to activate the monomer precursors. Prior to the work performed in this thesis, only two published studies existed that used vapor-deposited polymers were in OPVs. Poly(isothianaphthene-3,6-diyl) was deposited by heating 3,4-

diethynylthiophene,[25] and plasma polymerization was used to deposit poly(acrylonitrile).[26] In both cases very high temperatures (500°C -700°C) were required for deposition of polymers with adequate properties, and the OPV efficiencies were less than $10^{-4}\%$.

1.2 Oxidative Chemical Vapor Deposition

Oxidative chemical vapor deposition (oCVD) offers a potential link between many of the above considerations by enabling the effective deposition of conjugated polymers from vapor phase precursors. In oCVD, both the monomer and oxidant are delivered to the substrate surface in the vapor phase in a single step, resulting in the simultaneous synthesis and deposition of polymer films on the substrate. This is performed at low temperature (25–100 °C) and moderate vacuum (~0.1 Torr). A standard oCVD process involves placement of the substrate inside a vacuum chamber onto an inverted, temperature-controlled stage. Iron(III) chloride, a solid state oxidant at room temperature, is placed in a crucible directly inside the vacuum chamber oriented upward at the inverted stage and heated to a high temperature (~320 °C) to sublime it.[27] The monomer, frequently in liquid form, is placed in a heated vacuum jar and fed into the system through a heated line at a controlled flow rate. The operating pressure during deposition is often maintained using a butterfly valve.

The polymerization process is believed to proceed via step-growth polymerization. An oxidizing agent first oxidizes an aromatic heterocyclic monomer to form a radical cation. Contact between two radical cations then results in the formation of a dimer. This process then repeats and the polymer chain grows through step-growth polymerization. Figure 1-1 shows the oCVD reaction pathway for poly(3,4-ethylenedioxythiophene) (PEDOT). Over-oxidation of the polymer chain results in a doped, conductive film.
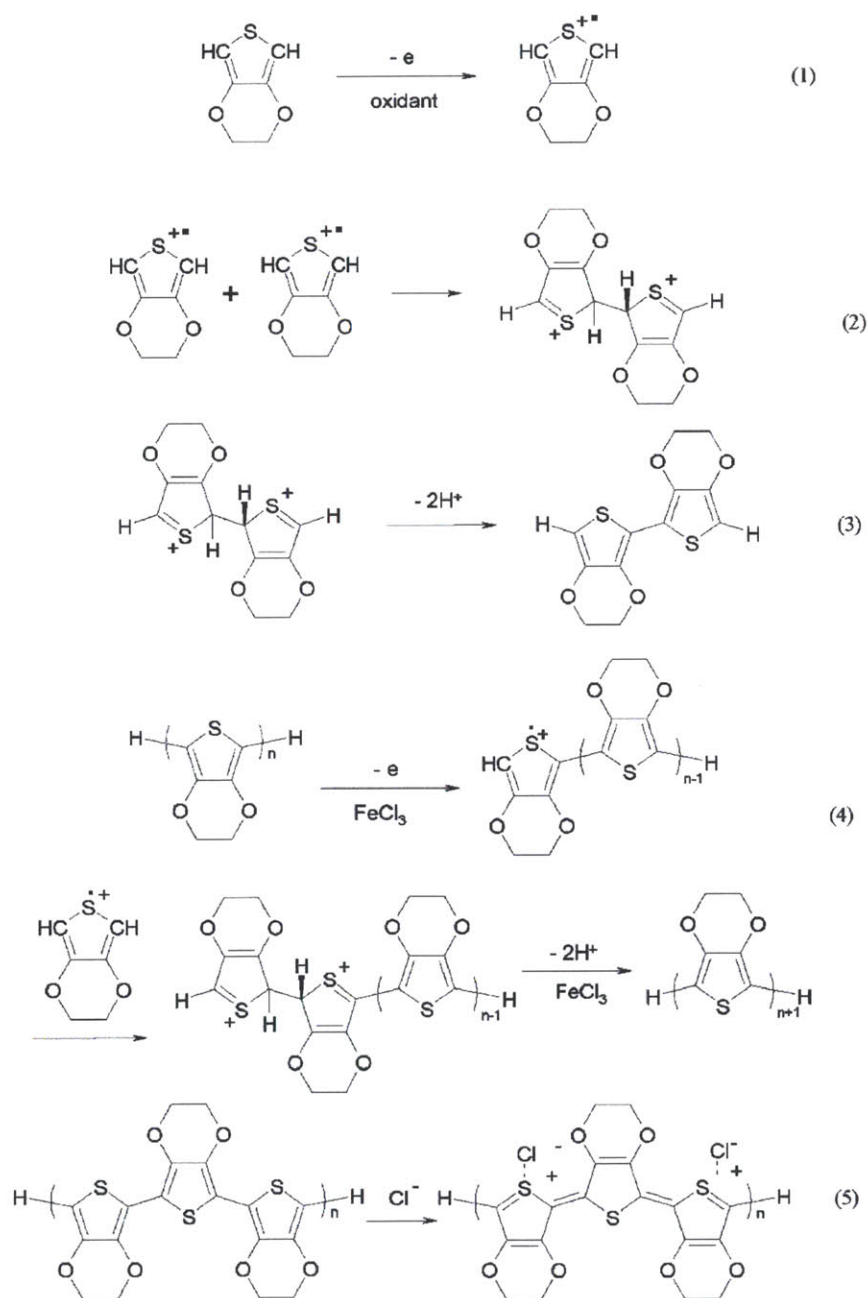
Figure 1-1. PEDOT polymerization mechanism. (1) oxidation of EDOT to form cation radicals; (2) dimerization of cation radicals; (3) deprotonation to form conjugation; (4) further polymerization from n-mer to (n+1)-mer; (5) doping of PEDOT. Reprinted with permission from Ref [27]. Copyright 2007 American Chemical Society.

Previous work has focused on using oCVD for depositing conducting polymers, such as PEDOT, often for electrodes in organic electronics.[28, 29] Many other conjugated homo- and co-polymers have also been successfully deposited by oCVD, as summarized in Table 1-1.

21

Table 1-1. Summary of oxidants and monomers used in oCVD, including those from this thesis.[30]

Oxidants	Monomers
Iron (III) chloride	EDOT
Iron (III) p-toluenesulfonate or iron (III) tosylate	Pyrrole
Copper (II) chloride	3-thiophene acetic acid
Bromine	3-thiopheneethanol
Vanadium oxytrichloride	Selenophene
	Thiophene
	1,3-Dihydroisothianaphthene

Organic electronic device applications of polymer thin films often require patterning the films in certain geometries. Patterning is readily achieved in oCVD by shadow masking the substrates during the deposition process, as shown in Figure 1-2.
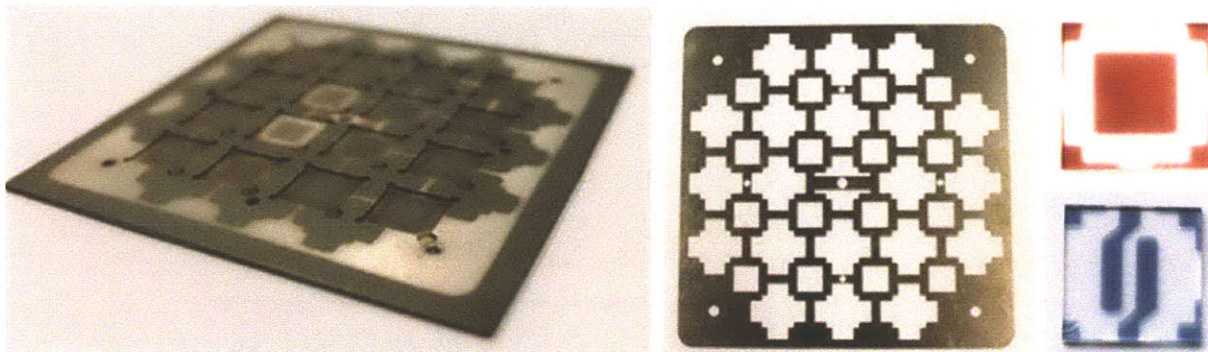
Figure 1-2. (left) Sample holder for 0.495 x 0.495 in^2 substrates. **(middle)** Example mask for photoactive layer. **(right)** oCVD Polythiophene (red) patterned on a glass substrate using the shown shadow mask and oCVD PEDOT (blue) patterned with an electrodes mask (not shown).

Effective deposition of polymers on nonplanar substrates is critical for many applications, such as when high surface areas are needed. The ability to achieve conformal coatings on micro- and nano-structured surfaces by solution-based coating techniques, such as spin coating and dip coating, are limited by wetting effects. The nonconformal coating from solution-based processes often results from the solvent flowing due to the action of gravitational forces as well as solvent surface tension. In contrast, oCVD is conformal over nonplanar substrates, enabling compatibility

with substrates such as paper and textiles.[28] Additionally, this could result in improved device performances from better coverage of high-surface-area substrates (Figure 1-3).
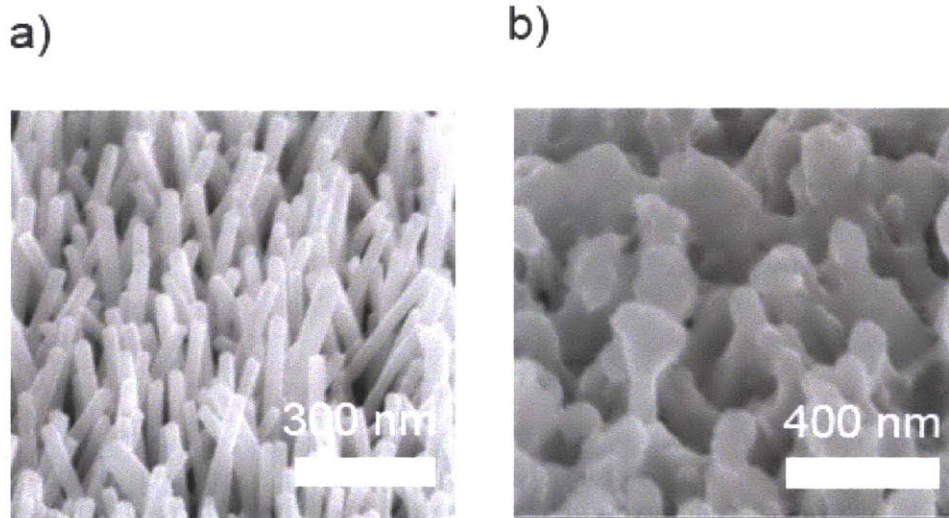
Figure 1-3. (a) ZnO nanowires. **(b)** ZnO nanowires coated with oCVD PT, demonstrating conformal polymer coverage. Images courtesy of Sehoon Chang.

1.3 Semiconducting Polymers via oCVD

The reaction conditions in the oCVD process typically result in over-oxidation of the deposited polymer, producing a conductive polymer film. These conductive polymers have been successfully used for numerous applications, including as transparent conductive electrodes for organic photovoltaics.[28, 29] A major finding of this thesis is that a dedoping step can be used to obtain useful semiconducting polymers deposited by oCVD. Dedoping is typically characterized by a noticeable change in color of the film between the doped and neutral states (Figure 1-4), in addition to other optoelectronic changes.
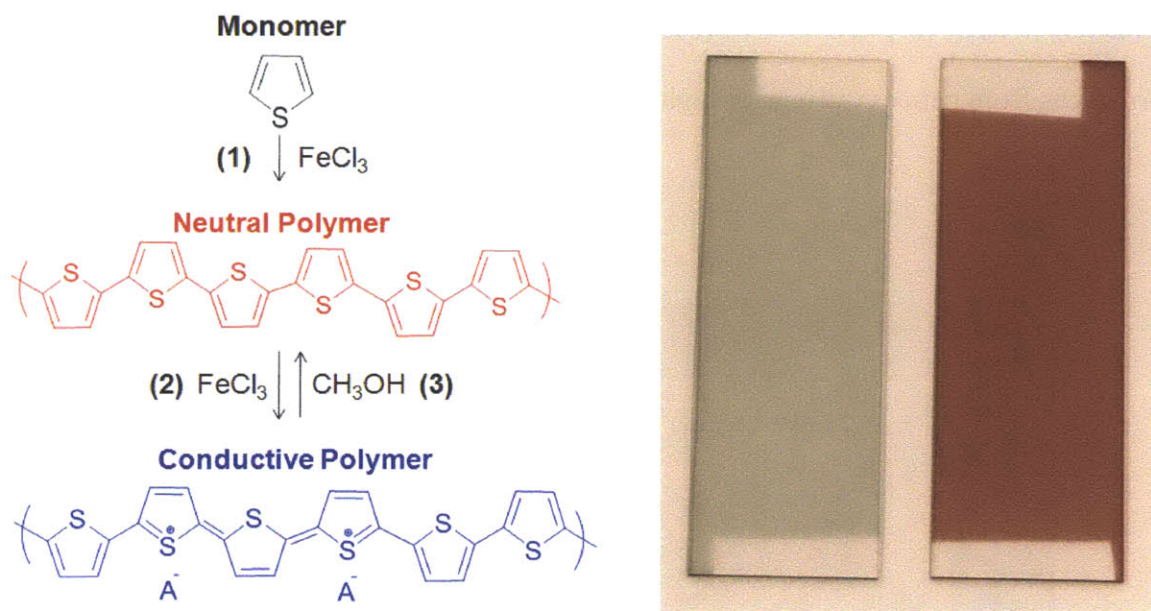
Figure 1-4. (Left) Chemical structures of unsubstituted polythiophene at the various steps of the oCVD process. Steps (1) and (2) occur during oCVD to overoxidize the films. Rinsing the films in methanol to dedope them results in recovery of the neutral form (3). **(Right)** Doped (blue) and undoped (red) polythiophene film on 2.5 x 7.6 cm^2 glass.

Most of the previous oCVD work focused on PEDOT or copolymers of EDOT with other monomers. It is very difficult to chemically dedope PEDOT that is p-doped, even with strong reducing agents such as hydrazine.[31] This is because the oxygen atoms have significant stabilizing effects on the positive charges, making the doped form of PEDOT very stable.[32] On the other hand, many other conjugated polymers can be easily dedoped.

In the solution-polymerization of semiconducting polymers, reducing agents are routinely used to dedope the polymers that become doped from reactants used for polymerization. The most common reducing agents are hydrazine[33] and ammonia[34] but alcohols, such as methanol[35] and ethanol,[36] have also been used. Alternatively, heat treatment can also dedope polymers. Poly(3-octylthiophene) doped with FeCl$_4^-$ has been shown to release Cl$_2$ upon heating to form neutral polymer.[37] However, thermally dedoping poly(3-alkylthiophenes) was observed to be associated

with polymer degradation.[38] For the oCVD films, methanol typically sufficiently dedoped the polymers.

Given the versatility of the oCVD technique, numerous semiconducting polymers can easily be deposited by changing the monomer used. However, much of this thesis work focuses on unsubstituted polymers that are normally difficult to process into films by conventional methods. Particular emphasis is placed on unsubstituted polythiophene (PT) since polythiophenes have received significant interest for their use in organic electronics.[1, 39, 40] Poly(3-hexylthiophene) (P3HT), a soluble derivative of PT, is especially popular for organic photovoltaics and is very well-studied.[41] In contrast, much less is known about PT and thus investigation of oCVD PT film properties is valuable.

PT films have been prepared by many methods, including electropolymerization,[42-45] thermo-cleavage of solubilizing side chains[13, 14] and various vapor-phase methods such as plasma polymerization[23, 46] and others.[22, 24, 47, 48] Chemical polymerization in solution or solid form is possible,[49, 50] but this results in polymer powders that are difficult to apply to organic electronics, which require polymer films. Since most polymer solar cells are solution-processed, PT's insolubility has limited its use in OPVs. Attempts at using PT electrodeposited directly onto electrodes resulted in efficiencies of 0.1% or less.[51, 52] Photoelectrochemical cells of polythiophene homo- and co-polymers yielded efficiencies less than 0.02%.[53, 54] A more successful approach to using PT in OPVs has been carried out by forming a bulk heterojunction of PCBM with poly-(3-(2-methylhexan-2-yl)-oxy-carbonyldithiophene) (P3MHOCT), which is a soluble derivative of PT. After the film was spin-coated onto the electrode, it was heated to above 300 °C to thermally cleave the side chains to leave unsubstituted PT.[55] Efficiencies up to 0.6% and 1.5% were obtained PC$_{60}$BM and PC$_{70}$BM, respectively.[56] A similar approach was taken with tandem cells, although

the efficiencies were much lower.[57] A roll-to-roll production process was also demonstrated using this process with device efficiencies less than 0.3%.

1.4 New oCVD Reactor

During the course of my research, I designed and constructed a new oCVD reactor as shown in Figure 1-5. Design details for the reactor can be found in Appendix A.

Figure 1-5. (Left) Full reactor setup. The valves and heaters are controlled through the computer control system on the left. Underneath the chamber are various controllers for the evaporation sources, butterfly valve, and turbopump. **(Right)** Inside of the new oCVD chamber. The inverted stage on the top is able to rotate. There are four evaporation sources on the bottom, each with its individual shutter (shown open).

By using this new reactor that is equipped with a rotating stage, it was possible to obtain much more uniform films over large areas, as shown below:
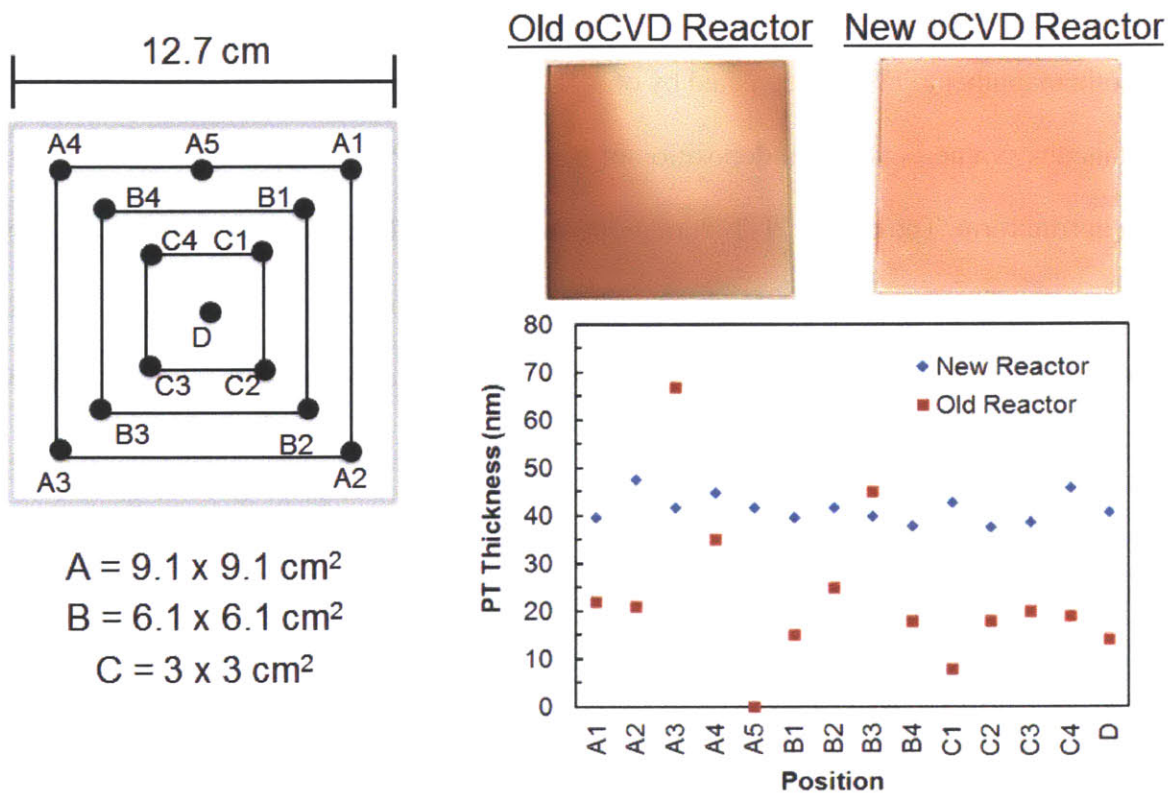
Figure 1-6. Comparison of the uniformity of film thickness of oCVD polythiohene on 12.7 x 12.7 cm2 glass slides in the old and newly built oCVD reactor. The rotating stage in the new reactor results in much improved uniformity.

This new chamber and evaporation sources greatly improved the control and reproducibility of the oCVD depositions. Additionally, the multiple evaporation sources in the new reactor enables to co-evaporation of multiple solid compounds.

1.5 Scope of Thesis

The goals of this project is to: (1) use oxidative chemical vapor deposition (oCVD) to deposit semiconducting polymers, and (2) integrate these semiconducting polymers into organic photovoltaics (OPVs). The first two research chapters (Chapters 2 and 3) focus on how the oCVD deposition properties affect the resulting polymer properties. Then this knowledge is applied to the integration of these polymers into OPVs.

Chapter 2 investigates the tunable optoelectronic properties of low bandgap (1.05 eV) polyisothianaphthene (PITN) deposited by oCVD. We report a one-step process via oCVD for the simultaneous synthesis and film deposition of unsubstituted PITN, which is normally difficult to obtain in film form. The oCVD PITN film properties were easily tuned by controlling the substrate temperature during deposition. UV-vis absorption, Fourier transform infrared (FTIR) and Raman spectra spectroscopy suggest greater conjugation lengths were achieved with increasing deposition temperature.

Chapter 3 investigates how the pressure of the oCVD process affects the optoelectronic properties of PT films. Shifts in the Raman and UV-vis absorption spectra suggest that films deposited at the lowest pressure deposition conditions have shorter conjugation. Additionally, relative Raman peak intensities suggest that the polymer chains in these films contain more distortions than films deposited at higher pressures. Organic thin film transistors (TFTs) were fabricated using oCVD PT as the active channel layer to analyze the effect of deposition pressure on charge transport and electrical properties.

In Chapter 4 we further characterize oCVD PT and then integrate it into planar heterojunction organic photovoltaics as the electron donor layer. After depositing PT onto ITO, devices are completed with a thermally evaporated C_{60} electron acceptor layer, resulting in power conversion efficiencies up to 0.8%. The absorption edge of the PT at ~620 nm closely matches the edge present in the external quantum efficiency spectra, indicating that the oCVD PT contributes to the photocurrent of the devices.

Chapter 5 discusses the first demonstration of vapor-deposited mixed heterojunction polymer solar cells, which are deposited in an oCVD chamber. This is accomplished by simultaneously evaporating thiophene monomer, iron(III) chloride oxidizing agent, and C_{60} to

result in mixed films of oCVD polythiophene (PT) and C_{60}. Various film compositions are deposited and OPVs made using these films are investigated.

In Chapter 6 we use a three-layer energy cascade device architecture to improve the performance of the OPVs. Addition of a dibenzotetraphenylperiflanthene (DBP) intermediate layer in between PT donor and C_{60} acceptor layers is shown to improve device performance through increased current and voltage. Addition of 10 nm intermediate DBP layer into the PT/C_{60} structure results in device efficiencies up to 2.4% using this energy cascade device architecture.

Chapter 7 concludes this thesis and provides potential future directions.

Lastly, Appendix A provides the detailed engineering drawings for the new oCVD reactor constructed during this thesis.

1.6 References

1.   R. D. McCullough, *Adv. Mater.*, 1998, 10, 93-116.
2.   C. J. Brabec, S. Gowrisanker, J. J. M. Halls, D. Laird, S. J. Jia and S. P. Williams, *Adv. Mater.*, 2010, 22, 3839-3856.
3.   E. Bundgaard and F. C. Krebs, *Sol. Energy Mater. Sol. Cells*, 2007, 91, 954-985.
4.   S. R. Forrest, *Nature*, 2004, 428, 911-918.
5.   R. R. Lunt and V. Bulovic, *Appl. Phys. Lett.*, 2011, 98, -.
6.   C.-C. Chen, L. Dou, R. Zhu, C.-H. Chung, T.-B. Song, Y. B. Zheng, S. Hawks, G. Li, P. S. Weiss and Y. Yang, *ACS Nano*, 2012, 6, 7185-7190.
7.   J. You, L. Dou, K. Yoshimura, T. Kato, K. Ohya, T. Moriarty, K. Emery, C.-C. Chen, J. Gao, G. Li and Y. Yang, *Nat Commun*, 2013, 4, 1446.
8.   12.0% efficienct vacuum-deposited molecular OPV (Heliatek), http://www.heliatek.com/newscenter/latest_news/neuer-weltrekord-fur-organische-solarzellen-heliatek-behauptet-sich-mit-12-zelleffizienz-als-technologiefuhrer/?lang=en, Accessed April 14, 2014.
9.   K. P. Gritsenko and A. M. Krasovsky, *Chem. Rev.*, 2003, 103, 3607-3649.
10.   J. E. Frommer, *Acc. Chem. Res.*, 1986, 19, 2-9.
11.   J. H. Park, J. S. Kim, J. H. Lee, W. H. Lee and K. Cho, *The Journal of Physical Chemistry C*, 2009, 113, 17579-17584.
12.   S. H. Baxamusa, S. G. Im and K. K. Gleason, *Phys. Chem. Chem. Phys.*, 2009, 11, 5227-5240.
13.   M. Manceau, M. Helgesen and F. C. Krebs, *Polym. Degrad. Stab.*, 2010, 95, 2666-2669.
14.   M. H. Petersen, S. A. Gevorgyan and F. C. Krebs, *Macromolecules*, 2008, 41, 8986-8994.

15.   K. M. Vaeth and K. F. Jensen, *Adv. Mater.*, 1997, 9, 490-493.
16.   C.-T. Hsiao and S.-Y. Lu, *The Journal of Physical Chemistry B*, 2010, 114, 7469-7473.
17.   R. Bakker, P. Weijers, C. H. M. van der Werf, J. K. Rath and R. E. I. Schropp, *physica status solidi (a)*, 2010, 207, 647-650.
18.   G. A. Zaharias and S. F. Bent, *Chem. Vap. Deposition*, 2009, 15, 133-141.
19.   G. J. Cruz, J. Morales, M. M. Castillo-Ortega and R. Olayo, *Synth. Met.*, 1997, 88, 213-218.
20.   H. Usui, M. Watanabe, C. Arai, K. Hibi and K. Tanaka, *Japanese Journal of Applied Physics*, 2005, 44, 2810.
21.   G. J. Cruz, J. Morales and R. Olayo, *Thin Solid Films*, 1999, 342, 119-126.
22.   B. Winther-Jensen, J. Chen, K. West and G. Wallace, *Macromolecules*, 2004, 37, 5930-5935.
23.   R. Dams, D. Vangeneagden and D. Vanderzande, *Chem. Vap. Deposition*, 2006, 12, 719-727.
24.   P. M. Bayley, B. Winther-Jensen, D. R. MacFarlane, N. M. Rocher and M. Forsyth, *React. Funct. Polym.*, 2008, 68, 1119-1126.
25.   C. Y. Lee and M. H. C. Jin, in *Organic Photovoltaics Viii*, eds. Z. H. Kafafi and P. A. Lane, 2007, vol. 6656, pp. Y6560-Y6560.
26.   A. H. Bhuiyan and S. V. Bhoraskar, *Thin Solid Films*, 1988, 162, 333-342.
27.   S. G. Im and K. K. Gleason, *Macromolecules*, 2007, 40, 6552-6556.
28.   M. C. Barr, J. A. Rowehl, R. R. Lunt, J. Xu, A. Wang, C. M. Boyce, S. G. Im, V. Bulović and K. K. Gleason, *Adv. Mater.*, 2011, 23, 3500-3505.
29.   M. C. Barr, R. M. Howden, R. R. Lunt, V. Bulović and K. K. Gleason, *Advanced Energy Materials*, 2012, 2, 1404-1409.
30.   D. Bhattacharyya, R. M. Howden, D. C. Borrelli and K. K. Gleason, *J. Polym. Sci., Part B: Polym. Phys.*, 2012, 50, 1329-1351.
31.   T. Yamamoto and M. Abla, *Synth. Met.*, 1999, 100, 237-239.
32.   G. Heywang and F. Jonas, *Adv. Mater.*, 1992, 4, 116-118.
33.   P. Coppo, D. C. Cupertino, S. G. Yeates and M. L. Turner, *Macromolecules*, 2003, 36, 2705-2711.
34.   M. R. Andersson, D. Selse, M. Berggren, H. Jaervinen, T. Hjertberg, O. Inganaes, O. Wennerstroem and J. E. Oesterholm, *Macromolecules*, 1994, 27, 6503-6506.
35.   J. Kim, D. Sohn, Y. Sung and E.-R. Kim, *Synth. Met.*, 2003, 132, 309-313.
36.   N. Chanunpanich, A. Ulman, Y. M. Strzhemechny, S. A. Schwarz, J. Dormicik, A. Janke, H. G. Braun and T. Kratzmüller, *Polym. Int.*, 2003, 52, 172-178.
37.   S.-A. Chen, J.-M. Ni and M.-Y. Hua, *Journal of Polymer Research*, 1997, 4, 261-265.
38.   M. T. Loponen, T. Taka, J. Laakso, K. Väkiparta, K. Suuronen, P. Valkeinen and J. E. Österholm, *Synth. Met.*, 1991, 41, 479-484.
39.   G. Li, R. Zhu and Y. Yang, *Nat Photon*, 2012, 6, 153-161.
40.   B. C. Thompson and J. M. J. Fréchet, *Angew. Chem. Int. Ed.*, 2008, 47, 58-77.
41.   M. T. Dang, L. Hirsch and G. Wantz, *Adv. Mater.*, 2011, 23, 3597-3602.
42.   B. Krische and M. Zagorska, *Synth. Met.*, 1989, 28, C263-C268.
43.   M. Gratzl, D. F. Hsu, A. M. Riley and J. Janata, *The Journal of Physical Chemistry*, 1990, 94, 5973-5981.
44.   T. C. Chung, J. H. Kaufman, A. J. Heeger and F. Wudl, *Phys. Rev. B*, 1984, 30, 702-710.
45.   R. M. Eales and A. R. Hillman, *J. Mater. Sci.*, 1990, 25, 3806-3813.

46.   H. Goktas, F. G. Ince, A. Iscan, I. Yildiz, M. Kurt and I. Kaya, *Synth. Met.*, 2009, 159, 2001-2008.

47.   T. Sorita, H. Fujioka, M. Inoue and H. Nakajima, *Thin Solid Films*, 1989, 177, 295-303.

48.   S. Tepavcevic, Y. Choi and L. Hanley, *J. Am. Chem. Soc.*, 2003, 125, 2396-2397.

49.   J. Tang, L. Kong, J. Zhang, L. Zhan, H. Zhan, Y. H. Zhou and C. Zhan, *React. Funct. Polym.*, 2008, 68, 1408-1413.

50.   X. G. Li, J. Li, Q. K. Meng and M. R. Huang, *J. Phys. Chem. B*, 2009, 113, 9718-9727.

51.   R. Valaski, C. D. Canestraro, L. Micaroni, R. M. Q. Mello and L. S. Roman, *Sol. Energy Mater. Sol. Cells*, 2007, 91, 684-688.

52.   W. L. Yu, B. Xu, Q. F. Dong, Y. H. Zhou, J. H. Zhang, W. J. Tian and B. Yang, *J. Solid State Electrochem.*, 2010, 14, 1051-1056.

53.   C. A. Cutler, A. K. Burrell, G. E. Collis, P. C. Dastoor, D. L. Officer, C. O. Too and G. G. Wallace, *Synth. Met.*, 2001, 123, 225-237.

54.   C. A. Cutler, A. K. Burrell, D. L. Officer, C. O. Too and G. G. Wallace, *Synth. Met.*, 2002, 128, 35-42.

55.   T. Tromholt, S. A. Gevorgyan, M. Jorgensen, F. C. Krebs and K. O. Sylvester-Hvid, *ACS Appl. Mater. Interfaces*, 2009, 1, 2768-2777.

56.   S. A. Gevorgyan and F. C. Krebs, *Chem. Mater.*, 2008, 20, 4386-4390.

57.   O. Hagemann, M. Bjerring, N. C. Nielsen and F. C. Krebs, *Sol. Energy Mater. Sol. Cells*, 2008, 92, 1327-1335.

Chapter 2

Tunable Low Bandgap Polyisothianaphthene via oCVD[*]

2.1 Abstract

Despite polyisothianaphthene's (PITN) desirable properties, complex synthetic routes and lack of solubility have limited its utility, particularly when thin films are required. Here, we report a one-step process for the simultaneous synthesis and film deposition of unsubstituted PITN using oxidative chemical vapor deposition (oCVD). The PITN film properties were easily tuned by controlling the substrate temperature over a range from 70 °C to 130 °C during the oCVD process. The positions of the absorption maxima in the UV-Vis-NIR absorption spectra were considerably red-shifted by over 100 nm with increasing deposition temperature. This resulted in a decrease in the bandgap from 1.14 eV to 1.05 eV. Downshifts in many peak positions were observed in the Fourier transform infrared (FTIR) and Raman spectra with increasing deposition temperature. These observations suggest longer polymer conjugation lengths were achieved with increasing deposition temperature.

2.2 Introduction

Low bandgap polymers are of considerable interest for obtaining high-performing organic electronic and optoelectronic devices.[1, 2] In the neutral state, low bandgap polymers typically absorb in the red or near-infrared region of the electromagnetic spectrum. For organic photovoltaic applications, this enables photon absorption in a part of the solar spectrum often unutilized in polymer solar cells.[3] Enhanced absorption can increase current, thus increasing the device efficiency.[4-8] Low bandgap polymers also electroluminesce in the near infrared. This makes them important materials for organic light emitting diodes for optical communication and sensor applications operating in the near infrared region.[9-11] Upon reversibly doping and dedoping, low bandgap polymers display high optical contrast ratios necessary for electrochromic devices.[12-15]

Furthermore, the high carrier mobilities observed in some low bandgap polymers result in excellent performance in organic field effect transistors.[16-18]

Polyisothianaphthene (PITN) has a very low bandgap of 1 eV.[19] The isothianaphthene monomer consists of a thiophene ring with a benzene ring fused to it at its two β-carbons. Addition of the benzene ring results in competing aromaticity between the benzene and thiophene rings. This stabilizes various resonance structures of PITN, giving it a highly quinoid character. Figure 2-1 shows two of the resonance structures of PITN. While most conjugated polymers adopt the aromatic form in the ground state, the quinoid form of PITN is more stable by ~2 kcal/mol per repeat unit.[20-25] As a result, PITN has a bandgap that is half the value of its parent polythiophene.[19, 26, 27] PITN's low bandgap enables it to exhibit a high optical contrast ratio upon reversible doping and dedoping. It is dark blue in the neutral state but becomes almost transparent at visible wavelengths upon doping.[28] This makes the polymer a good candidate for electrochromic applications.
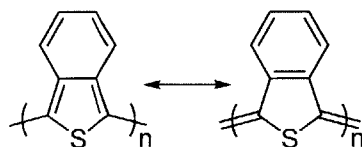
Figure 2-1. Aromatic (left) and quinoid (right) resonance structures of PITN.

The complexity of synthesis routes and/or the poor solubility of PITN have limited its utility. Figure 2-2 summarizes the three main methods used to prepare PITN (5). The first, and most common, synthesis route is by electrochemical polymerization to obtain a film deposited on an electrode surface (route I in Figure 2-2).[19, 27-30] However, this approach usually requires a difficult synthesis procedure that employs isothianaphthene (3) as the monomer precursor, which is unstable. Isothianaphthene (ITN) must be synthesized immediately prior to use and special conditions and careful temperature control are needed to obtain PITN.[31, 32] Additionally, it can be

difficult to reproducibly deposit smooth homogenous films using electropolymerization.[33] The second PITN synthesis approach is dehydrogenation of poly(1,3-dihydroisothianaphthene) (PDHITN) (route II in Figure 2-2).[19, 34-37] ITN (3) can be polymerized to PDHITN (4) chemically (for example, with CH_3SO_3H) or electrochemically. Since PDHITN (4) is soluble, it can be cast into a film before converting to PITN (5). SO_2Cl_2 is typically used for this dehydrogenation. However, this synthesis approach adds an extra step to the PITN synthesis process and still requires the use of ITN. The third approach is by chemical reaction of a monomer to form PITN, which is typically performed in solution. Various compounds have been used as the monomer precursor for the polymerization process. Concentrated H_2SO_4 will react directly with both isothianaphthene (3) and 1,3-dihydrobenzo[c] thiophene 2-oxide (2) to form PITN (5).[19] Phthalic anhydride has been shown to react with thionating reagents, such as phosphorus pentasulphide (P_4S_{10}), to yield PITN.[38, 39] More promisingly, the molecule 1,3-dihydroisothianaphthene (DHITN) (1), which unlike 3 is stable, will react with $FeCl_3$, N-chlorosuccinimide, and other species to produce PITN (route III in Figure 2-2).[40-42] This provides a much shorter and more direct synthesis route to PITN. However, the chemical reaction of any of these monomers in solution will only result in PITN powder instead of a film. Thus, this method has had limited practicality since the insolubility of PITN makes it difficult to process after polymerized. Table 2-1 summarizes the synthesis techniques available.
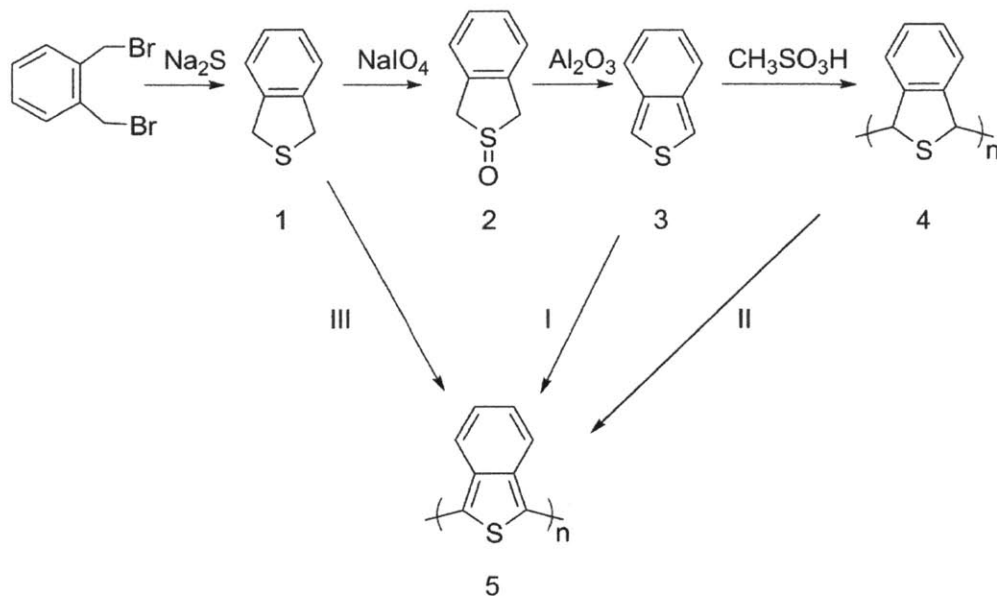
Figure 2-2. Common reaction schemes for obtaining polyisothianaphthene (PITN) (5). Polymerization from isothianaphthene (3) is possible but difficult because it is unstable (route I). Direct polymerization from 1,3-dihydroisothianaphthene (DHITN) (1) (route III) provides a fast synthesis route for depositing PITN films by oCVD.

Table 2-1. Summary of the synthesis routes of PITN. oCVD uniquely offers a one-step method for obtaining films of PITN.

Method	Synthesis Route	Number of Steps	Film Formation
Electropolymerization of ITN	I	3	Yes, on conductive substrates only
Dehydrogenation of PDHITN	II	5[a]	Yes, on dielectric and conductive substrates
Chemical polymerization of DHITN in solution	III	1	No, unprocessable powder formed
Oxidative CVD of DHITN	III	1	Yes, on dielectric and conductive substrates

[a]The casting of PDHITN into a film is included as a step in this process

Introduction of long alkyl side chains or other substituents makes the polymer soluble and processable, but it also often increases the bandgap.[43-48] Additionally, these polymerization methods produce ITN homopolymers and copolymers that have low molecular weights and poor film-forming properties.[45, 46, 49-52]

37

Oxidative chemical vapor deposition (oCVD) offers a facile route for depositing films of conjugated polymers, regardless of polymer solubility properties. Using vapor phase monomer and oxidant precursors, conjugated polymers are simultaneously synthesized and deposited on a substrate at low temperature (~25-150 °C) and moderate vacuum (~0.1 Torr) during oCVD.[53] oCVD offers accurate thickness control and uniformity over large areas that is independent of the substrate material.[54] Additionally, polymers can be conformally deposited on nonplanar substrates using oCVD, allowing compatibility with substrates such as textiles and paper.[55, 56] Previously, oCVD has been used to deposit thin films of doped conducting polymers, such as poly(3,4-ethylenedioxythiophene) (PEDOT), and semiconducting polymers such as unsubstituted polythiophene.[57, 58] These oCVD polymers were used for various applications, including electrochromic devices, transparent electrodes in small molecule organic solar cells, and part of the photoactive layer in polymer solar cells.[55, 57, 59, 60]

Here we report the preparation and characterization of unsubstituted PITN films by oCVD following the short synthesis route III. Films of PITN are prepared in a one-step process using DHITN as the monomer precursor and iron(III) chloride as the oxidizing agent. Conductive, as-deposited films and dedoped, semiconductive oCVD PITN films are studied as both forms are of interest. More emphasis is placed on the neutral, semiconductive form of oCVD PITN as its very low bandgap may be of particular interest for optoelectronic device applications, such as organic solar cells. Characterization of the PITN films as a function of the deposition temperature shows an ability to control the resulting polymer properties. In particular, increased deposition temperatures result in higher conjugation and decreased bandgap.

2.3 Experimental

2.3.1 Polyisothianaphthene oCVD Depositions

Polymer films were deposited using oCVD, which is described in more detail elsewhere.[58,] [61] The oCVD process was performed in a custom-built vacuum chamber that has monomer inlet ports and an exhaust to a pump. At the bottom of the reactor chamber was a resistively-heated crucible that holds the oxidizing agent, iron (III) chloride ($FeCl_3$, 97%, Sigma-Aldrich), which was used as purchased. 0.3 to 0.5 g of $FeCl_3$ was used and it was sublimed at 340 °C during the oCVD process. Above the oxidant crucible was a downward-facing stage where the substrates were placed. Glass slides and silicon wafers were used as substrates. DHITN (1) was used as the monomer precursor for the depositions. The synthesis of DHITN (>96%) was carried out by SynChem, Inc. (Elk Grove Village, IL) according to the reaction shown in Figure 2-2 following procedures from the literature.[62] The DHITN monomer jar was maintained at a temperature of 130 °C. Vapor phase DHITN was introduced into the reactor chamber from a side port on the reactor. A series of depositions were performed in which the stage temperature was held constant at 70 °C, 90 °C, 110 °C, or 130 °C while the reactor body temperature was held at least 20 °C hotter than the stage. Depositions using higher stage temperatures were also performed, and they resulted in polymer films with properties consistent with the trends in the data discussed. However, given the reactor setup used for these experiments, it was difficult to reproducibly obtain films with stage temperatures above 130 °C because of difficulty maintaining uniform reactor body temperatures above about 150 °C. The chamber pressure was held constant at 130 mTorr during the deposition using a butterfly valve. A deposition time of 20 minutes was used for all films. Upon completion, the samples were then removed from the vacuum chamber, which exposed them to air. The films were then rinsed to remove reacted oxidant. The rinsing step consisted of sample immersion into methanol (≥99.9%, Sigma-Aldrich) for 10 minutes, followed by dilute HCl for 5 minutes (4.4 mL

HCl dissolved in 250 mL methanol), and then ammonia in methanol (2.0M, Sigma-Aldrich) for 5 minutes.

2.3.2 Polymer Characterization

Film thicknesses were measured using a Veeco Dektak 150 surface profilometer and the sheet resistances were measured with a Jandel four-point probe. Conductivity values were calculated using the measured sheet resistance and the thickness measured with the profilometer. X-ray photoelectron spectroscopy (XPS) measurements were performed using a Surface Science Instruments (SSI) model SSX-100 with operating pressure $<2 \times 10^{-9}$ Torr utilizing monochromatic AlKα X-rays at 1486.6 eV. Photoelectrons were collected at an angle of 55-degrees from the surface normal. UV-Vis-NIR spectra of the PITN films on glass substrates were measured with a Varian Cary 5000 UV-Vis-NIR spectrophotometer. Transmission and reflection spectra were measured. The reflection spectra were obtained using an absolute specular reflectance accessory and an Al standard reference mirror (ThorLabs). Fourier transform infrared (FTIR) measurements of the PITN films on silicon wafers were performed on a Nexus 870, Thermo Electron Corp. spectrometer. The spectra were normalized by the film thicknesses. Raman spectra were taken with a Horiba Jobin-Yvon LabRam Raman Confocal Microscope with a 532 nm laser. The spectra were normalized such that the strongest peaks in each film's spectra have the same height. Cyclic voltammetry measurements were conducted using a 660D potentiostat (CH Instruments) with a standard three-electrode configuration under a nitrogen atmosphere. A platinum mesh attached to a platinum wire was used as the counter electrode, Ag/AgNO$_3$ (0.01 M in acetonitrile) was used as the reference electrode, and PITN-coated ITO/glass was the working electrode. The measurements were performed in acetonitrile with tetrabutylammonium hexafluorophosphate (0.1 M) as the supporting electrolyte at a scan rate of 50 mV s^{-1}. The Fc/Fc$^+$ redox couple was used to calibrate the Ag/Ag$^+$ reference electrode. The XRD measurements were taken with Scintag Theta-

Theta diffractometer (model PAD-X), using CuKα radiation. The settings for the instrument were 40 kV and 40 mA. The data was collected from 2 to 40 degrees, 2θ, at a rate of 2 degrees/minute and a step size of 0.03 degrees.

2.4 Results and discussion

2.4.1 PITN Synthesis

PITN films were simultaneously synthesized and deposited using oCVD. DHITN monomer was reacted with FeCl₃ via route III in Figure 2-2 for this process. Monomer and oxidizing agent (FeCl₃) precursor vapors were delivered into a vacuum chamber to a temperature-controlled stage where they reacted to yield PITN films. The PITN film properties were tuned by controlling the stage temperature between 70 °C and 130 °C during deposition. The as-deposited films were doped and conductive. In order to analyze the semiconducting form of the PITN films, they were rinsed with methanol, hydrochloric acid, and ammonia. The acid rinse step fully removed any residual iron left in the films.[63] The ammonia rinse was necessary to dedope the polymer by reducing it to the neutral state.[27]

2.4.2 Conductivity

The as-deposited oCVD polymer films were doped and conductive. Conductivity measurements in air showed several orders of magnitude increases in the film conductivities with increasing substrate temperature during deposition. Maximum conductivities of 1×10^{-3}, 1×10^{-1} and 1 S/cm were measured for samples deposited at 90 °C, 110 °C, and 130 °C, respectively. It was not possible to obtain consistent measurements for the samples deposited at 70 °C, likely because of very low conductivity. The large increases in conductivity might suggest that higher deposition temperatures result in increased conjugation length, as has been observed for oCVD PEDOT.[58]

The increased conjugation was attributed to faster polymerization kinetics that resulted in higher molecular weight and a decrease in defects from side reactions. The conductivity values obtained for the oCVD PITN film deposited at 130 °C compare favorably with the values of most electropolymerized PITN samples in the literature.[19, 30, 39] Additionally, after dedoping the films with acid and ammonia and redoping the films with concentrated HBr, conductivities up to about 4 S/cm were obtained. The highest reported value in the literature of 50 S/cm was obtained by in situ doping of electropolymerized PITN.[27]

Dedoping of the oCVD PITN films with ammonia resulted in average conductivity decreases by four orders of magnitude. Samples were dedoped with ammonia under a nitrogen atmosphere and the conductivities were measured without air exposure. PITN films deposited at 110 °C and 130 °C showed conductivities of 2×10^{-5} and 1×10^{-4} S/cm, respectively. The conductivities of the samples deposited at 70 °C and 90 °C were below the detection limit of the equipment used. These values are slightly lower than those typically observed. Conductivity values reported in the literature of dedoped PITN films range from 4×10^{-4} to 3×10^{-2} S/cm.[27, 39, 64] Exposure of the samples to air increased the conductivities of all the dedoped samples. Ten minutes of air exposure resulted in a 4x increase in film conductivities. After about two hours in air, conductivities increased to about 3×10^{-5}, 3×10^{-4}, and 9×10^{-4} S/cm for samples deposited at 90 °C, 110 °C, and 130 °C, respectively. It has been noted in the literature that exposure of PITN films to air results in doping of the polymer chains by oxygen.[65] Oxygen may react to form a carbonyl group or form a charge-transfer complex involving an O_2^- dopant.[41] Thus, as with many other semiconducting polymers, air exposure after dedoping should be avoided to employ the semiconducting form of PITN in a device.

2.4.3 XPS

X-ray photoelectron spectroscopy (XPS) survey scans of the as-deposited and dedoped oCVD PITN films show that the rinse procedure successfully removes the iron and chlorine from the PITN films (Figure 2-3). According to the XPS scans, the dedoped films only contain C, S, and O. Also, the as-deposited and dedoped films both appear to have high oxygen contents, likely as a result of air exposure. Since iron(III) chloride is hygroscopic, the high oxygen content of the as-deposited PITN may be due to absorbed water vapor and oxygen. The high oxygen content of the dedoped films may be from a combination of absorbed oxygen and carbonyl groups formed.
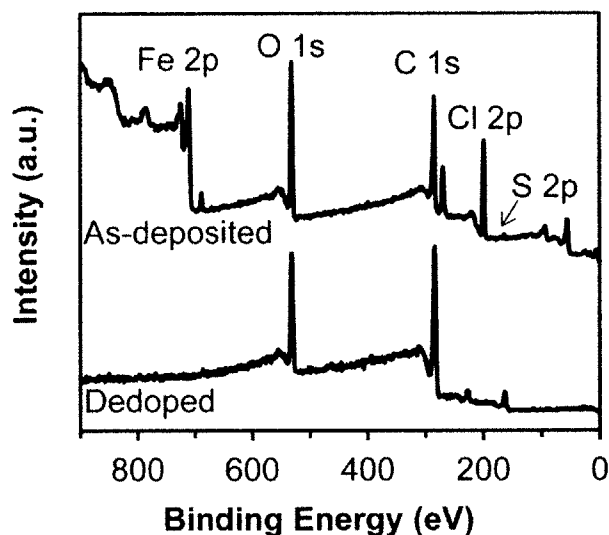
Figure 2-3. XPS spectra of as-deposited and dedoped oCVD PITN films. Iron and chlorine are successfully removed from the films during the dedoping process.

2.4.4 UV-Vis-NIR Spectroscopy

The UV-Vis-NIR absorption spectra of the as-deposited PITN films as a function of the film deposition temperature are shown in Figure 2-4a. Peaks around 540 nm and 720 nm are apparent in the sample deposited at 70 °C. However, they diminish as the deposition temperature increases. These peaks are essentially absent in the film deposited at 130 °C. Spectroscopic studies

of electrochemically-prepared PITN suggested that these peaks are due to entrapped monomers or oligomers in freshly prepared films.[66] Thus, the reduction of these two peaks as the deposition temperature increases suggests better conversion of reactants to polymer and fewer short chains at higher temperatures. The color of the as-deposited film was also influenced by the substrate temperature during the deposition process. At 70 °C, the film was a bright red color (inset in Figure 2-4a). As the temperature increased, the film became more yellowish in color. The changes in color are attributed to reductions in the reflection spectra in regions of visible light for higher deposition temperatures (data not shown). Additionally, the minima in the absorption spectra shifts slightly as the temperature increases, going from 611 nm to 585 nm. The low absorption of the p-doped PITN within the visible part of the spectrum supports its potential use for electrochromic applications.
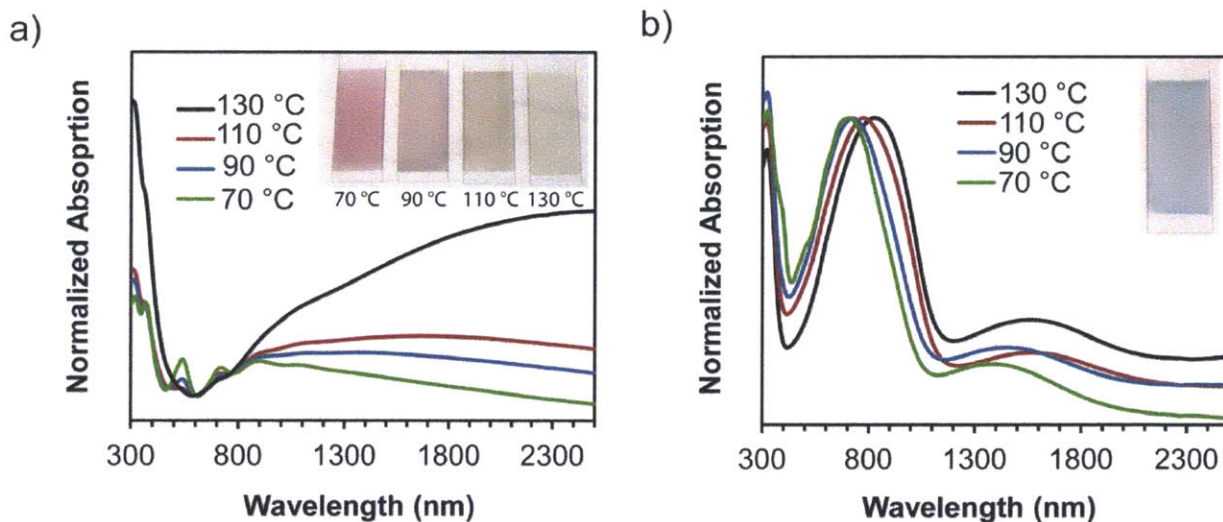
Figure 2-4. a) UV-Vis-NIR absorption spectra of the as-deposited oCVD PITN films show increased transparency in the visible part of the spectrum as the deposition temperature increases. Inset: as-deposited doped PITN films on 25mm x 75mm glass slides. **b)** Increases in stage temperature during polymer deposition results in a significant red shift in the UV-Vis-NIR absorption spectra of the dedoped films. Inset: dedoped PITN film deposited at 130 °C.

44

The post-deposition dedoping of the films caused them to undergo an abrupt color change to blue (inset in Figure 2-4b). There was no discernible difference in the appearance of the dedoped films deposited at different temperatures. As the stage temperature increases from 70 °C to 130 °C, the absorption maxima of the films increase as: 706, 719, 769, and 827 nm. Thus, considerable red-shifting occurs upon increasing the deposition temperature. The position of the absorption maximum for the film deposited at 130 °C is slightly red-shifted compared to those reported in the literature for PITN prepared by various methods.[36, 64, 66] Additionally, the optical band gap (E_g), calculated as the intersection of the line tangent to the absorption edge with the x-axis, decreases as the temperature increases. E_g decreases from 1.14 eV to 1.05 eV as the temperature increases from 70 °C to 130 °C. This suggests that higher deposition temperatures result in increased conjugation in the resulting PITN films.

The extra small, broad peaks around 1500-1600 nm suggest that the films are not fully dedoped as polarons or bipolarons may be present.[27, 28, 67] This is likely due to exposing the dedoped samples to air, which was necessary to perform the measurement. The height of these peaks also appeared to slightly increase with increased air exposure time. The presence of small peaks at longer wavelengths has also been noted in films of substituted polyisothianaphthenes and attributed to doping by oxygen in the air.[68]

2.4.5 Fourier Transform Infrared (FTIR) Spectroscopy

The FTIR spectra of the dedoped films deposited at various temperatures are shown in Figure 2-5a. All of the major infrared bands characteristic of PITN were observed in all the film spectra and the band positions were consistent with those published in the literature.[19, 20, 38, 39, 41, 69] Peak intensity increases for all of the peaks as the deposition temperature increases. For the film

deposited at 130 °C, peaks appear at 737, 847, 874, 976, 1055, 1142, 1188, 1221, 1265, 1381, 1452, 1589, and 1680 cm^{-1}.

a)

b)
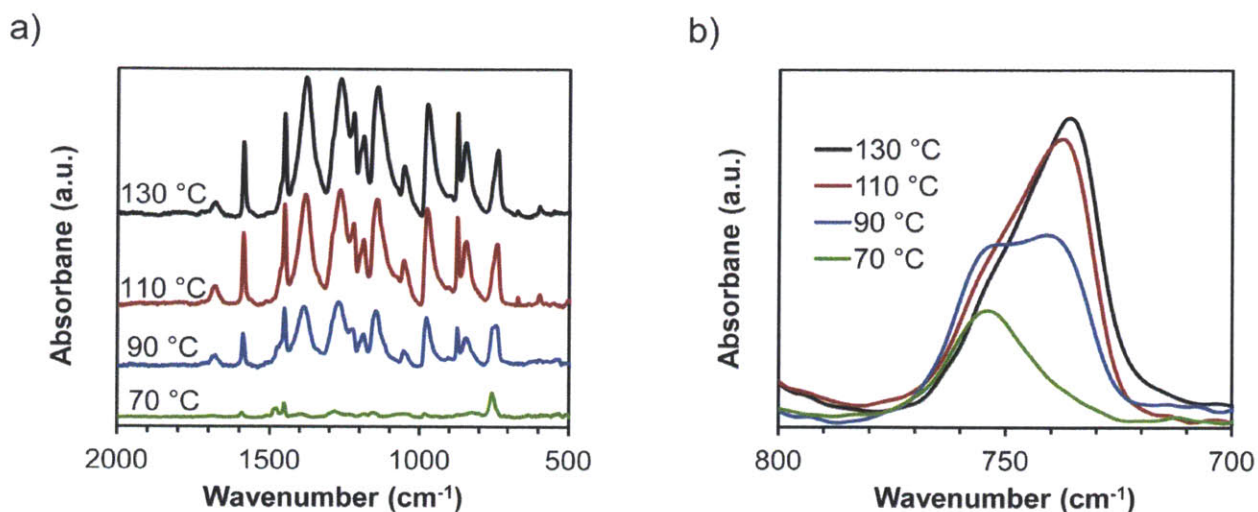
Figure 2-5. a) FTIR spectra of dedoped PITN deposited at the various temperatures. **b)** Absorption peaks corresponding to the C-H vibration of the four adjacent hydrogens. As the deposition temperature of the oCVD PITN films increases, a peak emerges at lower wavenumbers. This suggests a change in the bonding environment, possibly due to a transition to a more quinoid form.

Although the films deposited at lower temperatures also exhibit all of these peaks, many of their positions are shifted. As the deposition temperature increases from 70 °C to 130°C, there is a monotonic decrease in the wavenumber of the associated peak. Hernandez et al. noted significant downshifts in position for many peaks, including those associated with interring C=C bonds and intra-ring aromatic C=C stretching, in the IR spectra of oligothiophenes with increasing conjugation length.[70] The three peaks around 976, 1142, and 1221 cm^{-1} have been assigned to interring C-C and C=C deformations and other bending modes in PITN.[69] Table 2-2 lists the peak positions for the films deposited at various temperatures. Peak assignments for both the quinoid and aromatic forms of PITN are listed as the small energy difference between them may allow both forms to contribute to the structure of the polymer.[25] With increasing temperature from 70 °C to 130 °C, these peaks all demonstrate downshifts in position. Additionally, the peaks around

1265 and 1381 cm^{-1}, which have been assigned to C-C and C=C in the benzene and thiophene rings,[69] also exhibit downshifts with increasing temperature. Thus, the downshift in peak positions is consistent with increased conjugation of the resulting film with higher deposition temperatures.

Table 2-2. FTIR band positions of oCVD PITN films demonstrate downshifts with increasing deposition temperature.

Peak Assignments (from Ref [69])		Wavenumber (cm^{-1})			
Quinoid	Aromatic	70 °C	90 °C	110 °C	130 °C
C=C interring deformation + benzene breathing mode	C-C interring deformation + benzene breathing mode	984	980	976	974
C=C interring deformation + benzene breathing mode	C-C stretch intraring and interring + C-H bending	1153	1147	1144	1142
C-C stretch in thiophene ring + C-H bending	C-C interring + thiophene ring deformation + C-H bending	1232	1223	1221	1221
C-C stretch in thiophene ring + C=C stretch in benzene ring	C-C stretch in benzene ring + C-H bending	1283	1273	1267	1265
		1394	1389	1384	1381

All films exhibit a peak near 1680 cm^{-1}, which is assigned to C=O stretching. This peak has also been observed in spectra of PITN films prepared by direct polymerization of DHITN using other methods.[20, 41, 69] It has been suggested that the presence of carbonyl groups show that oxygen may be acting as a dopant for the polymer.[41]

The absorption band around 740 cm^{-1} corresponds to the C-H out-of-plane wag vibration of the four adjacent hydrogens in the benzene ring.[71] This peak displays an interesting trend as the film deposition temperature increases (Figure 2-5b). Rather than showing a simple downshift in wavenumber, as with the other peaks, there appears to be a second peak that emerges in the spectra at a lower position as temperature is increased. This suggests a change in the bonding environment

of the four adjacent hydrogens in the benzene ring. A possible explanation may lie in differences in geometry between the oligomeric and polymeric versions of the chains. It has been noted that isothianaphthene oligomers have an aromatic character if the terminal α carbon has a single bond, such as to hydrogen.[72] Given the highly oxidative environment of the oCVD process, it may be possible for the terminal monomer to deprotonate, resulting in an aromatic configuration for the oligomer. In contrast, the extended polymer chain is known to adopt a more quinoid character.[20] The higher temperature may increase the polymerization rate enough to minimize the amount of over-oxidation of the chains and preserve the sp^3-hybridization of the terminal carbon atoms. Additionally, this explanation is consistent with the positions of the relevant peaks in ITN and DHITN monomers that appear at 770 cm^{-1} and 750 cm^{-1}, respectively.[73, 74] The four adjacent C-H in ITN (3) resemble those in aromatic PITN, while those in DHITN (1) resemble those in quinoid PITN. The downshifts would be expected upon increased chain length.[19, 72] The peak position in oCVD PITN is 754 cm^{-1} for the film deposited at 70 °C and 737 cm^{-1} in the film deposited at 130 °C. Thus, this appears to suggest that there may be more shorter-chain and aromatic oligomers present at lower temperatures, which is consistent with the UV-Vis-NIR absorption data. At higher temperatures, a larger fraction of them are converted to longer quinoidal chains.

2.4.6 Raman Spectroscopy

The Raman spectra for the PITN films are shown in Figure 2-6a. All oCVD PITN films exhibit Raman bands near: 447(s), 988 (m), 1168(s), 1212(m), 1308(s), 1452(s), 1498(vs), and 1591(m) cm^{-1}, along with many other minor features. These band positions match those reported in the literature for PITN prepared by chemical and electropolymerization techniques.[22, 39, 69, 75-77] The peaks at 988, 1168 and 1308 cm^{-1} are attributed to the benzene ring, while the peaks at 447 and 1212 cm^{-1} are attributed to the presence of the thiophene ring.[77]

a)

b)
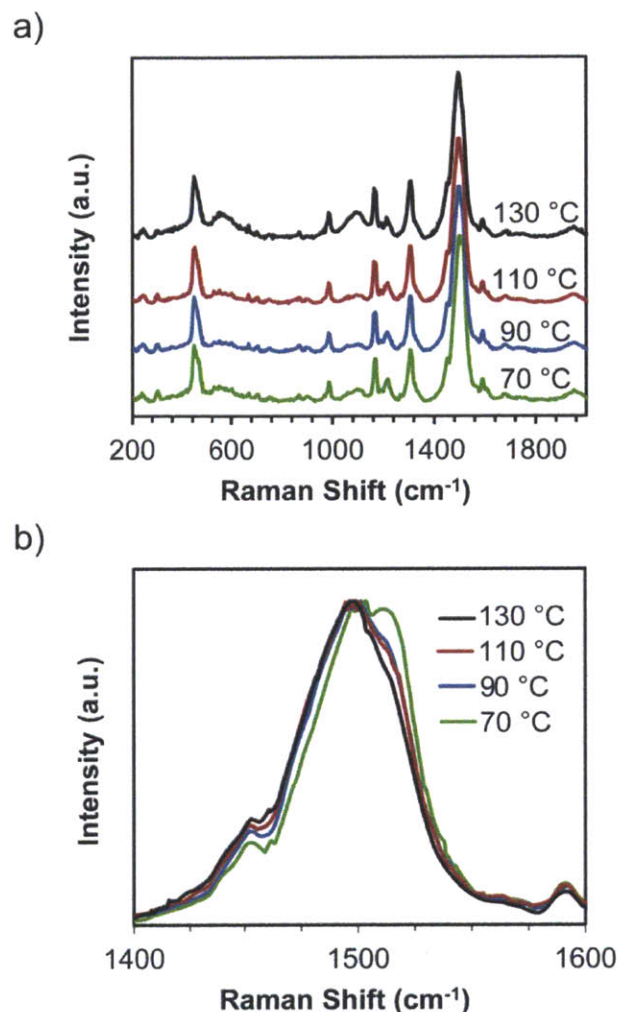
Figure 2-6. a) Raman spectra of dedoped oCVD PITN films as a function of deposition temperature. **b)** Increased temperature results in a downshift in the peak position, demonstrating better conjugation.

The bands at 1212 and 1497 cm^{-1}, which are both correlated with interring C–C or C=C stretching, exhibit shifts in position based on the deposition temperature. The peak around 1212 cm^{-1} decreases monotonically from 1218 to 1212 cm^{-1} as the temperature increases from 70 °C to 130 °C. Additionally, the band around 1498 cm^{-1} decreases monotonically from 1504 to 1498 cm^{-1} with increasing temperature (Figure 2-6b). Decreases in Raman peak positions related to conjugated C-C bonds have been correlated with increased conjugation in many oligomers and polymers.[70, 72, 78, 79] The magnitude of the shift is consistent with that seen in thiophenes.[70]

Furthermore, the peak near 1500 cm^{-1} in particular is thought to provide information on the lengths of the conjugated segments in PITN, with lower wavenumbers associated with greater conjugation.[76] Thus, the Raman spectra of the oCVD PITN films suggest increased conjugation with higher temperatures.

2.4.7 Electrochemical Properties

Cyclic voltammetry (CV) was used to study the electrochemical properties of oCVD PITN. The working electrodes consisted of ITO-coated glass with dedoped oCVD PITN films deposited on them. The ferrocene/ferrocenium (Fc/Fc$^+$) couple was used as an external standard, and its half-wave potential ($E_{1/2}$) was measured under the same testing conditions to be 0.088 V relative to the Ag/Ag$^+$ electrode. Upon cycling the voltage during the scans, there were distinct color changes associated with the p-doping process. In the neutral state the films were deep blue. As the films were p-doped they turned almost transparent. This observation is consistent with what has been observed for electrochemically polymerized PITN.[27, 80]

The cyclic voltammograms of the PITN films are shown in Figure 2-7. The films exhibited a decreasing trend in the onset and maxima of the oxidation peaks with increasing temperature. The CV curves of the oCVD PITN films were consistent with electrochemically-prepared PITN in the literature.[29, 33, 66, 80] With increasing temperature from 70 °C to 130 °C, the onset of the oxidation were estimated as: -0.41, -0.48, -0.49, -0.54 V vs Fc/Fc$^+$, respectively. The highest occupied molecular orbital (HOMO) energy level of the oCVD PITN films were calculated according to the following equation:

$$E_{HOMO} = -\left(E_{\left[onset,ox \ vs \ Fc/Fc^+ \right]} + 4.76 \right)(eV)$$

50

This equation uses an absolute energy value for the redox potential of Fc/Fc$^+$ of -4.76 eV relative to vacuum.[81] The low oxidation potential of the PITN films result in relatively high HOMO levels (Table 2-3). These high values likely make the PITN films very susceptible to oxidation by ambient oxygen. The lowest unoccupied molecular orbital (LUMO) level was calculated by adding the optical bandgap of the respective films to the calculated HOMO level. As summarized in Table 2-3, the HOMO level rises slightly as the deposition temperature increases but the LUMO level maintains a value of about -3.2 eV for all films.
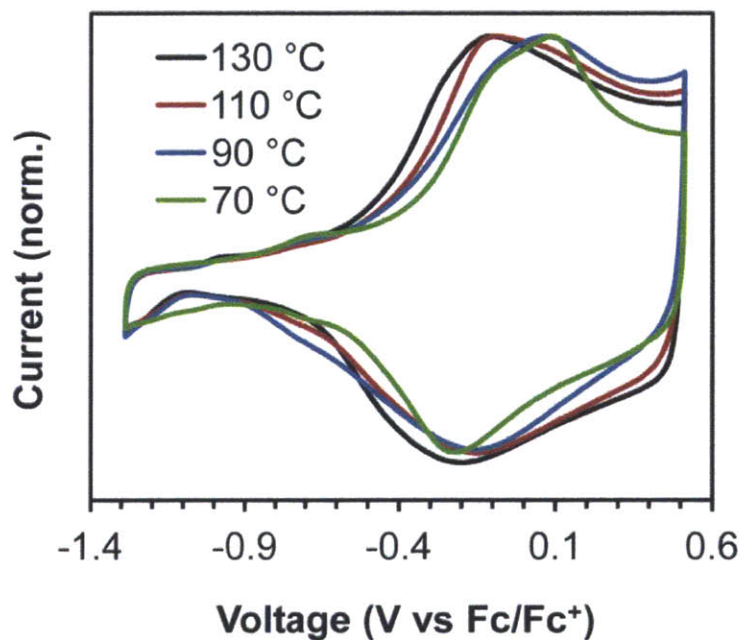
Figure 2-7. Cyclic voltammogram of oCVD PITN films at 50 mV/s.

Table 2-3. Summary of selected properties of oCVD PITN films.

Dep. Temp. (°C)	$\sigma_{as\text{-}deposited}$ (S/cm)	λ_{max} (nm)	E_g (eV)	HOMO (eV)	LUMO (eV)
70	-	706	1.14	-4.35	-3.21
90	1×10^{-3}	719	1.09	-4.28	-3.19
110	1×10^{-1}	769	1.06	-4.27	-3.21
130	1	827	1.05	-4.22	-3.19

2.4.8 XRD

X-ray diffraction measurements of the oCVD PITN films show that the films are amorphous, as shown in Figure 2-8. A broad amorphous halo is present in all the films, with a peak at about $2\theta=23°$. Thus, it does not appear that differences in the film crystallinity cause the conductivity changes observed in the films with increasing temperature.
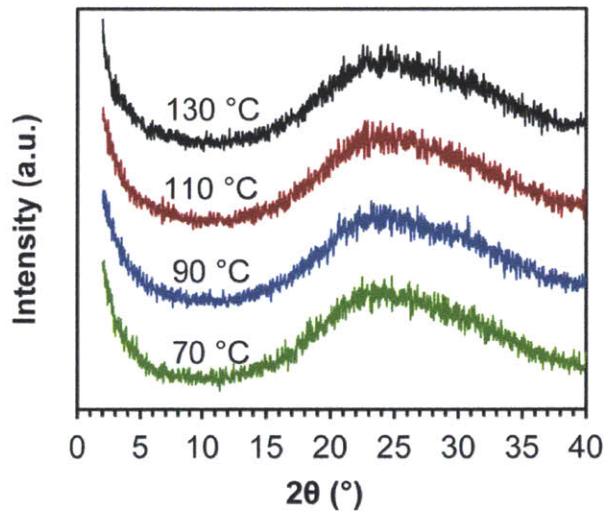
Figure 2-8. XRD scans of oCVD PITN films at various deposition temperatures.

2.5 Conclusions

The oCVD method simultaneously provides for the direct chemical synthesis of PITN and thin film formation. This method is compatible with a variety of substrates, both dielectric and conducting. Monotonic variation in the optical and electrical properties of PITN occurred as the substrate temperature was raised from 70 °C to 130 °C (Table 2-3). The conductivity of the doped, as-deposited films changed by over three orders of magnitude, with a maximum of about 1 S/cm. The position of the absorption maxima in the UV-Vis-NIR spectra of dedoped films was considerably red-shifted by over 100 nm with increasing deposition temperature. This resulted in

a decrease in the bandgap from 1.14 eV to 1.05 eV. Additionally, trends in the FTIR and Raman spectra confirm greater conjugation with increasing temperature. This facile synthesis and deposition route for obtaining PITN films with tunable properties by oCVD will facilitate its application to organic optoelectronic devices.

2.6 Acknowledgements

2.7 References

1. J. Roncali, *Chem. Rev.*, 1997, 97, 173-206.
2. A. Facchetti, *Chem. Mater.*, 2010, 23, 733-758.
3. C. Winder and N. S. Sariciftci, *J. Mater. Chem.*, 2004, 14, 1077-1086.
4. E. Bundgaard and F. C. Krebs, *Sol. Energy Mater. Sol. Cells*, 2007, 91, 954-985.
5. P.-L. T. Boudreault, A. Najari and M. Leclerc, *Chem. Mater.*, 2010, 23, 456-469.
6. J. Hou, M.-H. Park, S. Zhang, Y. Yao, L.-M. Chen, J.-H. Li and Y. Yang, *Macromolecules*, 2008, 41, 6012-6018.
7. Y. Liang, D. Feng, Y. Wu, S.-T. Tsai, G. Li, C. Ray and L. Yu, *J. Am. Chem. Soc.*, 2009, 131, 7792-7799.
8. D. Mühlbacher, M. Scharber, M. Morana, Z. Zhu, D. Waller, R. Gaudiana and C. Brabec, *Adv. Mater.*, 2006, 18, 2884-2889.
9. C. J. Brabec, C. Winder, N. S. Sariciftci, J. C. Hummelen, A. Dhanabalan, P. A. van Hal and R. A. J. Janssen, *Adv. Funct. Mater.*, 2002, 12, 709-712.
10. R. Yang, R. Tian, J. Yan, Y. Zhang, J. Yang, Q. Hou, W. Yang, C. Zhang and Y. Cao, *Macromolecules*, 2005, 38, 244-253.
11. M. Chen, E. Perzon, M. R. Andersson, S. Marcinkevicius, S. K. M. Jonsson, M. Fahlman and M. Berggren, *Appl. Phys. Lett.*, 2004, 84, 3570-3572.
12. H. Meng, D. Tucker, S. Chaffins, Y. Chen, R. Helgeson, B. Dunn and F. Wudl, *Adv. Mater.*, 2003, 15, 146-149.
13. G. E. Gunbas, A. Durmus and L. Toppare, *Adv. Mater.*, 2008, 20, 691-695.
14. B. C. Thompson, Y.-G. Kim, T. D. McCarley and J. R. Reynolds, *J. Am. Chem. Soc.*, 2006, 128, 12714-12725.

15. P. M. Beaujuge, S. Ellinger and J. R. Reynolds, *Nat Mater*, 2008, 7, 795-799.

16. M. M. Durban, P. D. Kazarinoff and C. K. Luscombe, *Macromolecules*, 2010, 43, 6348-6352.

17. H. Yan, Z. Chen, Y. Zheng, C. Newman, J. R. Quinn, F. Dotz, M. Kastler and A. Facchetti, *Nature*, 2009, 457, 679-686.

18. Y. Li, P. Sonar, S. P. Singh, M. S. Soh, M. van Meurs and J. Tan, *J. Am. Chem. Soc.*, 2011, 133, 2198-2204.

19. F. Wudl, M. Kobayashi and A. J. Heeger, *The Journal of Organic Chemistry*, 1984, 49, 3382-3384.

20. I. Hoogmartens, P. Adriaensens, D. Vanderzande, J. Gelan, C. Quattrocchi, R. Lazzaroni and J. L. Bredas, *Macromolecules*, 1992, 25, 7347-7356.

21. R. Kiebooms, I. Hoogmartens, P. Adriaensens, D. Vanderzande and J. Gelan, *Macromolecules*, 1995, 28, 4961-4969.

22. L. Cuff, M. Kertesz, J. Geisselbrecht, J. Kürti and H. Kuzmany, *Synth. Met.*, 1993, 55, 564-569.

23. J. Kurti and P. R. Surjan, *The Journal of Chemical Physics*, 1990, 92, 3247-3248.

24. Y.-S. Lee and M. Kertesz, *The Journal of Chemical Physics*, 1988, 88, 2609-2617.

25. K. Nayak and D. S. Marynick, *Macromolecules*, 1990, 23, 2237-2245.

26. J. L. Bredas, A. J. Heeger and F. Wudl, *The Journal of Chemical Physics*, 1986, 85, 4673-4678.

27. M. Kobayashi, N. Colaneri, M. Boysel, F. Wudl and A. J. Heeger, *The Journal of Chemical Physics*, 1985, 82, 5717-5723.

28. H. Yashima, M. Kobayashi, K. B. Lee, D. Chung, A. J. Heeger and F. Wudl, *J. Electrochem. Soc.*, 1987, 134, 46-52.

29. M. Lapkowski, R. Kiebooms, J. Gelan, D. Vanderzande, A. Pron, T. P. Nguyen, G. Louarn and S. Lefrant, *J. Mater. Chem.*, 1997, 7, 873-876.

30. P. Chandrasekhar, A. M. Masulaitis and R. W. Gumbs, *Synth. Met.*, 1990, 36, 303-326.

31. P. A. Christensen, J. C. H. Kerr, S. J. Higgins and A. Hamnett, *Faraday Discussions of the Chemical Society*, 1989, 88, 261-275.

32. M. P. Cava, N. M. Pollack, O. A. Mamer and M. J. Mitchell, *The Journal of Organic Chemistry*, 1971, 36, 3932-3937.

33. S. J. Higgins, C. Jones, G. King, K. H. D. Slack and S. Pétidy, *Synth. Met.*, 1996, 78, 155-159.

34. S.-A. Chen and C.-C. Lee, *Polymer*, 1996, 37, 519-522.

35. T. L. Rose and M. C. Liberto, *Synth. Met.*, 1989, 31, 395-398.

36. S.-A. Chen and C.-C. Lee, *Synth. Met.*, 1995, 75, 187-189.

37. S. Ito, T. Suzuki, T. Kawai and T. Iyoda, *Synth. Met.*, 2000, 114, 235-242.

38. H. Paulussen, H. Haitjema, R. van Asselt, P. Mylle, P. Adriaensens, J. Gelan and D. Vanderzande, *Polymer*, 2000, 41, 3121-3127.

39. R. van Asselt, I. Hoogmartens, D. Vanderzande, J. Gelan, P. E. Froehling, M. Aussems, O. Aagaard and R. Schellekens, *Synth. Met.*, 1995, 74, 65-70.

40. K.-y. Jen and R. Elsenbaumer, *Synth. Met.*, 1986, 16, 379-380.

41. W.-T. Chen, G. A. Bowmaker, J. M. Seakins and R. P. Cooney, *Synth. Met.*, 2002, 128, 215-220.

42. I. Hoogmartens, D. Vanderzande, H. Martens and J. Gelan, *Synth. Met.*, 1992, 47, 367-371.

43. M. Pomerantz, B. Chaloner-Gill, L. O. Harding, J. J. Tseng and W. J. Pomerantz, *Synth. Met.*, 1993, 55, 960-965.

44. L. Goris, M. A. Loi, A. Cravino, H. Neugebauer, N. S. Sariciftci, I. Polec, L. Lutsen, E. Andries, J. Manca, L. De Schepper and D. Vanderzande, *Synth. Met.*, 2003, 138, 249-253.

45. H. Paulussen, D. Vanderzande and J. Gelan, *Synth. Met.*, 1997, 84, 415-416.

46. I. Polec, A. Henckens, L. Goris, M. Nicolas, M. A. Loi, P. J. Adriaensens, L. Lutsen, J. V. Manca, D. Vanderzande and N. S. Sariciftci, *J. Polym. Sci., Part A: Polym. Chem.*, 2003, 41, 1034-1045.

47. M. J. Swann, G. Brooke, D. Bloor and J. Maher, *Synth. Met.*, 1993, 55, 281-286.

48. Y. Qin, J. Y. Kim, C. D. Frisbie and M. A. Hillmyer, *Macromolecules*, 2008, 41, 5563-5570.

49. A. Henckens, M. Knipper, I. Polec, J. Manca, L. Lutsen and D. Vanderzande, *Thin Solid Films*, 2004, 451-452, 572-579.

50. S. E. Shaheen, D. Vangeneugden, R. Kiebooms, D. Vanderzande, T. Fromherz, F. Padinger, C. J. Brabec and N. S. Sariciftci, *Synth. Met.*, 2001, 121, 1583-1584.

51. S. Curran, S. Roth, A. P. Davey, A. Drury and W. Blau, *Synth. Met.*, 1996, 83, 239-243.

52. D. L. Vangeneugden, D. J. M. Vanderzande, J. Salbeck, P. A. van Hal, R. A. J. Janssen, J. C. Hummelen, C. J. Brabec, S. E. Shaheen and N. S. Sariciftci, *The Journal of Physical Chemistry B*, 2001, 105, 11106-11113.

53. W. E. Tenhaeff and K. K. Gleason, *Adv. Funct. Mater.*, 2008, 18, 979-992.

54. H. Park, R. M. Howden, M. C. Barr, V. Bulović, K. Gleason and J. Kong, *ACS Nano*, 2012, 6, 6370-6377.

55. M. C. Barr, J. A. Rowehl, R. R. Lunt, J. Xu, A. Wang, C. M. Boyce, S. G. Im, V. Bulović and K. K. Gleason, *Adv. Mater.*, 2011, 23, 3500-3505.

56. S. G. Im, D. Kusters, W. Choi, S. H. Baxamusa, M. de Sanden and K. K. Gleason, *ACS Nano*, 2008, 2, 1959-1967.

57. D. C. Borrelli, M. C. Barr, V. Bulović and K. K. Gleason, *Sol. Energy Mater. Sol. Cells*, 2012, 99, 190-196.

58. S. G. Im and K. K. Gleason, *Macromolecules*, 2007, 40, 6552-6556.

59. J. P. Lock, J. L. Lutkenhaus, N. S. Zacharia, S. G. Im, P. T. Hammond and K. K. Gleason, *Synth. Met.*, 2007, 157, 894-898.

60. M. C. Barr, R. M. Howden, R. R. Lunt, V. Bulović and K. K. Gleason, *Advanced Energy Materials*, 2012, 2, 1404-1409.

61. J. P. Lock, S. G. Im and K. K. Gleason, *Macromolecules*, 2006, 39, 5326-5329.

62. D.-R. Hou, Y.-D. Hsieh and Y.-W. Hsieh, *Tetrahedron Lett.*, 2005, 46, 5927-5929.

63. R. M. Howden, E. D. McVay and K. K. Gleason, *Journal of Materials Chemistry A*, 2013, 1, 1334-1340.

64. M. Onoda, S. Morita, H. Nakayama and K. Yoshino, *Japanese Journal of Applied Physics*, 1993, 32, 3534.

65. W.-T. Chen, G. A. Bowmaker and R. P. Cooney, *Phys. Chem. Chem. Phys.*, 2002, 4, 4218-4225.

66. S. M. Dale, A. Glidle and A. R. Hillman, *J. Mater. Chem.*, 1992, 2, 99-104.

67. N. Colaneri, M. Kobayashi, A. J. Heeger and F. Wudl, *Synth. Met.*, 1986, 14, 45-52.

68. G. King and S. J. Higgins, *J. Chem. Soc., Chem. Commun.*, 1994, 0, 825-826.

69. W.-T. Chen, G. A. Bowmaker, J. M. Seakins and R. P. Cooney, *Appl. Spectrosc.*, 2002, 56, 909-915.

70. V. Hernandez, C. Castiglioni, M. Del Zoppo and G. Zerbi, *Phys. Rev. B*, 1994, 50, 9815-9823.

71. D. Lin-Vien, N. B. Colthup, W. G. Fateley and J. G. Grasselli, *The Handbook of Infrared and Raman Characteristic Frequencies of Organic Molecules*, Academic Press, 1991.

72. C. Quattrocchi, R. Lazzaroni, J. L. Bredas, R. Kiebooms, D. Vanderzande, J. Gelan and L. Van Meervelt, *The Journal of Physical Chemistry*, 1995, 99, 3932-3938.

73. K. Steliou, P. Salama and J. Corriveau, *The Journal of Organic Chemistry*, 1985, 50, 4969-4971.

74. R. P. Kreher and J. Kalischko, *Chem. Ber.*, 1991, 124, 645-654.

75. I. Hoogmartens, P. Adriaensens, R. Carleer, D. Vanderzande, H. Martens and J. Gelan, *Synth. Met.*, 1992, 51, 219-228.

76. W. Wallnöfer, E. Faulques, H. Kuzmany and K. Eichinger, *Synth. Met.*, 1989, 28, 533-538.

77. E. Faulques, W. Wallnofer and H. Kuzmany, *The Journal of Chemical Physics*, 1989, 90, 7585-7593.

78. P. Frère, J.-M. Raimundo, P. Blanchard, J. Delaunay, P. Richomme, J.-L. Sauvajol, J. Orduna, J. Garin and J. Roncali, *The Journal of Organic Chemistry*, 2003, 68, 7254-7265.

79. H. E. Schaffer, R. R. Chance, R. J. Silbey, K. Knoll and R. R. Schrock, *The Journal of Chemical Physics*, 1991, 94, 4161-4170.

80. M. Onoda, H. Nakayama, S. Morita and K. Yoshino, *J. Electrochem. Soc.*, 1994, 141, 338-341.

81. B. W. D'Andrade, S. Datta, S. R. Forrest, P. Djurovich, E. Polikarpov and M. E. Thompson, *Org. Electron.*, 2005, 6, 11-20.

Chapter 3

Effects of Deposition Pressure on the Optoelectronic Properties of oCVD Unsubstituted Polythiophene [*]

3.1 Abstract

Fabrication of devices utilizing unsubstituted polythiophene (PT) has received limited attention because thin films of this insoluble material have been difficult to prepare from traditional solution-based methods. However, since the thiophene monomer is volatile, PT films can be readily fabricated by oxidative chemical vapor deposition (oCVD). The pressure of the oCVD process significantly affects the optoelectronic properties of the PT films. Shifts in the Raman bands near 1500 cm^{-1} suggest that the lowest pressure deposition conditions (1 mTorr) result in shorter conjugation. Additionally, relative Raman peak intensities suggest that the polymer chains in these films contain more distortions than films deposited at higher pressures. UV-Vis absorption spectra of the oCVD PT films show that films deposited at the lowest pressure considered (1 mTorr) are slightly blue-shifted and demonstrate lower absorption than films deposited at higher pressures. PT films deposited at 75, 150, and 300 mTorr demonstrated similar UV-Vis absorption spectra, with absorption maxima near 515 nm. Organic thin film transistors (TFTs) were fabricated using oCVD PT as the active channel layer to analyze the effect of deposition pressure on charge transport and electrical properties. Films deposited at 150 mTorr demonstrate the greatest field effect carrier mobility of 4×10^{-3} cm^2 $V^{-1}sec^{-1}$.

3.2 Introduction

In addition to the choice of materials, the processes used for fabricating polymer electronics greatly affect how the devices perform. The selected synthetic and purification routes impact material purity, molecular weight, and regioregularity, which can all influence device performance.[1-6] Additionally, the microstructure and crystallinity of polymer films are known to be important considerations for optimizing film properties.[7-10]

Oxidative chemical vapor deposition (oCVD) is a promising technique that can be used to process conjugated polymers. Unlike most solution deposition techniques, during oCVD polymers films are simultaneously synthesized and deposited. Monomer and oxidizing agent precursor vapors react on the substrate to deposit polymer films. This enables facile film formation, even for unsubstituted and insoluble polymers which are difficult to process by standard methods. oCVD has been used to deposit conducting and semiconducting films for numerous applications, including organic photovoltaics, electrochromic devices, and others.[11-13]

Many oCVD process parameters influence the resulting polymer properties. Previous studies have shown that increased substrate deposition temperature increases conjugation length in poly(isothianaphthene) and poly(3,4-ethylenedioxythiophene) (PEDOT) and lowers PEDOT work function.[14-16] Additionally, post-deposition acid rinsing was shown to effectively increase PEDOT conductivity.[17] Optimization of the oxidizing agent and monomer delivery rates is also important for obtaining high quality films.

Here we analyze the effects of oCVD chamber pressure on the resulting properties of unsubstituted polythiophene (PT). The Raman spectra, UV-vis absorption spectra and film morphology are measured. In order to better characterize the electrical properties of the films, we prepared organic thin film transistors (TFTs) using oCVD PT as the active channel layer. From the TFT device performances and by using TFT transmission line model (TLM) measurements we systematically investigated the conductivity, carrier mobility, and carrier density in oCVD PT films. In addition to providing greater characterization of the oCVD process, this study expands the knowledge of unsubstituted polythiophene, which has traditionally been difficult to incorporate into organic electronics because of its insolubility. Fundamental knowledge of PT is likely to benefit the understanding of its many substituted variants.

3.3 Experimental

Polythiophene films were prepared using oxidative chemical vapor deposition (oCVD) in a custom-built reactor. The general oCVD process and basic reactor configuration are described in detail elsewhere.[15, 18] However, a newly-constructed reactor was used for this study. The reactor body was a stainless steel cube of 41 cm on each side. Monomer is held in a temperature-controlled glass jar outside of the reactor and feed into the chamber through an inlet port. A dry pump (Edwards, iQDP40 with a QMB250 mechanical booster) was used to achieve vacuum through an exhaust port opposite from the monomer inlet port. A butterfly-type throttling valve (MKS Instruments, Model 653B) was used to maintain pressures above 50 mTorr. A turbomolecular pump (Pfeiffer Vacuum, HiPace 300C) was used to achieve higher vacuum. At the bottom of the chamber are four low temperature evaporation (LTE) point sources (Kurt J. Lesker Co.) designed to deposit volatile organic materials. Each point source is off-centered and slightly angled (~30° from vertical) towards the stage, which is approximately 20 cm away. Only one point source evaporator was used in this study and it was used to heat a crucible holding the iron(III) chloride oxidizing agent. The substrate stage was at the top of the reactor chamber and inverted to face down. The stage is capable of rotating, which greatly contributes to improved uniformity of samples over the entire stage surface (21 cm in diameter). An active pirani/cold cathode transmitter vacuum gauge (Pfeiffer Vacuum, PKR 261) was used to monitor pressures below 10 mTorr. Higher pressures were read with an absolute capacitance manometer (MKS Instruments, Model 628D).

Thiophene monomer vapors reacted via oxidative polymerization with sublimated oxidizing agent (iron(III) chloride) to result in the deposition of solid, polymer films on the stage. Thiophene ($\geq 99\%$, Sigma-Aldrich) and iron(III) chloride ($FeCl_3$, 97%, Sigma-Aldrich) were used as purchased. Glass slides and thermally oxidized (50 nm) silicon wafers (SiO_2/Si) were used as

substrates. Thiophene vapors were delivered into the reactor chamber and directed toward the substrate stage. The thiophene monomer jar was maintained at a temperature of 20 °C and a needle valve was used to control the flow rate. A total gas flow rate of ~31 sccm was used for all deposition conditions. oCVD PT films were deposited at the following pressures for this study: 1, 75, 150, and 300 mTorr. $FeCl_3$ was used as the oxidizing agent and its crucible was heated from room temperature to 130 °C at 8 °C/min, and 130 °C to the final heating temperature at 4 °C/min. The final heating temperatures for depositions at 1, 75, 150, and 300 mTorr were 170, 190, 200, and 225 °C, respectively. The stage was rotated at approximately 3 rotations per minute during the depositions. The stage and reactor body were unheated for this study. Samples deposited at 75, 150, and 300 mTorr were deposited in 25 minutes, while samples at 1 mTorr were deposited in 40 minutes. After deposition, the samples were all sequentially rinsed in methanol ($\geq$99.9%, Sigma-Aldrich) for 30 minutes, 0.2M HCl in methanol for 10 minutes, and 1 minute in methanol to remove reacted and excess oxidant.

UV-Vis absorption spectra of the films deposited on glass slides were measured with a Varian Cary 5000 UV-vis spectrophotometer. Absorption coefficient (α) values were calculated as:

$$\alpha = \frac{-1}{d}\ln\left(\frac{T}{1-R}\right)$$

where d is the film thickness, T is the fraction of incident light transmitted through the film, and R is the fraction of incident light reflected by the film. A specular reflectance accessory and an aluminum standard reference mirror (ThorLabs) were used to measure sample absolute reflection. Film thicknesses were measured using a Veeco Dektak 150 surface profilometer. Morphologies of the thin films were measured using an Agilent Technologies AFM in tapping

mode with a Bruker Si cantilever having a tip frequency of 330 kHz. Raman spectra were taken with a Horiba Jobin-Yvon LabRam Raman Confocal Microscope with a 532 nm laser. The XRD measurements were taken with a Scintag Theta-Theta diffractometer (model PAD-X), using Cu Kα radiation.

Bottom-gated thin film transistor (TFT) devices were fabricated on heavily doped p-type single crystalline (100) Si (0.003-0.005 Ωcm) substrates. In these devices, thermally grown 50 nm-thick SiO_2 was used as the gate dielectric which presents a smooth and uniform surface for the channel layer deposition. The channel polythiophene was deposited on SiO_2/Si substrates using oCVD in the conditions described above. For source/drain metallizations, 50 nm of Ag was deposited by thermal evaporation at a deposition rate of 0.1 nm/sec. The channel and source/drain electrode patterns were vapor-printed by in-situ shadow masking. Gate metallization back side contact was made by scratching the wafer surface with a diamond scriber to ensure the removal of any native oxides and exposing heavily-doped Si. Device performance was measured on at least nine PT TFTs for each deposition condition. Characterization was performed in air in a light-tight probe station at room temperature with an Agilent B1500A semiconductor device parameter analyzer.

3.4 Results and discussion

3.4.1 oCVD Depositions

Polythiophene (PT) was simultaneously synthesized and deposited as thin films using oCVD at various deposition pressures. The oCVD process results in doping of the polythiophene films due to excess oxidizing agent that makes the film conductive[12]. Thus, a post-deposition rinse of the films in methanol and dilute acid was used to dedope the films to the semiconducting form and remove residual oxidant.

Analogous to most physical vapor deposition processes, the rate of $FeCl_3$ delivery to the substrate is highly dependent on several variables, including: distance between substrate and source (205 mm in this case), chamber pressure, and source temperature. The mean free path (λ) of a molecule in the chamber can be calculated using standard kinetic theory as:

$$\lambda = \frac{k_B T}{\sqrt{2}\pi d^2 P}$$

where k_B is the Boltzmann constant, T is the temperature, d is the gas molecule diameter, and P is the pressure.[19] The mean free path in the chamber is 32.8 mm when at a pressure of 1 mTorr, assuming a thiophene kinetic diameter of 0.46 nm.[20] Increasing the pressure to 75, 150, and 300 mTorr significantly decreases the mean free path to 0.44, 0.22 and 0.11 mm, respectively.

PT film properties are dependent on the flow rates of the $FeCl_3$ and monomer. The $FeCl_3$ final heating temperatures for this study were determined to approximately optimize the relative $FeCl_3$ and monomer delivery rates to the substrate at the four deposition pressures considered (Table 3-1, conditions A, B, C, and E).

Table 3-1. Summary of oCVD deposition conditions used in this study.

Condition	Pressure (mTorr)	$FeCl_3$ Final Heating Temp (°C)	Time (min)	Thickness (nm)
A	300	225	25	27
B	150	200	25	34
C	75	190	25	42
D	10 mTorr thiophene + 140 mTorr N_2	200	25	48
E	1	170	40	23
F	1	175	40	31

For these conditions, the optimum was characterized by minimal excess FeCl3 as seen in the rinsing step and maximization of the absorption spectrum peak position and TFT mobility. Film D was included to study the impact of lower monomer concentration while maintaining identical overall pressure and FeCl3 temperature (compared to condition B). Film F was included as an example of a film with a slight excess of FeCl3 (compared to condition E).

For the increasing pressure series of 75, 150, and 300 mTorr (conditions C, B, and A) one might expect the growth rate to increase in response to the increased monomer concentration. However, the oxidant delivery temperature needed to be increased to obtain somewhat comparable film growth rates at higher pressures. This observation suggests that the delivery rate of oxidant to the substrate is the rate limiting step at these three conditions. To test this hypothesis, a comparison was made between conditions B and D. Both have the same total pressure and final oxidant heating temperature. However, condition B uses pure monomer while condition D is a mixture of only 6.7 mole % monomer in nitrogen. This decrease in monomer concentration was observed to actually increase the growth rate. This confirms that the rate of oxidant delivery is rate limiting at the higher pressures in this study. The oxidant is required to form the reactive radical cation growth species.18 Thus, at lower monomer pressures a higher percentage could be activated by the oxidant, resulting in a higher reaction rate. Lastly, the two films deposited at 1 mTorr grew at a slower rate than those at higher pressures and a slightly longer deposition time of 40 minutes was used (Table 3-1, conditions E and F).

The Knudsen number (Kn = λ/L), calculated as the ratio of the mean free path to the distance between the source and the stage, decreases from 0.002 to 0.0005 for increasing pressure from 75 to 300 mTorr. Therefore, evaporation at these pressures is non-line-of-sight as mass transport in the chamber is in the continuum diffusion regime. In this regime delivery of the oxidant

to the substrates becomes slower with increased pressures, hence the need to increase the crucible temperature at higher pressures. At 1 mTorr Kn = 0.2, suggesting that it is in the transition regime and more line of sight. Thus a slightly lower crucible temperature is required at 1 mTorr.

3.4.2 Raman

The Raman spectra of all films share very similar features, with strong bands in the 1400 – 1500 cm^{-1} region (Figure 3-1a). The C=C symmetric stretching band position at ~1460 cm^{-1} is known to be essentially independent of conjugation length.[21] All the oCVD PT films have almost identical vibrational peak positions of around 1457 cm^{-1}.
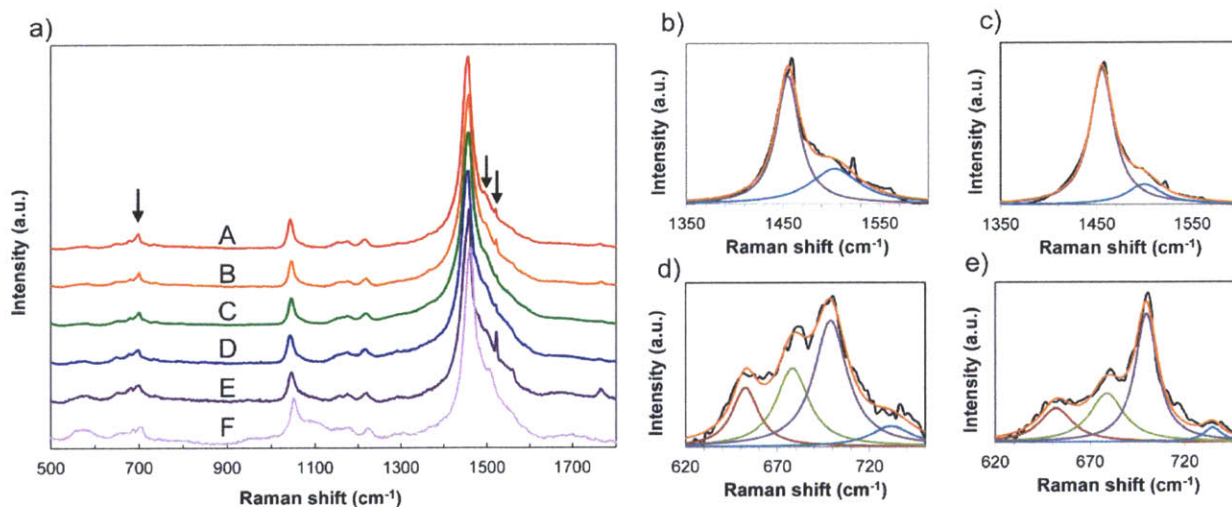
Figure 3-1. a) Raman spectra of oCVD PT films deposited under various conditions. The arrows point to bands of interest around 1520, 1500, and 700 cm^{-1} that can be used to estimate conjugation length and relative distortion in the polymer chains. **b)** and **c)** Raman bands near 1450 and 1500 cm^{-1} for conditions E and B, respectively. **d)** and **e)** Raman bands of films near 700 cm^{-1} from conditions E and B, respectively.

In contrast, the Raman band near 1500 cm^{-1}, which is assigned to the C=C antisymmetric stretching vibration, has been shown to downshift in position and decrease in intensity with increased conjugation[21]. These peaks are very weak in the oCVD PT films, suggesting a high level

of conjugation in the films. Estimates for the maximum in the weak vibration band are listed in Table 3-2. This band appears at 1519, 1504-1507, and 1502 cm^{-1} in α-quarterthiophene, α-sexithiophene, and α-octithiophene, respectively.[21, 22] Thus the two oCVD samples deposited at 1 mTorr (E and F) appear to have the lowest conjugation lengths. Additionally, most of the oCVD films have peaks of varying intensity near 1520 cm^{-1} (Figure 3-1a). This could be due to either the existence of shorter PT chains or increased rotation of thiophene rings out of coplanarity that disrupts conjugation and confines π electrons.[23] Notably, this peak is strongest in condition E and at the highest position of 1523 cm^{-1}, consistent with conjugation over about four thiophene rings. With higher $FeCl_3$ delivery rate at the same pressure (condition F), this additional peak near 1520 cm^{-1} almost completely disappears.

The four weak bands in the 620 – 750 cm^{-1} region are believed to be due to C-S-C thiophene ring vibrations. The ~700 cm^{-1} band arises from vibrations in coplanar thiophene rings, while bands at ~682 and ~652 cm^{-1} are due to the distorted parts of the polymer chain.[21] Thus the peak intensity ratio I_{682}/I_{700} can be used to compare the relative amounts of distortions in the chains, with a larger ratio corresponding to more chain distortions.[24-26] The sample spectra were decomposed into four bands with Lorentzian distributions to aid this analysis. Example nonlinear least square fits along with individual components are shown for condition E (Figure 3-1b and 3-1d) and condition B (Figure 3-1c and 3-1e) in two regions of interest. As shown by the values listed in Table 3-2, films from conditions A, B, C demonstrated the least amount of chain distortion while films deposited at 1 mTorr (E and F) show the highest amount of chain distortions.

Table 3-2. Summary of oCVD PT properties for conditions analyzed in this study.

Condition	RMS roughness (nm)	λ_{max} (nm)	Raman shift v (cm^{-1})	Raman I_{682}/I_{700}
A	19.3	516	1500	0.38
B	33.2	515	1500	0.38
C	18.9	514	1498	0.39
D	35.1	517	1498	0.48
E	26.9	495	1503	0.62
F	23.3	503	1505	0.67

3.4.3 UV-Vis Absorption

Figure 3-2a shows the absorption spectra of samples from all six deposition conditions. The four higher pressure conditions (A through D) exhibit an absorption shoulder at ~585 nm, which is much better defined than in the lower pressure samples (E and F). A similar absorption shoulder is seen in films of poly(3-hexylthiophene) (P3HT), a soluble derivative of PT, and is attributed to interchain interactions from chain aggregation.[27, 28] A significant majority of PT spectra in the literature do not exhibit this absorption shoulder.[24, 29-36] This may be due to the difficulty in controlling film morphology via conventional methods used for depositing films of insoluble PT.

Deposition pressure impacts how strongly the oCVD PT films absorb. PT films deposited at 1 mTorr (E and F) have much lower absorption coefficients (α) than the films deposited at higher pressures. The film deposited at 300 mTorr has the highest absorption. These results are summarized in Figure 3-2b, which shows the absorption coefficient at 515 nm for each film.

Films from the four higher pressure conditions (A through D) have almost identical absorption maxima at around 515 nm (Figure 3-2c). In contrast, however, the films deposited at much lower pressure (E and F) are blue-shifted relative to the higher pressure conditions. This suggests lower conjugation in the films deposited at 1 mTorr. Using a higher $FeCl_3$ temperature

67

(and thus higher FeCl$_3$ delivery rate) for Film F versus Film E resulted in a slight red-shift in the absorption maxima.
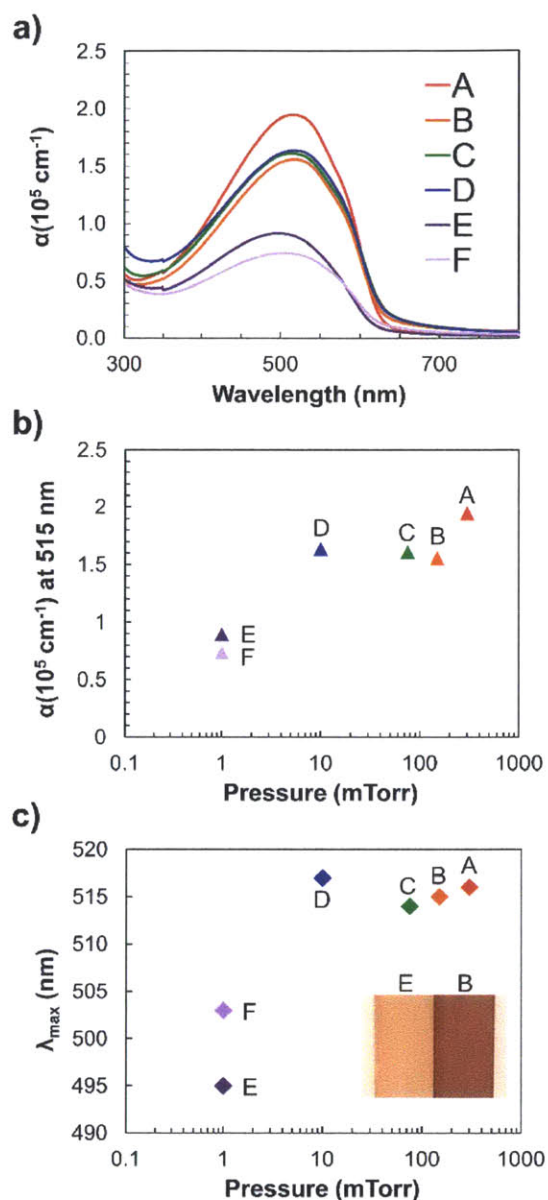
Figure 3-2. a) UV-vis absorption spectrum of oCVD PT films deposited at various pressures. The film deposited at 1 mTorr shows much greater transparency. **b)** Absorption coefficient of the six films at 515 nm as a function of monomer partial pressure. **c)** The position of the absorption maximum for the six PT films as a function of monomer partial pressure.

Films E and F demonstrate absorption maxima at 495 and 503 nm, respectively. Changes in the color of polymer films deposited under different deposition conditions hinted at the changes in their optical properties. The four PT films deposited at higher total pressures (A through D) appeared dark red with a slight purplish tint. In contrast, the two films deposited at the lowest pressure (E and F) appeared to have a pinkish-orange color. The inset in Figure 3-2c shows a picture of Films E and B on glass as examples.

We hypothesize that the differences in the absorption spectra of the oCVD PT deposited under different conditions are due to a combination of decreased conjugation in the chains and increased disorder. Thiophene-based oligomers demonstrate red-shifting and stronger absorption with increasing chain length and conjugation.[37, 38] Changes in the degree of order and disorder in P3HT films have been shown to affect its absorption properties as well. Annealing composite films of poly(3-hexylthiophene)/[6,6]-phenyl C_{61} butryic acid methyl ester (P3HT/PCBM) can greatly increase absorption at each wavelength and also red-shift the absorption peak by over 60 nm.[39, 40] This change was attributed to the increased crystallinity of the films from the conversion of an amorphous matrix to domains of aggregated P3HT.[41] Conformational defects that rotate monomer units out of plane are also known to reduce conjugation. For example, heating P3HT up to 190 °C introduces disorder into polymer film that reduces the conjugation length and blue-shifts the absorption spectrum by over 70 nm.[42] Furthermore, the absorption coefficient of P3HT was shown to increase with increasing regioregularity because of improved interplane and intraplane stacking.[5]

The spectra of Films B and D are almost identical, despite condition D having significantly lower thiophene pressure (Figure 3-2a). This suggests that the overall pressure is an important parameter for the resulting polymer film properties. At the very low pressures (E and F) the $FeCl_3$

has fewer vapor species competing for the same surface sites. This might allow the $FeCl_3$ to more easily crystallize, as it is known to form crystals.[43] The $FeCl_3$ crystals may disrupt the formation of well-stacked polymer chains and result in lower effective conjugation lengths. This also potentially explains the slightly lower absorption in Film F versus Film E (Figure 3-2a) despite having a more red-shifted absorption maximum (Figure 3-2c). The higher $FeCl_3$ delivery rate for Film F may allow the $FeCl_3$ to further disrupt interchain stacking. This explanation is also consistent with the Raman results, which showed higher chain distortions in films E and F that could lower the effective conjugation in the films. At higher pressures, $FeCl_3$ crystallization might be hindered by competing vapor molecules and a greater chance of reaction in the gas phase due to the lower mean free path.

Lastly, it is also important to note that it is not necessarily a negative result to obtain films with lower absorption. For applications in which it is desirable for the polymer to absorb light, such as an active layer material in an organic solar cell, higher absorption coefficients are beneficial. However, for use as a transparent conducting polymer electrode, greater transparency would improve performance.

3.4.4 Morphology

Figure 3-3 shows tapping mode AFM topographic images of oCVD PT films deposited under various deposition conditions. The root mean square (RMS) roughness values for the films are listed in Table 3-2. These films are slightly smoother than PT films prepared by other techniques such as plasma polymerization and electropolymerization.[31, 44, 45] Additionally, it is possible to obtain much smoother films using a lower monomer flowrate than that used for this study. Both samples deposited at 150 mTorr total pressure (B and D) have higher surface roughness than the rest of the samples.

70

The film morphologies vary considerably under the different deposition pressures. Samples from condition A (300 mTorr) demonstrate much smaller and well-defined morphological features than the rest of the conditions. Additionally, films deposited at Condition D show interesting surface features. oCVD PEDOT films deposited using $CuCl_2$ as the oxidizing agent showed somewhat similar features.[46] The porosity of the PEDOT films was attributed to the collapse of bubbles formed by the release of gaseous byproducts from the polymerization process. A similar phenomenon might be occurring in Film D due to its slightly higher polymerization rate compared to Film B (Table 3-1).
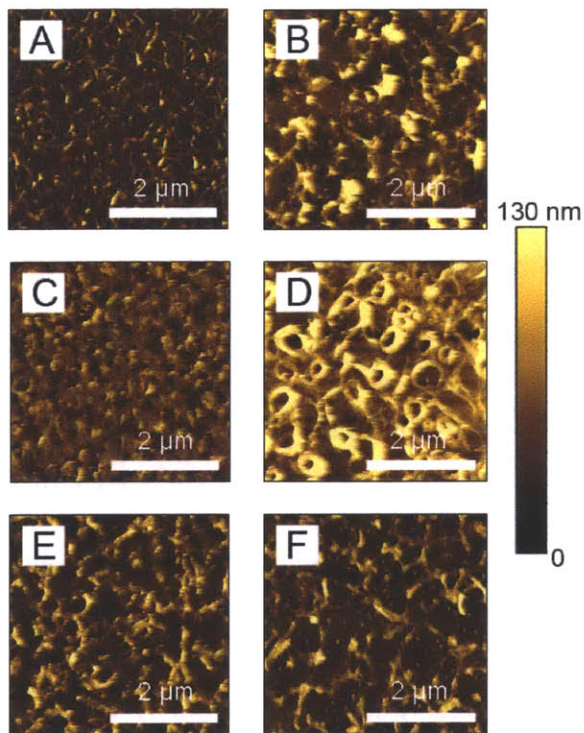
Figure 3-3. AFM topography images of oCVD PT films under various deposition conditions.

Despite the UV-Vis data suggesting higher interchain interactions, none of the XRD scans of the oCVD PT films showed evidence of crystallinity (Figure 3-4). Thus the order is likely at the nanocrystalline level and beyond the detection capability of the XRD used.
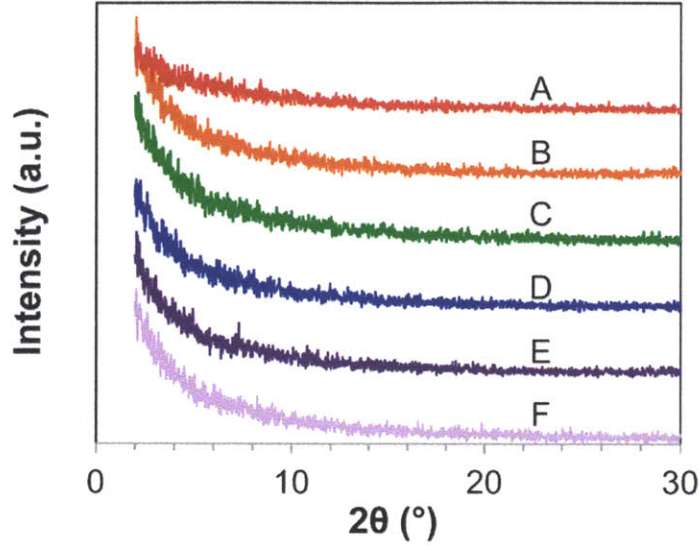
Figure 3-4. XRD scans of oCVD PT films show that the films are amorphous.

3.4.5 TFT Properties

oCVD PT thin films were then successfully integrated as thin film transistor (TFT) active channel layers to allow for the extraction of electrical properties, such as carrier mobility and concentrations, and, hence, conductivity. The TFTs were fabricated on thermally oxidized Si wafers (SiO_2/Si) and the channel PT layers were deposited at the conditions listed in Table 3-1. The complete bottom-gated device structure is shown schematically in Figure 3-5a.

Condition B (150 mTorrr) provided the highest on-current and field effect mobility in this study. Figure 3-5b shows the drain current (I_D) in these devices as the drain bias (V_D) was swept from 0 to -25 V for a series of gate voltages (V_G) from 12 to -21 V at 3 V intervals. Since no current crowding was observed in the initial sweep of output characteristics, Ohmic contact was confirmed between the PT channel and silver source/drain metallizations.

The transfer characteristics (I_D-V_G) were investigated by setting the drain bias so that the devices were well into the saturation regime (V_D = -25 V in this study), then sweeping the gate voltage (V_G) to make the device on and off within the range arising no device break-down. Figure

3-5c presents the transfer characteristics using channel films deposited under the various oCVD deposition conditions. PT TFTs processed at 75, 150 and 300 mTorr show the drain current on/off ratio of approximately 10^3, while devices using samples deposited at 1 mTorr (E and F) have a much lower value of $\sim 10^1$. Devices with PT deposited under condition D (10 mTorr with N_2) have an on/off ratio in between that of the other devices at $\sim 10^2$. The off-current for devices using condition B (150 mTorr) is slightly larger than for TFTs using PT films deposited at other pressures, likely due to higher PT channel conductivity. The device drain current in the saturation regime is a function of the field effect mobility and threshold voltage as shown in equation (1):

$$I_D = \mu_{FE} C_{ox} \frac{W}{2L}(V_G - V_{Th})^2$$

(1)

This equation relates the saturation current (I_D) to the field effect mobility (μ_{FE}), oxide capacitance ($C_{ox} = 6.903 \times 10^{-8}$ F/cm^2 for 50 nm-thick SiO_2), the device aspect ratio (W/L), the applied gate voltage (V_G), and the threshold voltage (V_{Th}).
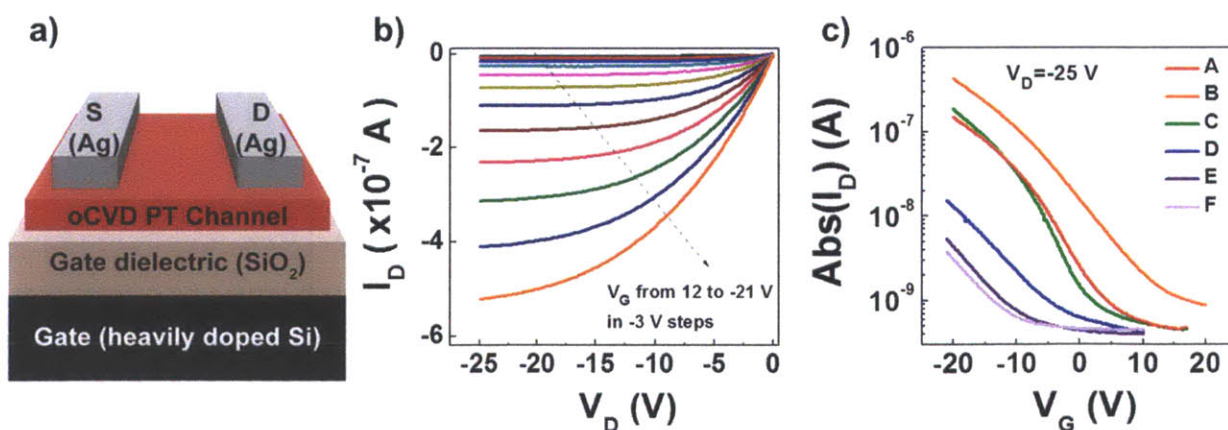
Figure 3-5. Polythiophene-based TFT device applications: **(a)** schematic of bottom-gated TFT structure with channel width/length W/L = 2000 μm/60 μm, **(b)** typical output characteristics of TFTs using condition B (150 mTorr) oCVD PT, and **(c)** transfer characteristics of absolute I_D vs V_G measured at fixed V_D of -25 V.

Figure 3-6a shows the resulting field effect mobility from the analysis using equation (1). For PT films grown at the lowest pressure (1 mTorr), the hole mobility is also the lowest ($\sim 4 \times 10^{-4}$ and $\sim 2 \times 10^{-4}$ cm^2 V^{-1}sec^{-1} for E and F, respectively). A maximum hole mobility of $\sim 4 \times 10^{-3}$ cm^2 V^{-1}sec^{-1} is observed for the PT deposited at a pressure of 150 mTorr (condition B). This mobility value is slightly higher than those in the literature of electropolymerized PT in the neutral (1×10^{-5} to 6.9×10^{-5} cm^2 V^{-1}sec^{-1}) and doped forms (1×10^{-3} cm^2 V^{-1}sec^{-1}).[47-50] At the highest growth pressure (condition A, 300 mTorr), the carrier mobility slightly decreases to $\sim 2 \times 10^{-3}$ cm^2 V^{-1}sec^{-1}.
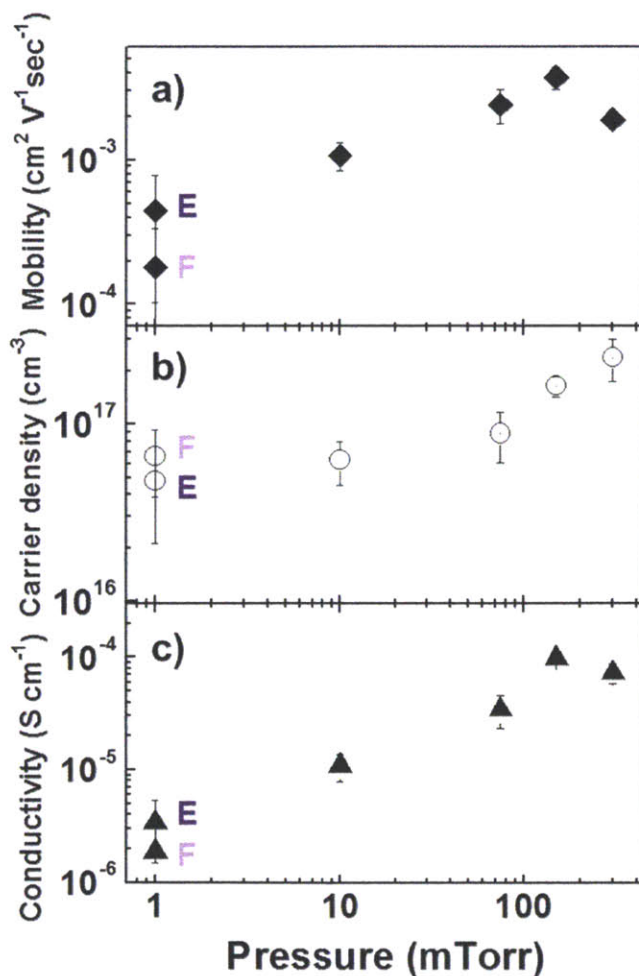
Figure 3-6. Electrical properties of the carrier mobility and density, and the overall conductivity of oCVD PT thin films as a function of monomer partial pressure.

The electrical characterization of the transport properties of the highly resistive thin PT samples via either Hall methods or a four point probe is difficult because the field required to drive measureable sample current is large. The transmission line model (TLM) is an alternative method to determine the channel sheet resistance and the interfacial contact resistance in TFT device applications.[51, 52] In this work, TFT TLM measurements were employed to investigate the channel conductivity (σ_{ch}) and the carrier density. The channel conductivity was calculated from the channel sheet resistance extracted using TLM and the measured thickness. The carrier density (p) was then obtained by using the relation of $\sigma = qp\mu$ with the values of the channel conductivity (σ_{ch}) and field effect mobility (μ_{FE}). More detailed TLM procedure can be found elsewhere.[51-53] Figure 3-6b presents the carrier density of the channel PT films and shows that the carrier density increases with increasing deposition pressure. Conductivity of doped PT films have been shown to be inversely correlated with the Raman bands intensity ratio of I_{682}/I_{700}.[53, 54] Trends in the mobility and conductivity correlate well with trends in I_{682}/I_{700} from Raman measurements, as listed in Table 3-2. The overall conductivity of oCVD polythiophene films with pressure is given in Figure 3-6c. The electrical properties and device performance are summarized in Table 3-3.

Table 3-3. oCVD polythiophene-based TFT device parameters

Condition	Mobility $(cm^2 V^{-1}s^{-1})$	Carrier density (cm^{-3})	I_D on/off	V_{TH} (V)
A	1.90×10^{-3}	2.38×10^{17}	$\sim 10^3$	-3.44
B	3.74×10^{-3}	1.65×10^{17}	$\sim 10^3$	-0.74
C	2.42×10^{-3}	0.89×10^{17}	$\sim 10^3$	-5.90
D	1.08×10^{-3}	0.63×10^{17}	$\sim 10^2$	-8.32
E	4.45×10^{-4}	0.48×10^{17}	$\sim 10^1$	-9.56
F	1.80×10^{-4}	0.66×10^{17}	$\sim 10^1$	-8.05

3.5 Conclusions

Properties of oCVD unsubstituted polythiophene were analyzed under various deposition conditions. In particular, an emphasis was placed on studying the effects of pressure. Films deposited at the lowest pressure (1 mTorr) polymerized at a slower rate and required longer process times. These films demonstrated lower absorption, a lower degree of conjugation, and a higher amount of polymer chain distortions than films deposited at the higher pressure conditions used in this study. The decreased absorption at this low pressure may be desirable for depositing transparent conductive polymers as electrodes. PT films deposited at 75, 150, and 300 mTorr demonstrated very similar UV-Vis absorption and Raman spectra to each other. Although crystallinity was not detected in the XRD measurements taken, the Raman measurements, absorption spectra, and TFT mobilities gave insight into changes in order in the films at different conditions. Specifically, the higher pressure films (A through D) demonstrated much more order and higher field effect mobility than films deposited at 1 mTorr (E and F). Films deposited at 150 mTorr demonstrate the greatest field effect carrier mobility of 4×10^{-3} cm^2 V^{-1}sec^{-1}. This is the highest reported mobility value for unsubstituted polythiophene. Thus the chamber pressure is an important process parameter that can be used to tune the properties of oCVD films for applications in organic electronics.

3.6 Acknowledgments

3.7 References

1.   M. Urien, G. Wantz, E. Cloutet, L. Hirsch, P. Tardy, L. Vignau, H. Cramail and J.-P. Parneix, *Org. Electron.*, 2007, 8, 727-734.
2.   R. J. Kline, M. D. McGehee, E. N. Kadnikova, J. Liu and J. M. J. Fréchet, *Adv. Mater.*, 2003, 15, 1519-1522.
3.   R. J. Kline, M. D. McGehee, E. N. Kadnikova, J. Liu, J. M. J. Fréchet and M. F. Toney, *Macromolecules*, 2005, 38, 3312-3319.
4.   P. Schilinsky, U. Asawapirom, U. Scherf, M. Biele and C. J. Brabec, *Chem. Mater.*, 2005, 17, 2175-2180.
5.   Y. Kim, S. Cook, S. M. Tuladhar, S. A. Choulis, J. Nelson, J. R. Durrant, D. D. C. Bradley, M. Giles, I. McCulloch, C.-S. Ha and M. Ree, *Nat Mater*, 2006, 5, 197-203.
6.   H. Sirringhaus, P. J. Brown, R. H. Friend, M. M. Nielsen, K. Bechgaard, B. M. W. Langeveld-Voss, A. J. H. Spiering, R. A. J. Janssen, E. W. Meijer, P. Herwig and D. M. de Leeuw, *Nature*, 1999, 401, 685-688.
7.   M. Campoy-Quiles, T. Ferenczi, T. Agostinelli, P. G. Etchegoin, Y. Kim, T. D. Anthopoulos, P. N. Stavrinou, D. D. C. Bradley and J. Nelson, *Nat Mater*, 2008, 7, 158-164.
8.   G. Li, V. Shrotriya, J. Huang, Y. Yao, T. Moriarty, K. Emery and Y. Yang, *Nat Mater*, 2005, 4, 864-868.
9.   J.-F. Chang, B. Sun, D. W. Breiby, M. M. Nielsen, T. I. Sölling, M. Giles, I. McCulloch and H. Sirringhaus, *Chem. Mater.*, 2004, 16, 4772-4776.
10.   Z. Bao, A. Dodabalapur and A. J. Lovinger, *Appl. Phys. Lett.*, 1996, 69, 4108-4110.
11.   M. C. Barr, J. A. Rowehl, R. R. Lunt, J. Xu, A. Wang, C. M. Boyce, S. G. Im, V. Bulović and K. K. Gleason, *Adv. Mater.*, 2011, 23, 3500-3505.
12.   D. C. Borrelli, M. C. Barr, V. Bulović and K. K. Gleason, *Sol. Energy Mater. Sol. Cells*, 2012, 99, 190-196.
13.   D. Bhattacharyya, R. M. Howden, D. C. Borrelli and K. K. Gleason, *J. Polym. Sci., Part B: Polym. Phys.*, 2012, 50, 1329-1351.
14.   D. C. Borrelli and K. K. Gleason, *Macromolecules*, 2013, 46, 6169-6176.
15.   S. G. Im and K. K. Gleason, *Macromolecules*, 2007, 40, 6552-6556.
16.   S. G. Im, K. K. Gleason and E. A. Olivetti, *Appl. Phys. Lett.*, 2007, 90, 3.
17.   R. M. Howden, E. D. McVay and K. K. Gleason, *Journal of Materials Chemistry A*, 2013, 1, 1334-1340.
18.   J. P. Lock, S. G. Im and K. K. Gleason, *Macromolecules*, 2006, 39, 5326-5329.
19.   J. F. O'Hanlon, *A User's Guide to Vacuum Technology*, Wiley Interscience, Hoboken, New Jersey, Third Edition edn., 2003.
20.   S. Goel, Z. Wu, S. I. Zones and E. Iglesia, *J. Am. Chem. Soc.*, 2012, 134, 17688-17695.
21.   Y. Furukawa, M. Akimoto and I. Harada, *Synth. Met.*, 1987, 18, 151-156.
22.   G. Louarn, J. P. Buisson, S. Lefrant and D. Fichou, *The Journal of Physical Chemistry*, 1995, 99, 11399-11404.

23. J. T. Lopez Navarrete and G. Zerbi, *The Journal of Chemical Physics*, 1991, 94, 965-970.
24. S. Nejati and K. K. S. Lau, *Langmuir*, 2011, 27, 15223-15229.
25. J. L. Sauvajol, G. Poussigue, C. Benoit, J. P. Lere-Porte and C. Chorro, *Synth. Met.*, 1991, 41, 1237-1242.
26. E. A. Bazzaoui, G. Levi, S. Aeiyach, J. Aubard, J. P. Marsault and P. C. Lacaze, *The Journal of Physical Chemistry*, 1995, 99, 6628-6634.
27. P. J. Brown, D. S. Thomas, A. Köhler, J. S. Wilson, J.-S. Kim, C. M. Ramsdale, H. Sirringhaus and R. H. Friend, *Phys. Rev. B*, 2003, 67, 064203.
28. J. Clark, C. Silva, R. H. Friend and F. C. Spano, *Phys. Rev. Lett.*, 2007, 98, 206406.
29. M. Kobayashi, J. Chen, T. C. Chung, F. Moraes, A. J. Heeger and F. Wudl, *Synth. Met.*, 1984, 9, 77-86.
30. K. Kaneto, Y. Kohno and K. Yoshino, *Solid State Commun.*, 1984, 51, 267-269.
31. R. Valaski, C. D. Canestraro, L. Micaroni, R. M. Q. Mello and L. S. Roman, *Sol. Energy Mater. Sol. Cells*, 2007, 91, 684-688.
32. K. Kaneto, K. Yoshino and Y. Inuishi, *Solid State Commun.*, 1983, 46, 389-391.
33. R. M. Eales and A. R. Hillman, *J. Mater. Sci.*, 1990, 25, 3806-3813.
34. C. A. Cutler, A. K. Burrell, G. E. Collis, P. C. Dastoor, D. L. Officer, C. O. Too and G. G. Wallace, *Synth. Met.*, 2001, 123, 225-237.
35. S. A. Gevorgyan and F. C. Krebs, *Chem. Mater.*, 2008, 20, 4386-4390.
36. M. C. Kim, S. H. Cho, S. B. Lee, Y. Kim and J. H. Boo, *Thin Solid Films*, 2004, 447–448, 592-598.
37. H. Chosrovian, S. Rentsch, D. Grebner, D. U. Dahm, E. Birckner and H. Naarmann, *Synth. Met.*, 1993, 60, 23-26.
38. P. Frère, J.-M. Raimundo, P. Blanchard, J. Delaunay, P. Richomme, J.-L. Sauvajol, J. Orduna, J. Garin and J. Roncali, *The Journal of Organic Chemistry*, 2003, 68, 7254-7265.
39. D. Chirvase, J. Parisi, J. C. Hummelen and V. Dyakonov, *Nanotechnology*, 2004, 15, 1317.
40. U. Zhokhavets, T. Erb, G. Gobsch, M. Al-Ibrahim and O. Ambacher, *Chem. Phys. Lett.*, 2006, 418, 347-350.
41. T. Erb, U. Zhokhavets, G. Gobsch, S. Raleva, B. Stühn, P. Schilinsky, C. Waldauf and C. J. Brabec, *Adv. Funct. Mater.*, 2005, 15, 1193-1196.
42. W. R. Salaneck, O. Inganäs, B. Thémans, J. O. Nilsson, B. Sjögren, J. E. Österholm, J. L. Brédas and S. Svensson, *The Journal of Chemical Physics*, 1988, 89, 4613-4619.
43. N. Caswell and S. A. Solin, *Solid State Commun.*, 1978, 27, 961-967.
44. M. Ito, A. Tsuruno, S. Osawa and K. Tanaka, *Polymer*, 1988, 29, 1161-1165.
45. N. V. Bhat and D. S. Wavhal, *J. Appl. Polym. Sci.*, 1998, 70, 203-209.
46. S. G. Im, D. Kusters, W. Choi, S. H. Baxamusa, M. de Sanden and K. K. Gleason, *ACS Nano*, 2008, 2, 1959-1967.
47. A. Tsumura, H. Koezuka and T. Ando, *Appl. Phys. Lett.*, 1986, 49, 1210-1212.
48. H. Koezuka, A. Tsumura and T. Ando, *Synth. Met.*, 1987, 18, 699-704.
49. H. Koezuka and A. Tsumura, *Synth. Met.*, 1989, 28, 753-760.
50. A. Tsumura, H. Koezuka and T. Ando, *Synth. Met.*, 1988, 25, 11-23.
51. S. Lee, H. Park and D. C. Paine, *J. Appl. Phys.*, 2011, 109, -.
52. H. H. Berger, *Solid-State Electronics*, 1972, 15, 145-158.
53. S. Lee, H. Park and D. C. Paine, *Thin Solid Films*, 2012, 520, 3769-3773.
54. M. Akimoto, Y. Furukawa, H. Takeuchi, I. Harada, Y. Soma and M. Soma, *Synth. Met.*, 1986, 15, 353-360.

Chapter 4

Planar Heterojunction OPVs Using oCVD Unsubstituted Polythiophene Donor Layers *

4.1 Abstract

We demonstrate the use of a vacuum-based, vapor phase technique for the deposition of a donor polymer for use in polymer solar cells. Unsubstituted polythiophene (PT), which is insoluble and infusible and thus typically difficult to process, is easily prepared by oxidative chemical vapor deposition (oCVD). The oCVD process results in a conductive PT film that is heavily doped with $FeCl_3$, which is used as the oxidizing agent. A post-deposition methanol rinse sufficiently dedopes the film and removes spent oxidant, leaving semiconducting PT with an optical bandgap close to 2 eV. Drastic changes in the film color, absorption spectra, and film composition confirm the dedoping process. The resulting semiconducting PT is then applied as an electron donor in bilayer heterojunction solar cells with a thermally evaporated C_{60} electron acceptor layer, resulting in power conversion efficiencies up to 0.8%. The absorption edge of the PT at ~620 nm closely matches the edge present in the external quantum efficiency spectra, indicating that the oCVD PT contributes to the photocurrent of the devices. This demonstrates that the oCVD technique can be used in the processing and design of polymer active layers for polymer solar cells and hybrid small molecular organic solar cells without solubility, temperature, or substrate considerations.

4.2 Introduction

Semiconducting polymers and low molecular weight organic molecules have received significant attention for their application as active layers in organic solar cells, due to their potential low cost, high mechanical flexibility, wide array of functionalities, and well-understood structure-composition-property relationships.[1-4] In fact, both solution-printed polymer solar cells and vacuum-deposited small molecule organic solar cells have independently reached record certified efficiencies of 8.3%,[5] through careful materials selection and device architecture engineering.

Vapor-deposited polymer solar cells would enhance the ability to integrate attractive materials into organic solar cells. For example, unsubstituted polymers, which are reported to be more stable because their highly compact structures prevent oxygen permeation into the polymer bulk,[6, 7] are also insoluble and infusible because of their compact structures. Furthermore, the vacuum fabrication of multilayered devices is not constrained by the requirement of finding solvents that will not dissolve the underlying layers to prevent mixing between layers during deposition. However, the high temperatures necessary to physically deposit polymers by vacuum thermal evaporation leads to polymer degradation,[8] limiting materials to low-molecular-weight organics. The few reports in the literature of the use of a vapor deposition technique (such as physical deposition,[9] plasma polymerization,[10] and thermal chemical vapor deposition[11]) to deposit a polymer photoactive layer resulted in low corresponding device efficiencies (<0.3%). Thus a soluble derivative (e.g. poly(3-hexylthiophene)) or an oligomeric version are typically used to facilitate processing by standard solution printing or vacuum thermal evaporation. This leaves a largely unexplored domain of materials for use in organic solar cells (Figure 4-1). This work demonstrates an alternative vacuum fabrication method for the utilization of this region of polymers that is independent of solubility properties.

Oxidative chemical vapor deposition (oCVD) offers a facile route to processing conjugated polymers (including insoluble polymers) via vacuum deposition, offering a potential link between many of the above considerations. In oCVD, conjugated polymers are simultaneously synthesized from vapor phase precursors (monomer and oxidant) and deposited on the substrate at low temperature (25-100 °C) and moderate vacuum (~0.1 Torr).[12, 13]
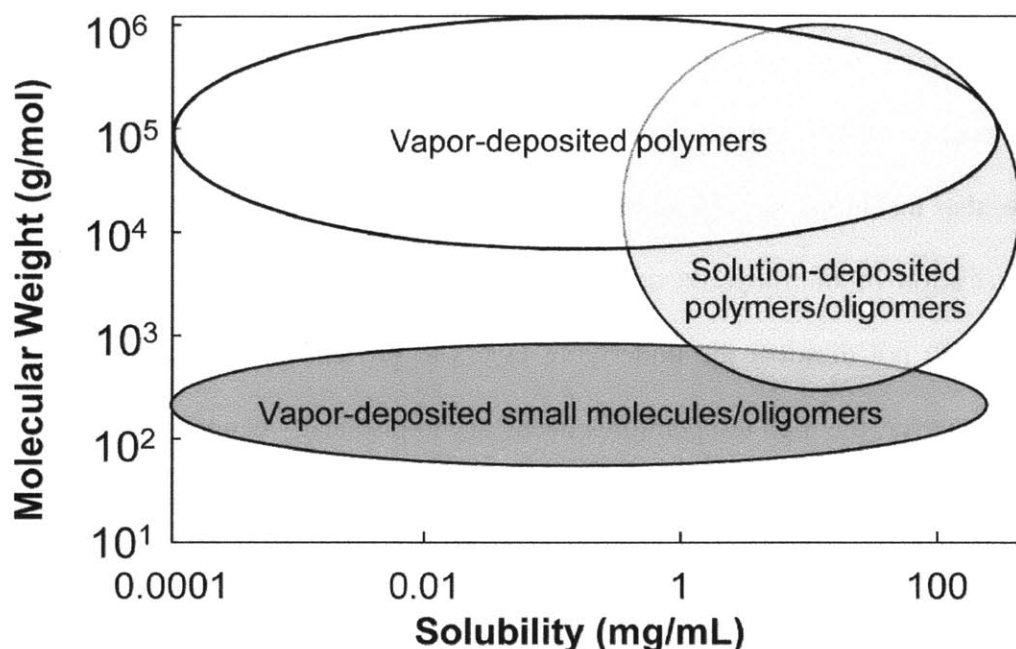
Figure 4-1. Properties of materials deposited by various techniques for use in organic solar cells. Traditionally, the use of polymer is limited to those that can be dissolved so that it can be deposited by some solution-based technique. Vapor deposition is usually limited to molecules with low enough molecular weight to be thermally evaporated. This leaves a region of vapor-deposited polymers that is difficult to access by traditional methods.

Thus, oCVD offers the well-cited processing benefits of vacuum processing, including parallel and sequential deposition, well-defined thickness control and uniformity, and inline integration with other standard vacuum processes (e.g. vacuum thermal evaporation). Moreover, oCVD is conformal over nonplanar substrates, enabling compatibility with substrates such as paper and textiles.[13] In contrast, vacuum thermal evaporation is generally subject to line-of-sight deposition, while conformal deposition of liquid-phase systems is complicated by surface tension effects around micro- and nano-scale features.[14] oCVD has previously been used to conformally deposit thin films of doped conducting polymers, such as poly(3,4-ethylenedioxythiophene) (PEDOT),[12] which have recently been incorporated as transparent electrodes in small molecule organic solar cells on a variety of substrates, including unmodified paper.[13]

Unsubstituted polythiophene (PT) has been prepared by several techniques in the literature, including electropolymerization,[15, 16] chemical polymerization,[17, 18] thermo-cleavage of solubilizing side chains,[7, 19] and various types of vapor deposition techniques such as plasma polymerization[20, 21] and others [22-25]. However, largely because of difficulties in processing PT due to its insolubility or harsh deposition conditions, PT has only been reported in polymer solar cells via electropolymerization[26, 27] and thermo-cleavage of a solution-processable alkylated polymer precursor.[7, 28-30]

Here we report the preparation, characterization, and application of unsubstituted PT by oCVD for use as a photoactive semiconductor in organic solar cells. We characterize as-deposited and methanol-rinsed oCVD PT films to confirm polymer dedoping upon post-processing with methanol. The resulting semiconducting PT is then applied as an electron donor in bilayer heterojunction solar cells with a thermally evaporated C_{60} electron acceptor layer, resulting in power conversion efficiencies up to 0.8%. This demonstrates that the oCVD technique can be used in the processing and design of polymer active layers for polymer solar cells and hybrid small molecule organic solar cells without solubility, temperature, or substrate considerations.

4.3 Experimental

4.3.1 Polythiophene Depositions

The polymer deposition procedure using the oCVD process and the custom-built reactor configuration are described in detail elsewhere.[31, 32] Briefly, the oCVD reactor consists of a vacuum chamber with monomer inlet ports and an exhaust to a pump. A heated crucible holding the oxidizing agent is in the bottom of the chamber, and directly above it is an inverted stage for the substrate. The stage and reactor body were maintained at 30°C and 45°C, respectively. The chamber pressure was held constant at 150 mTorr using a butterfly valve. Iron(III) chloride (FeCl₃,

97%, Sigma-Aldrich) and thiophene (≥99%, Sigma-Aldrich) were used as purchased. Quartz slides, silicon wafers, and ITO-coated glass were used as substrates. $FeCl_3$ was used as the oxidizing agent and it was sublimed at 340°C. Polymer film thickness was controlled by varying the amount of $FeCl_3$ loaded in the crucible. Vapor phase thiophene monomer was introduced into the reactor from a side port on the reactor. The thiophene monomer jar was maintained at a temperature of 25°C and a needle valve was used to limit the flow rate to about 1 sccm. A deposition time of 20 minutes was used for all films. After deposition, the films were rinsed in methanol (≥99.9%, Sigma-Aldrich) for 2 minutes to remove reacted oxidant.

4.3.2 Polymer Characterization

UV-vis spectra of the studied films on quartz substrates were measured with a Varian Cary 5000 UV-vis spectrophotometer. Transmission and reflection spectra were measured. The reflection spectra were obtained using a specular reflectance accessory and an Al standard reference mirror (ThorLabs). Fourier transform infrared (FTIR) measurements of PT films on silicon wafers were performed on a Nexus 870, Thermo Electron Corp. spectrometer. Film compositions were estimated by XPS using a Surface Science Instruments (SSI) model SSX-100 with operating pressure $<2x10^{-9}$ Torr utilizing monochromatic AlKα X-rays at 1486.6 eV. Photoelectrons were collected at an angle of 55-degrees from the surface normal. Film thicknesses were measured using a Veeco Dektak 150 surface profilometer. PT film thicknesses used for devices were approximated by measuring the thickness of PT on glass slides placed close to the ITO substrates from the same deposition. The sheet resistance of the as-deposited PT films were measured with a Jandel four-point probe in air. Conductivity values were calculated using the measured sheet resistivity and thickness measured with the profilometer. Cyclic voltammetry measurements were conducted using a 660D potentiostat (CH Insturments) with a standard three-

electrode configuration under a nitrogen atmosphere. The oCVD PT film on ITO/glass was the working electrode, Ag/AgNO$_3$ (0.01 M in acetonitrile) was the reference electrode, and a platinum mesh attached to a platinum wire was used as the counter electrode. The measurements were performed in acetonitrile with tetrabutylammonium hexafluorophosphate (0.1 M) as the supporting electrolyte at a scan rate of 100 mV s^{-1}. The Fc/Fc+ redox couple was used to calibrate the Ag/Ag+ reference electrode.

4.3.3 Device Fabrication and Characterization

The OPVs were fabricated on glass substrates that were precoated with a 150 nm thick, patterned indium-tin oxide (ITO) transparent anode with 15 Ω/sq sheet resistance (Kintec Co.). Prior to use, the substrates were successively cleaned by ultrasonic treatment in detergent solution (Micro 90), 2 x de-ionized water, 2 x acetone and 2 x isopropanol for 5 minutes each. The substrates were then treated with O$_2$ plasma for 30 seconds. A PT film of varying thickness was deposited onto the cleaned ITO via oCVD as described above. Samples were exposed to air for approximately 10 minutes in transferring them to a glovebox. C$_{60}$ (99.9%, sublimed, Sigma-Aldrich) was purified once by vacuum train sublimation prior to loading, while bathocuproine (BCP, from Luminescence Technology Corp.) and Ag (Alfa Aesar, 1-3 mm shot, 99.9999%) were used as purchased. C$_{60}$, BCP (8 nm), and a 100 nm thick Ag cathode were sequentially deposited via thermal evaporation at a rate of 0.1 nm/s. The cathode films were deposited through a shadow mask for single devices, defining a 1 mm x 1.2 mm active device area, and there were 10 devices per substrate. The current-density-voltage (J-V) measurements were recorded by a Keithley 6487 picoammeter and 100 ± 10 mW cm^{-2} illumination was provided by a nitrogen-glovebox-integrated 1kW xenon arc-lamp (Newport 91191) equipped with an AM1.5G filter. The solar simulator intensity was measured with a calibrated silicon photodiode. The external quantum efficiency

(EQE) spectra were measured with a Stanford Research Systems SR830 lock-in amplifier, under a focused monochromatic beam of variable wavelength light generated by an Oriel 1kW xenon arc lamp coupled to an Acton 300i monochromator and chopped at 43 Hz. A Newport 818-UV calibrated silicon photodiode was used to measure the incident monochromatic light intensity.

4.4 Results and Discussion

4.4.1 PT Synthesis

Following a procedure similar to that for the deposition of poly(3,4-ethylenedioxythiophene) (PEDOT) by oCVD, thiophene monomer vapor was fed into a reaction chamber.[31] Thiophene reacted via oxidative polymerization with sublimated iron(III) chloride on a substrate to result in the deposition of a solid, polymer film [Figure 4-2 (1)]. The generally accepted mechanism for the oxidative polymerization of thiophene involves the formation of radical cations.[1] Further oxidation results in the formation of polarons and bipolarons, making the polymer conductive.[33] The cations are charge balanced by counter anions [Figure 4-2 (2)]. The resulting polymer film from the oCVD process is a conductive, blue film (Figure 4-3). This suggests that $FeCl_3$ is present in large enough concentrations during the oCVD process to over-oxidize the PT, as has been seen during chemical polymerization in solution. Based on conductivity measurements in air, the doped PT film conductivities ranged from 10 to 20 S cm^{-1}.
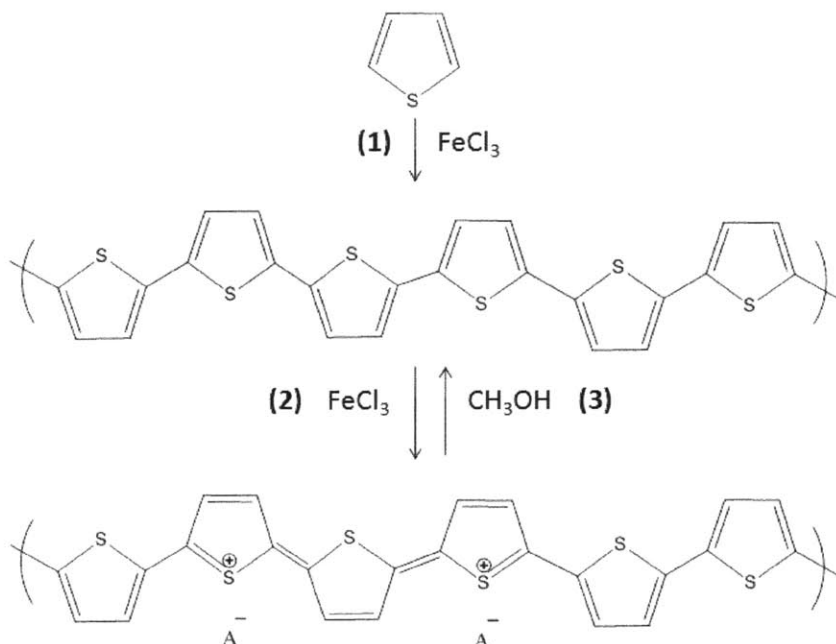
Figure 4-2. Processes (1) and (2) occur during the oCVD deposition process, while process (3) is a post-deposition step. (1) Oxidative polymerization of thiophene to polythiophene. (2) Oxidation of the polymer chain leads to the formation of polarons and bipolarons (shown), which are charge balanced by counteranion dopants. (3) Rinsing the deposited film with methanol reduces it back to neutral PT.

A post-deposition rinse treatment of the films with methanol caused them to become nonconductive and undergo an abrupt color change to red (Figure 4-3). The conductivities of the methanol-rinsed films were below the detection limit of the equipment used ($<10^{-4}$ S cm^{-1}). The observed changes in conductivity and color of the films suggest that the methanol rinse dedoped the PT [Figure 4-2 (3)]. Composition measurements from X-ray photoelectron spectroscopy (XPS) survey scans show that the methanol rinse significantly reduces the amount of iron and chlorine in the PT film (Table 4-1). It is possible that the dedoping mechanism follows a similar mechanism as that for other reactions involving the oxidation of primary alcohols with strong electrophiles.[34] Additionally, the high solubility of iron in methanol results in rapid removal of most of the reacted oxidant.
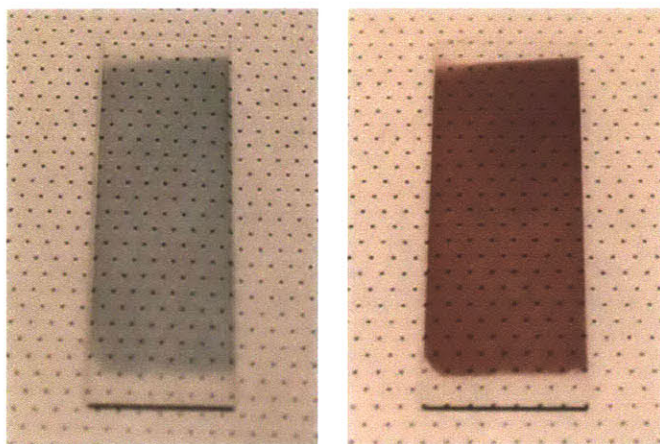
Figure 4-3. As-deposited oCVD PT film (left) and methanol-rinsed film (right) uniformly deposited on 25 x 75 mm glass slides. The blue PT film is doped with $FeCl_3$ and has a conductivity between 10 and 20 S cm^{-1}, whereas the red film is neutral PT and nonconductive.

Table 4-1. Atomic ratios in PT films from XPS survey scans after various methanol rinsing times.

Rinsing time (min)	C : S	Fe : S	Cl : S
0	16	1.6	2.8
2	6.1	0.05	0.07
60	5.8	0.05	0.07
240	5.7	0.05	0.07

4.4.2 UV-vis and Fourier Transform Infrared (FTIR) Spectroscopy

The UV-vis absorption spectra of the as-deposited and methanol-rinsed PT films are shown in Figure 4-4. The presence of midgap energy states in the as-deposited PT film is indicative of the presence of polarons or bipolarons.[35] The energy levels of the peaks (0.8 and 1.6 eV) suggest that the conductive PT film is heavily doped and contains bipolarons.[35, 36] The maximum of the absorption coefficient of the methanol-rinsed PT occurs at 495 nm (~2.5 eV). The optical band gap, taken as the intersection of the line tangent to the band edge with the x-axis, is 1.96 eV. These values match those of electrochemically and chemically polymerized neutral PT.[36, 37] This further supports the hypothesis that the methanol rinse reduces the PT film.
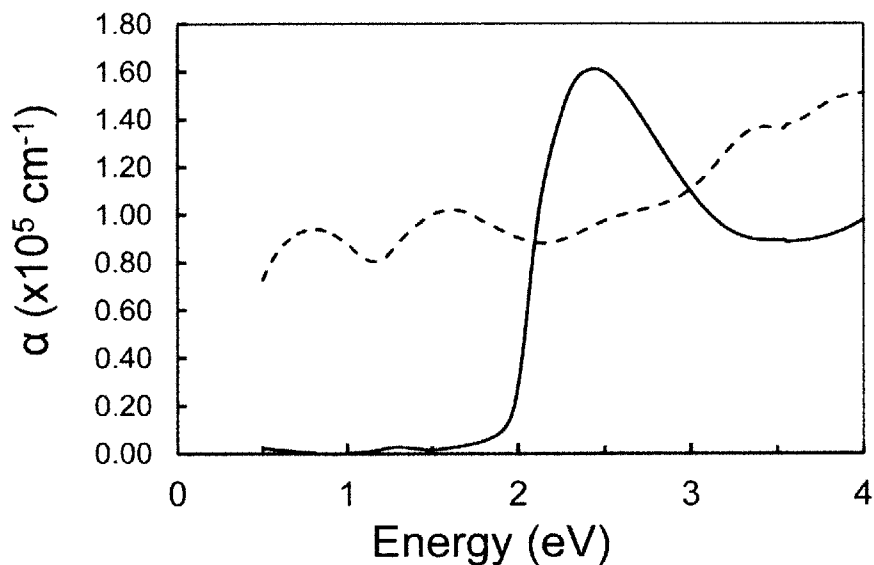
Figure 4-4. Absorption coefficient of doped (- -) and dedoped (—) oCVD PT films on quartz. The energy levels of midgap peaks in the doped film suggest that it is heavily doped, resulting in bipolarons in the film.

The FTIR spectra of the as-deposited and methanol-rinsed films are shown in Figure 4-5, along with a reference spectra for neutral polythiophene.[38] The MeOH-rinsed spectrum matches the neutral reference spectrum closely, suggesting that neutral (dedoped) PT is indeed formed.
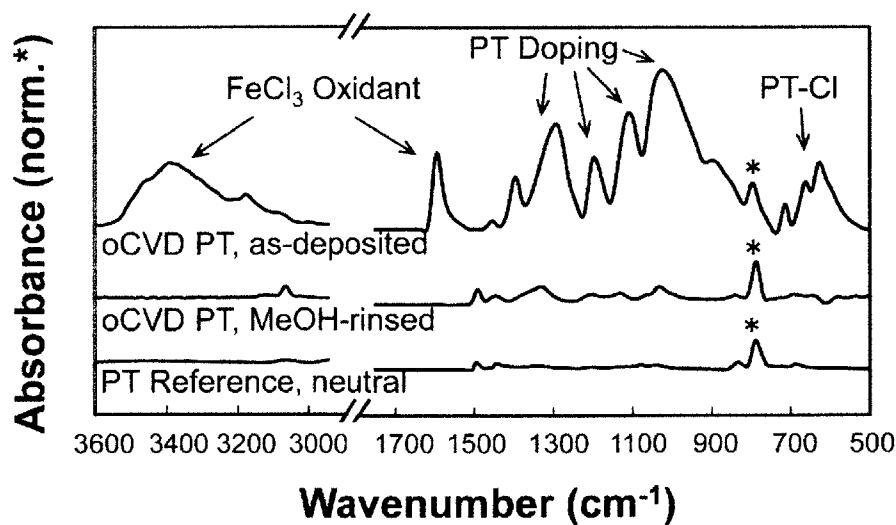
Figure 4-5. FTIR spectra of oCVD PT film before and after MeOH rinse. The bottom spectrum is a reference spectrum for neutral PT.[38] All spectra are normalized by the C-H vibrational peak at 790 cm^{-1}, as indicated by the asterisk.

All spectra show peaks at around 790 cm^{-1}, attributed to C-H out-of-plane vibration for 2,5-substituted thiophene, along with peaks at 1450 and 1490 cm^{-1} due to 2,5-substituted thiophene ring stretching, and a C-H stretching peak at 3060 cm^{-1}.[39, 40] To elucidate the relative strength of doping-induced absorption peaks in the as-deposited PT sample, all spectra were normalized by the C-H vibrational peak at 790 cm^{-1}, as its intensity has previously been reported to be independent of doping effects.[39] The as-deposited PT film shows strong peaks throughout the spectral range that are not present in the spectra for the neutral reference or MeOH-treated oCVD PT film. It has previously been reported for oCVD PEDOT films that the presence of broad and strong absorption peaks in the 1400-700 cm^{-1} range films are indicative of doping of the conjugated polymer chain,[31] as are evident in the as-deposited PT film. The peaks indicated with arrows at 1320, 1200, 1190, and 1020 cm^{-1} match closely with the doping-induced peaks observed in electrochemically prepared PT, independent of the dopant species.[39] The broad peak below 700 cm^{-1} is ascribed to Cl-specific dopant interactions with the thiophene ring, as observed for plasma-polymerized thiophene doped with Cl.[41] Finally, the sharp peak at 1600 cm^{-1} and the characteristic -OH peak at 3500-3300 cm^{-1} are indicative of atmospheric water interactions with residual iron chloride oxidant in the PT film, which is known to be strongly hydroscopic. Both of these peaks have been observed in $FeCl_3$-doped poly(phenylacetylene),[42] and are also strongly evident in the $FeCl_3$ and $FeCl_2$ spectra themselves.[43] These doping- and oxidant-related peaks are removed for the MeOH-rinsed film, which agrees with the neutral PT reference spectrum, supporting the claim that methanol post-treatment removes the oxidant residue and dedopes the as-deposited oCVD PT film.

4.4.3 Electrochemical Properties

Cyclic voltammetry was used to study the electrochemical properties of oCVD PT. PT films were deposited onto ITO-coated glass and rinsed in methanol to use as the working electrode. Ferrocene/ferrocenium (Fc/Fc$^+$) was used as an external standard. The half-wave potential (E$_{1/2}$) of the Fc/Fc$^+$ couple was measured under the same testing conditions to be 0.096 V to the Ag/Ag$^+$ electrode. The cyclic voltammogram of the PT film is shown in Figure 4-6. The pre-peaks that appear before the peaks for both the n-doping and p-doping processes are due to charge trapping.[44, 45] This phenomenon is often seen during consecutive p- and n-doping cycles of conducting polymers.[46, 47]
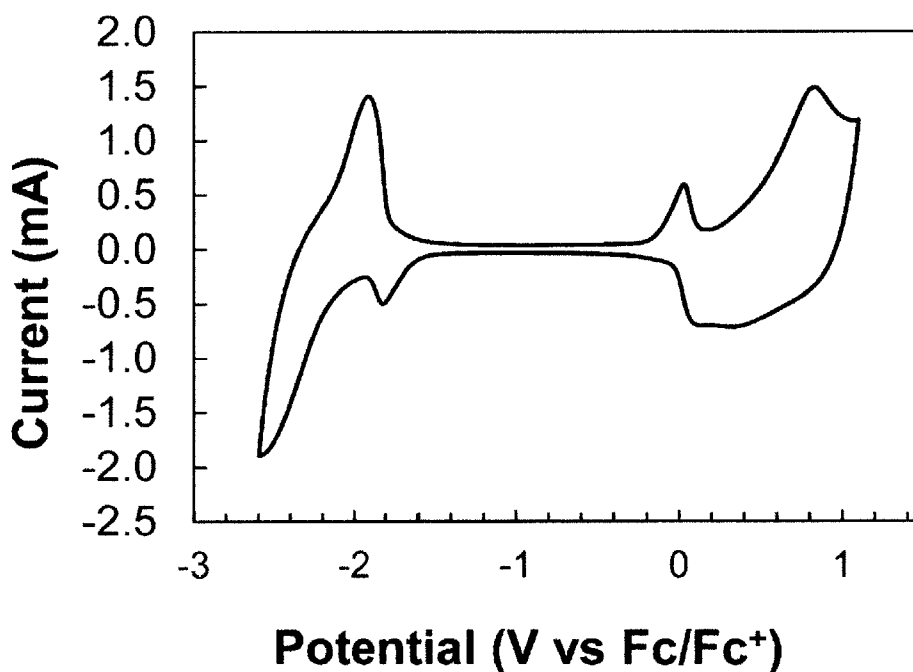
Figure 4-6. Cyclic voltammogram of the oCVD PT film deposited onto ITO-coated glass in an acetonitrile solution of Bu$_4$NPF$_6$ (0.1 M) at a scan rate of 100 mV s^{-1}. The Ag/Ag$^+$ reference electrode was calibrated using the Fc/Fc$^+$ redox couple.

The onset of the oxidation and reduction peaks were estimated as being 0.36 V and -2.09 V vs Fc/Fc$^+$, respectively. The energy levels of the highest occupied molecular orbital (HOMO)

and lowest unoccupied molecular orbital (LUMO) were calculated according to the following equations:

$$E_{HOMO} = -\left(E_{[onset,ox \; vsFc/Fc+]} + 4.76\right)(eV) \qquad (1)$$

$$E_{LUMO} = -\left(E_{[onset,red \; vsFc/Fc+]} + 4.76\right)(eV) \qquad (2)$$

These equations assume that the redox potential of Fc/Fc^+ has an absolute energy level of -4.76 eV relative to vacuum,[48] although several other values have been used in the literature.[49] The calculated HOMO and LUMO levels are -5.12 eV and -2.67 eV, respectively. The electrochemical band gap is 2.45 eV.

4.4.4 Photovoltaic Device Performance

Dedoped PT was then prepared on patterned ITO-coated glass substrates for incorporation as the electron donor layer in bilayer heterojunction photovoltaic cells. The PV devices were completed by vacuum thermal evaporation of fullerene C_{60} as the electron acceptor, bathocuproine (BCP) as an exciton blocking layer, and silver (Ag) as the cathode. BCP is commonly used in small molecule organic photovoltaics.[50] The resulting device structures were: ITO/PT/C_{60}/BCP (8 nm)/Ag (100 nm).

First, the thickness of the C_{60} layer was optimized by varying its value and using a PT layer thickness of ~30 nm. Representative current-density-voltage (J-V) curves obtained under one sun of air mass 1.5G (AM 1.5G) irradiation (100 mW cm^{-2}) are shown in Figure 4-7 (a). The fill factor (FF) remained relatively constant with variation in C_{60} thickness, whereas the open circuit voltage (V_{oc}), short-circuit current (J_{sc}), and power conversion efficiency (PCE) achieve a maximum at around 30 nm of C_{60} [Figure 4-7 (b)].
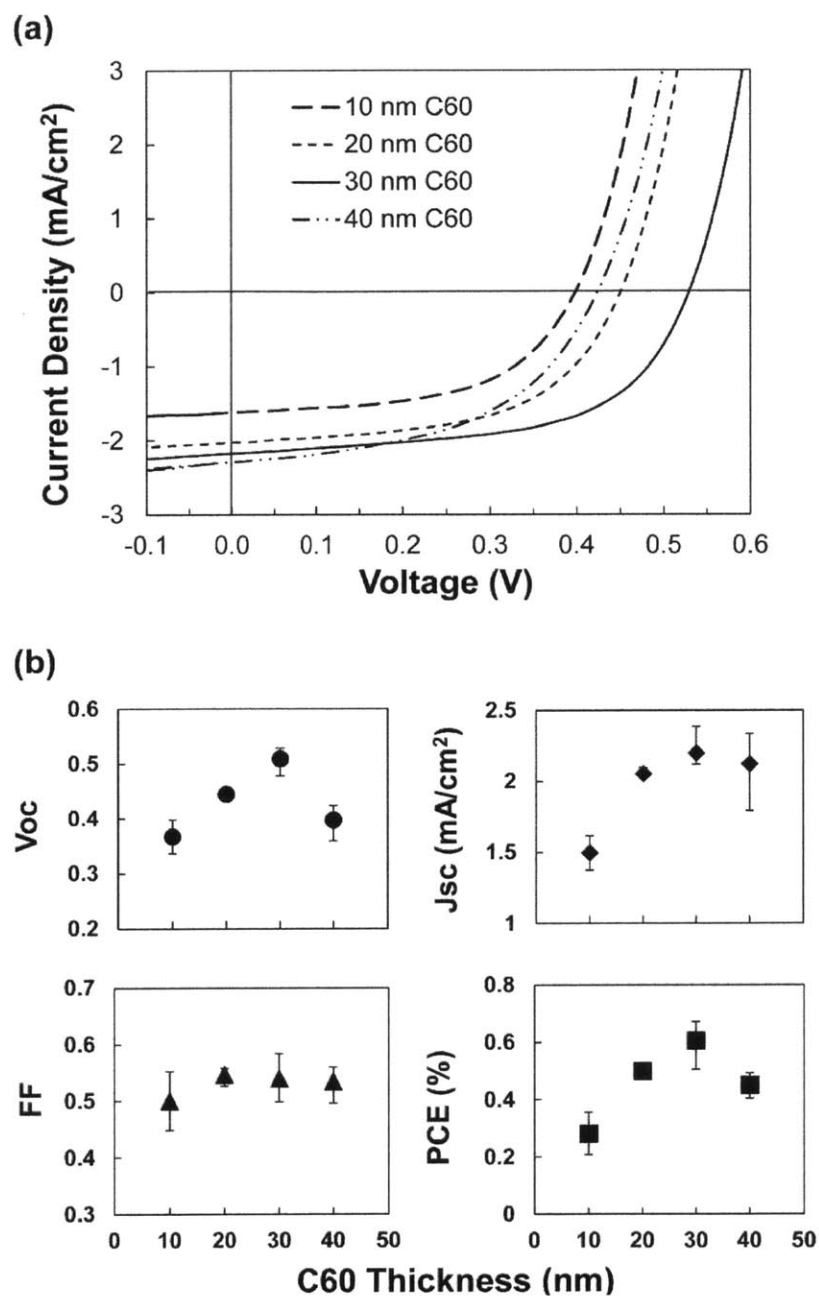
Figure 4-7. (a) J-V characteristics of devices with structure ITO/PT (~30nm)/C_{60}/BCP (8 nm)/Ag under 100 mW cm^{-2} AM1.5G simulated solar illumination. **(b)** Performance characteristics of the above devices. Markers and error bars correspond to the average and maximum and minimum values obtained. An efficiency maximum is achieved for a 30 nm-thick C_{60} layer.

The change in short-circuit current with increasing C_{60} thickness is expected due to the changes in optical interference patterns within the thin multilayer device stack, as the position of

the reflective Ag interface is moved farther from the PT/C_{60} interface.[50] The optical electric field is expected to be maximized for shorter wavelengths (e.g. C_{60} absorption peak) closer to the reflective node and for longer wavelengths (e.g. PT absorption peak) farther from the reflective node, which should vary the relative amount of photocurrent originating from excitons generated in the C_{60} and PT layers, respectively. This effect is evident in Figure 4-8, which shows the variation in the external quantum efficiency (EQE) as the thickness of the C_{60} is changed.
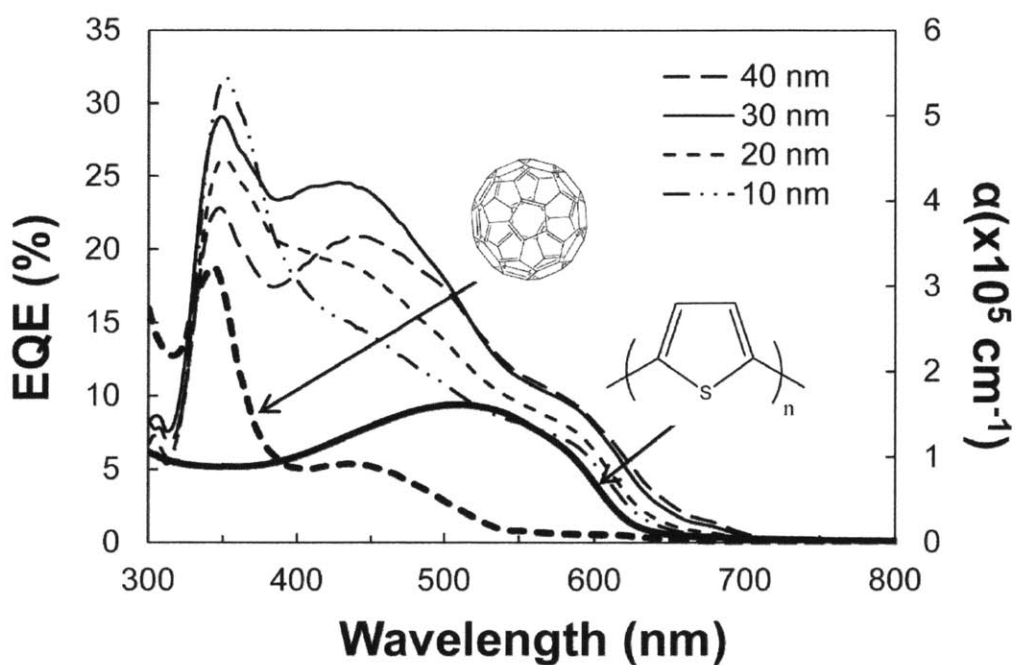
Figure 4-8. The thin lines show the EQE spectra (left axis) of the devices in Figure 4-7 in which the C_{60} thickness is varied. The bold lines show the absorption coefficients of C_{60} (- -) and oCVD PT (—) (right axis). The absorption edge past 600 nm in the EQE suggests that the oCVD PT is functioning as a photoactive layer.

The bold lines show the absorption coefficients of C_{60} and oCVD PT. Any EQE past about 550 nm should be mainly due to excitons generated in the PT layer and EQE below 400 nm primarily due to C_{60} excitons. As the C_{60} becomes thicker, the shoulder in the EQE curve around 600 nm becomes larger, likely due to additional excitons generated in the PT as the optical field maxima for longer wavelengths are positioned within an exciton diffusion length of the

heterojunction interface. In contrast, the EQE at short wavelengths near the C_{60} absorption peaks decrease as the C_{60} thickness is increased. This is likely due to loss of excitons that are generated too far from the heterojunction interface to diffuse and separate before recombining, as the optical field maxima for the shorter wavelengths are positioned deeper into the C_{60} layer. These observations suggest that both PT and C_{60} are contributing to the device photocurrent, which is balanced at around 30 nm of C_{60}. Lastly, the J_{sc} values calculated by integrating the product of the EQE and the AM1.5G solar spectrum are 1.7, 2.0, 2.5, and 2.4 mA/cm^2 for 10, 20, 30, and 40 nm of C_{60}, respectively. These values are in close agreement with the J_{sc} values shown in Figure 4-7.

Devices were then fabricated with a fixed C_{60} thickness of 30 nm and a varying PT thickness. Representative J-V curves for these devices under AM 1.5G (100 mW cm^{-2}) are shown in Figure 4-9 (a). The J_{sc} for the devices remained constant, but the FF decreased with increasing PT thickness [Figure 4-9 (b)]. The decrease in fill factor is most likely explained by an increase in series resistance through the device with thicker PT layers, which was generally observed to manifest as a lower slope in the J-V curves at positive bias above V_{oc}. Additionally, for devices with a PT layer thicker than about 35 nm, there is much more variability in the values of V_{oc}. A maximum PCE of 0.8% was achieved using about 25 nm of PT and 30 nm of C_{60}. This is the highest efficiency achieved to date for the use of a vapor-phase deposition of the donor polymer for a polymer solar cell. Furthermore, despite using a bilayer structure, this efficiency is also comparable to bulk heterojunction devices made with PT and similar acceptor materials (Table 4-2). Higher efficiencies should be possible using bulk heterojunction device structures instead of bilayer structures and with the use of different acceptor materials.
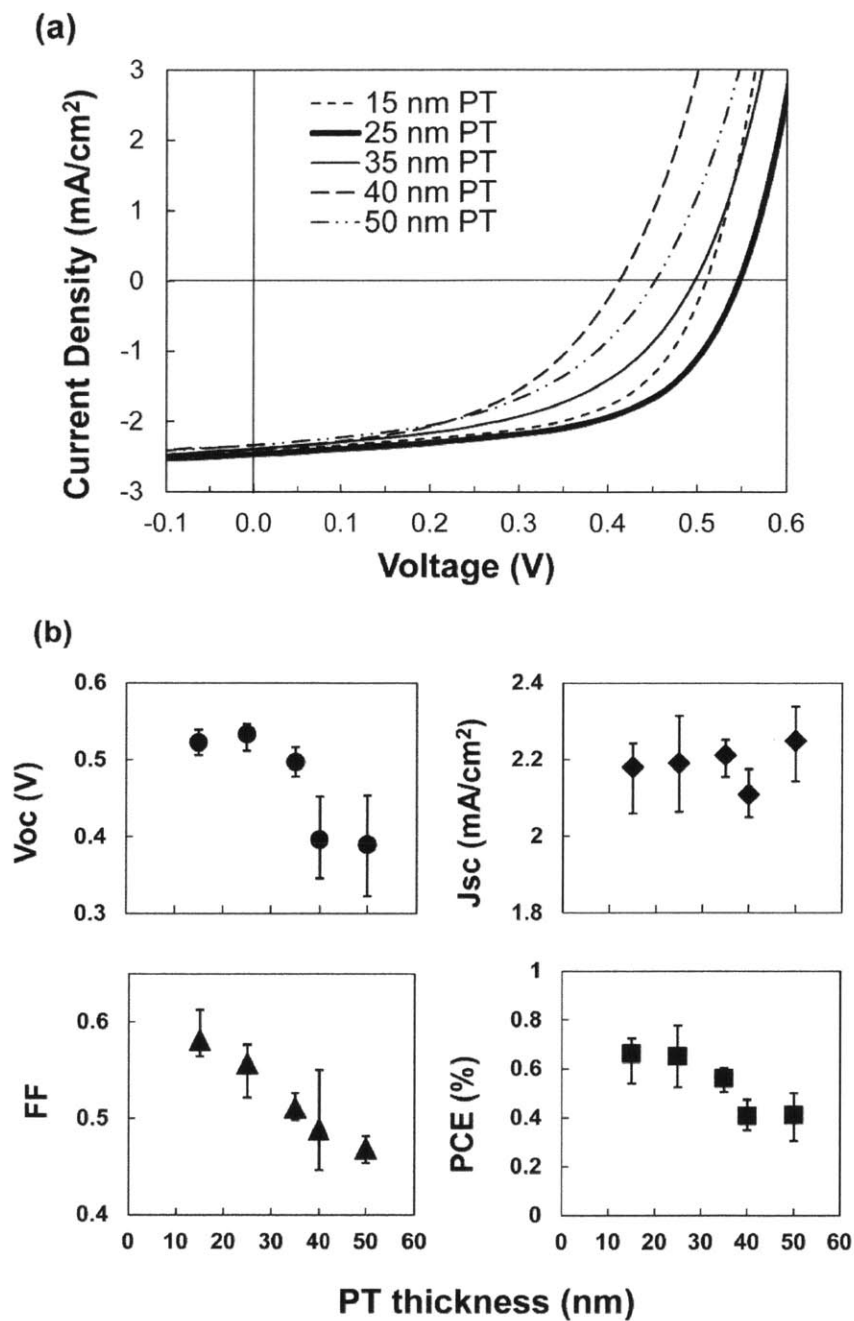
Figure 4-9. (a) J-V characteristics of devices with structure with structure ITO/PT/C_{60} (30 nm)/BCP (8 nm)/Ag. **(b)** Performance characteristics of the above devices. Markers and error bars correspond to the average and maximum and minimum values obtained. A maximum efficiency of 0.8% was obtained for a 25 nm PT layer with 30 nm of C_{60}.

Table 4- 2. Summary of device structures and performance that use PT as the donor material. The devices using oCVD PT provide comparable or better performance compared to other PT deposition methods.

Deposition Method	Device Structure	Acceptor	PCE (%)	Source
oCVD	Bilayer	C_{60}	0.8	This work
Solution processing/ thermocleavage	Bulk heterojunction	(60)PCBM	0.6, 0.84	[7], [28]
Solution processing/ thermocleavage	Bulk heterojunction	(70)PCBM	1.5	[7]
Electropolymerization	Bilayer	(60)PCBM	0.1	[27]
Electropolymerization	Single layer (Schottky device)	-	0.02	[26]

4.5 Conclusions

In conclusion, we have used oCVD to obtain unsubstituted polythiophene. A doped, conductive form of the polymer is deposited during the oCVD process. Rinsing the film with methanol is sufficient to dedope the PT to obtain the semiconducting form, as confirmed by UV-vis, FTIR, and XPS. By directly depositing onto ITO substrates, the neutral PT was successfully incorporated into efficient bilayer heterojunction photovoltaic devices with C_{60}. The external quantum efficiency spectra demonstrate that the oCVD PT contributes to the photocurrent generation of the devices, which is successfully balanced with photocurrent from C_{60} through variation in the layer thicknesses.

It is expected that device fabrication using oCVD active layers will be directly compatible with other substrates, including those that are rough, lack the ability to withstand high temperature, and/or degrade upon exposure to solvents. This technique can easily be extended to the deposition of other semiconducting polymers by changing the monomer used. By utilizing oCVD, the selection of the monomer is no longer constrained by the requirement that the resulting conjugated polymer must be soluble or stable at high temperatures for thermal evaporation. Thus, this opens up a range of materials with potentially desirable properties that can be considered for an active layer material with the goals of improving device efficiency and stability. Additionally, with the

use of different monomers to deposit polymers with different bandgaps, oCVD can provide another route for the fabrication of tandem polymer solar cells capable of energy conversion across the solar spectrum. Thus, oCVD is a viable technique that can combine the benefits of vacuum processing and the use of semiconducting polymers for fabricating organic photovoltaics.

4.6 Acknowledgements

4.7 References

1.   R. D. McCullough, *Adv. Mater.*, 1998, 10, 93-116.
2.   C. J. Brabec, S. Gowrisanker, J. J. M. Halls, D. Laird, S. J. Jia and S. P. Williams, *Adv. Mater.*, 2010, 22, 3839-3856.
3.   E. Bundgaard and F. C. Krebs, *Sol. Energy Mater. Sol. Cells*, 2007, 91, 954-985.
4.   S. R. Forrest, *Nature*, 2004, 428, 911-918.
5.   8.3% efficient vacuum-deposited molecular OPV (Heliatek/IAPP, 2010), http://www.heliatek.com/?p=199&lang=en, Last accessed November 30, 2011. 8.3% efficient solution-deposited polymer OPV (Konarka, 2010), 2010, http://www.konarka.com/index.php/site/pressreleasedetail/konarkaspowerplasti c_achievesworldrecord_83_efficiencycertification_fr, Last accessed November 30, 2011.
6.   F. C. Krebs and H. Spanggaard, *Chem. Mater.*, 2005, 17, 5235-5237.
7.   S. A. Gevorgyan and F. C. Krebs, *Chem. Mater.*, 2008, 20, 4386-4390.
8.   K. P. Gritsenko and A. M. Krasovsky, *Chem. Rev.*, 2003, 103, 3607-3649.
9.   P. Kovacik, G. Sforazzini, A. G. Cook, S. M. Willis, P. S. Grant, H. E. Assender and A. A. R. Watt, *ACS Appl. Mater. Interfaces*, 2011, 3, 11-15.
10.   A. H. Bhuiyan and S. V. Bhoraskar, *Thin Solid Films*, 1988, 162, 333-342.
11.   C. Y. Lee and M. H. C. Jin, in *Organic Photovoltaics Viii*, eds. Z. H. Kafafi and P. A. Lane, 2007, vol. 6656, pp. Y6560-Y6560.

12. S. G. Im, D. Kusters, W. Choi, S. H. Baxamusa, M. de Sanden and K. K. Gleason, *ACS Nano*, 2008, 2, 1959-1967.

13. M. C. Barr, J. A. Rowehl, R. R. Lunt, J. Xu, A. Wang, C. M. Boyce, S. G. Im, V. Bulović and K. K. Gleason, *Adv. Mater.*, 2011, 23, 3500-3505.

14. S. H. Baxamusa, S. G. Im and K. K. Gleason, *Phys. Chem. Chem. Phys.*, 2009, 11, 5227-5240.

15. B. Krische and M. Zagorska, *Synth. Met.*, 1989, 28, C263-C268.

16. M. Gratzl, D. F. Hsu, A. M. Riley and J. Janata, *J. Phys. Chem.*, 1990, 94, 5973-5981.

17. J. Tang, L. Kong, J. Zhang, L. Zhan, H. Zhan, Y. H. Zhou and C. Zhan, *React. Funct. Polym.*, 2008, 68, 1408-1413.

18. X. G. Li, J. Li, Q. K. Meng and M. R. Huang, *J. Phys. Chem. B*, 2009, 113, 9718-9727.

19. M. Manceau, M. Helgesen and F. C. Krebs, *Polym. Degrad. Stab.*, 2010, 95, 2666-2669.

20. R. Dams, D. Vangeneagden and D. Vanderzande, *Chem. Vap. Deposition*, 2006, 12, 719-727.

21. H. Goktas, F. G. Ince, A. Iscan, I. Yildiz, M. Kurt and I. Kaya, *Synth. Met.*, 2009, 159, 2001-2008.

22. T. Sorita, H. Fujioka, M. Inoue and H. Nakajima, *Thin Solid Films*, 1989, 177, 295-303.

23. S. Tepavcevic, Y. Choi and L. Hanley, *J. Am. Chem. Soc.*, 2003, 125, 2396-2397.

24. P. M. Bayley, B. Winther-Jensen, D. R. MacFarlane, N. M. Rocher and M. Forsyth, *React. Funct. Polym.*, 2008, 68, 1119-1126.

25. B. Winther-Jensen, J. Chen, K. West and G. Wallace, *Macromolecules*, 2004, 37, 5930-5935.

26. R. Valaski, C. D. Canestraro, L. Micaroni, R. M. Q. Mello and L. S. Roman, *Sol. Energy Mater. Sol. Cells*, 2007, 91, 684-688.

27. W. L. Yu, B. Xu, Q. F. Dong, Y. H. Zhou, J. H. Zhang, W. J. Tian and B. Yang, *J. Solid State Electrochem.*, 2010, 14, 1051-1056.

28. T. Tromholt, S. A. Gevorgyan, M. Jorgensen, F. C. Krebs and K. O. Sylvester-Hvid, *ACS Appl. Mater. Interfaces*, 2009, 1, 2768-2777.

29. M. H. Petersen, S. A. Gevorgyan and F. C. Krebs, *Macromolecules*, 2008, 41, 8986-8994.

30. F. C. Krebs and K. Norrman, *ACS Appl. Mater. Interfaces*, 2010, 2, 877-887.

31. J. P. Lock, S. G. Im and K. K. Gleason, *Macromolecules*, 2006, 39, 5326-5329.

32. S. G. Im and K. K. Gleason, *Macromolecules*, 2007, 40, 6552-6556.

33. R. D. McCullough and P. C. Ewbank, in *Handbook of Conducting Polymers* eds. T. A. Skotheim, R. L. Elsenbaumer and J. R. Reynolds, Marcel Dekker, Inc., New York, 2 edn., 1998, ch. 9, p. 226.

34. J. G. Smith, Organic Chemistry McGraw Hill, Boston, 2 edn., 2007.

35. K. Kaneto, Y. Kohno and K. Yoshino, *Solid State Commun.*, 1984, 51, 267-269.

36. T. C. Chung, J. H. Kaufman, A. J. Heeger and F. Wudl, *Phys. Rev. B*, 1984, 30, 702-710.

37. M. Kobayashi, J. Chen, T. C. Chung, F. Moraes, A. J. Heeger and F. Wudl, *Synth. Met.*, 1984, 9, 77-86.

38. Spectral data from Wiley Subscription Services, Inc., 2011.

39. S. Hotta, T. Hosaka and W. Shimotsuma, *Synth. Met.*, 1983, 6, 69-71.

40. D. Lin-Vien, N. B. Colthup, W. G. Fateley and J. G. Grasselli, *The Handbook of Infrared and Raman Characteristic Frequencies of Organic Molecules*, Academic Press, 1991.

41. M. Vasquez, G. J. Cruz, M. G. Olayo, T. Timoshina, J. Morales and R. Olayo, *Polymer*, 2006, 47, 7864-7870.

42. M. V. Russo, G. Polzonetti and A. Furlani, *Synth. Met.*, 1991, 39, 291-301.

43. Spectral data from the Bio-Rad/Sadtler IR Data Collection, 2011.

44. G. Zotti, G. Schiavon and S. Zecchin, *Synth. Met.*, 1995, 72, 275-281.

45. R. Borjas and D. A. Buttry, *Chem. Mater.*, 1991, 3, 872-878.

46. J. Heinze, B. A. Frontana-Uribe and S. Ludwigs, *Chem. Rev.*, 2010, 110, 4724-4771.

47. A. R. Hillman, S. J. Daisley and S. Bruckenstein, *Electrochim. Acta*, 2008, 53, 3763-3771.

48. B. W. D'Andrade, S. Datta, S. R. Forrest, P. Djurovich, E. Polikarpov and M. E. Thompson, *Org. Electron.*, 2005, 6, 11-20.

49. C. M. Cardona, W. Li, A. E. Kaifer, D. Stockdale and G. C. Bazan, *Adv. Mater.*, 2011, 23, 2367-2371.

50. P. Peumans, A. Yakimov and S. R. Forrest, *J. Appl. Phys.*, 2003, 93, 3693-3723.

Chapter 5

Vapor-deposited Mixed Heterojunction Polymer Solar Cells

5.1 Abstract

Bulk heterojunctions are the most ubiquitous device architecture for organic photovoltaics (OPVs), as the large donor-acceptor interfacial area allows for increased device current. Previously we have shown that planar heterojunction OPVs can be fabricated using a vapor-deposited polymer via oxidative chemical vapor deposition (oCVD). Here we provide the first demonstration of vapor-deposited mixed heterojunction polymer solar cells. This is accomplished by simultaneously evaporating thiophene monomer, iron(III) chloride oxidizing agent, and C_{60} to result in mixed films of oCVD polythiophene (PT) and C_{60}. Various film compositions are deposited and their absorption and morphological features are investigated. OPVs are then fabricated with these films, which successfully demonstrate a photovoltaic response under illumination.

5.2 Introduction

The most common organic photovoltaic (OPV) device structure for polymer solar cells is the bulk heterojunction (BHJ) in which the donor and acceptor compounds are mixed together. This structure drastically increases the donor-acceptor interfacial area necessary for exciton dissociation.[1-3] For polymer solar cells, this is typically done by finding a solvent in which the donor polymer and acceptor compound are both sufficiently soluble in. Films of the mixtures are then cast using various solution-based techniques, such as spin-coating, doctor-blading, and inkjet printing.[4] The best single junction polymer bulk heterojunction OPVs have achieved efficiencies of ~8 - 9%.[5-8] Many attempts have also been made to deposit mixed heterojunction thermally evaporated small molecule solar cells to improve device efficiency. This is done by co-evaporating the donor and acceptor materials to varying degrees.[9-11] Researchers have experimented with various gradations of the donor and acceptor materials in the active layer, from fully mixed BHJs

to structures called planar mixed heterojunctions (PMHJs) in which a mixed layer is sandwiched in between pure layers of donor on the anode side and acceptor on the cathode side.[12-14] Through material and structural optimization, efficiencies up to ~5-6% have been obtained for mixed single heterojunction small molecule OPV devices.[15-17]

Oxidative chemical vapor deposition (oCVD) enables the deposition of conjugated polymer films from the vapor phase. Polymers are simultaneously synthesized and deposited from vaporized monomer and oxidant precursors on a substrate at low temperature (~25-150 °C) and moderate vacuum (~0.1 Torr) during oCVD.[18] oCVD offers uniform deposition over large areas that is independent of the substrate material.[19] Additionally, oCVD polymers can be conformally deposited on nonplanar substrates such as paper and textiles.[20, 21] Similar to other vacuum deposition processes, it also offers accurate thickness control and potential for integration with other standard vacuum processes such as thermal evaporation. oCVD has previously been used to deposit various conducting and semiconducting polymers, including poly(3,4-ethylenedioxythiophene) (PEDOT), unsubstituted polythiophene, and others.[22-24] Furthermore, we demonstrated that oCVD PT can successfully serve as the electron donor material in planar heterojunction polymer solar cells, resulting in efficiencies up to 0.8%.[23]

Here we provide the first demonstration of vapor-deposited mixed heterojunction polymer solar cells. This is accomplished by simultaneously evaporating thiophene monomer, iron(III) chloride oxidizing agent, and C_{60} to result in mixed films of oCVD PT and C_{60}. Various film compositions are deposited and their corresponding device performances are investigated.

5.3 Experimental

oCVD depositions were carried out in a modified oCVD reactor (see Figure 5-1). The reactor chamber is a stainless steel cube (41 x 41 x 41 cm^3). A dry pump (Edwards, iQDP40 with

103

a QMB250A mechanical booster) was used to achieve vacuum through an exhaust port opposite from the monomer inlet port. The chamber is equipped with four low temperature evaporation (LTE) point sources (Kurt J. Lesker Co.) that are designed for evaporating volatile organic materials (note: only two are shown in Figure 5-1 for clarity). Each point source is off-centered and slightly angled (~30° from vertical) towards the stage, which is approximately 20 cm away. One point source evaporator each was used to heat separate crucibles holding the iron(III) chloride oxidizing agent and C_{60}. The substrate stage is at the top of the reactor chamber and inverted to face down. The stage is capable of rotating, which greatly contributes to improved uniformity of samples over the entire stage surface (21 cm in diameter). Pressures were read with an absolute capacitance manometer (MKS Instruments, 20 Model 628D). The stage and reactor body were unheated for this study. The chamber pressure was held constant at 75 mTorr using a butterfly valve (MKS Instruments, Model 653B).

Thiophene (≥99%, Sigma-Aldrich) and iron(III) chloride ($FeCl_3$, 97%, Sigma-Aldrich) were used as purchased. Films were deposited onto boro-aluminosilicate glass (Corning® 1737) substrates for characterization and ITO-coated glass (Thin Film Devices, 50 Ω/sq) for device fabrication. Thiophene monomer was maintained at 25 °C in a temperature-controlled glass jar outside of the reactor. Vapor phase thiophene monomer was introduced into the reactor using a gas feedthrough that was piped into the chamber and pointed facing directly at the stage approximately 20 cm away (see Figure 5-1). A needle valve was used to limit the flow rate to ~1 sccm. $FeCl_3$ was sublimed at ~195°C. For depositions involving C_{60}, the C_{60} crucible was heated to 470 °C from room temperature at a rate of 30 °C/min. When C_{60} deposition was desired, the source shutter was opened and the nitrogen carrier gas was turned on (20 sccm). Prior to loading, C_{60} (99.9%, sublimed, Sigma-Aldrich) was purified once by vacuum train sublimation prior.[25] The

stage was rotated at ~3 rpm during the depositions. After deposition, the films were rinsed in methanol ($\geq$99.9%, Sigma-Aldrich) for 20 minutes, 0.2M HCl in methanol for 10 minutes, followed by 1 minute in methanol to remove reacted oxidant.

UV-vis absorbance spectra of the studied films on glass substrates were measured with a Varian Cary 5000 UV-vis spectrophotometer. Film thicknesses were measured using a Veeco Dektak 150 surface profilometer. Morphologies of the thin films were measured using an Agilent Technologies AFM in tapping mode with a Bruker Si cantilever having a tip frequency of 330 kHz.

The OPVs were fabricated on glass substrates that were pre-coated with a 75 nm thick, patterned indium-tin oxide (ITO) transparent anode with 50 Ω/sq sheet resistance. Prior to use, the substrates were successively cleaned by ultrasonic treatment in detergent solution (Micro 90), 2 x de-ionized water, 2 x acetone and 2 x isopropanol for 5 minutes each. The substrates were then treated with O_2 plasma for 30 seconds. Films of varying thickness and composition were deposited onto the cleaned ITO via oCVD as described above. Samples were exposed to air for approximately 10 minutes in transferring them to a glovebox. The devices were then completed in a separate chamber by sequential deposition of C_{60} (10, 30, or 40 nm), BCP (8 nm), and a 100 nm-thick Ag cathode via thermal evaporation at a rate of 0.1 nm/s at 10^{-6} Torr. C_{60} (99.9%, sublimed, Sigma-Aldrich) was purified once by vacuum train sublimation prior to loading, while bathocuproine (BCP, from Luminescence Technology Corp.) and Ag (Alfa Aesar, 1-3 mm shot, 99.9999%) were used as purchased. The cathode films were deposited through a shadow mask, and an active device area of 1 x 1.2 mm^2 was defined by the overlap of all electrodes and organic materials. There were 10 devices per substrate. The OPV current-density-voltage (J-V) measurements were recorded by a Keithley 6487 picoammeter and 100 $\pm$ 10 mW cm^{-2} illumination

was provided by a nitrogen-glovebox-integrated 1kW xenon arc-lamp (Newport 91191) equipped with an AM1.5G filter. The solar simulator intensity was measured with a calibrated silicon photodiode.

5.4 Results and Discussion

5.4.1 Deposition of Mixed Layers

A new oCVD reactor chamber was built that enabled the deposition of oCVD films simultaneously with other evaporated molecules (as described in Chapter 1 and Appendix A). Specifically, the new reactor chamber is equipped with four evaporation sources to allow for the co-evaporation of multiple different materials. For this study, only two evaporation sources were used: one each for $FeCl_3$ and C_{60}. The substrate stage is also capable of rotating, which is a new feature for the oCVD reactors. This allows for greater uniformity across the entire stage to reduce flow pattern effects. Thermal evaporation of C_{60} and other small molecules is typically performed at pressures of ~10^{-6} Torr. However, oCVD depositions are normally performed at ~50 – 300 mTorr. Thus it was desirable to be able to deposit C_{60} at higher pressures of 75 mTorr. At such high pressures the mean free path (λ) significantly drops. For example, $\lambda \approx 32$ m at 10^{-6} Torr, but only ~0.5 mm at 75 mTorr. Thus, the deposition process becomes significantly less line-of-sight and the rate of deposition drops considerably. However, it has previously been shown in the literature that it is possible to deposit small molecule organics at high pressures by using a carrier gas passing over the boats' surfaces.[26, 27] Thus, a N_2 carrier gas was added below the C_{60} evaporation source to help transport the C_{60} molecule to the stage 20 cm above it. To further aid the deposition at higher pressures, the monomer flow direction was also changed. Historically, the monomer flow in the oCVD reactor has been parallel to the substrate stage as the monomer inlet ports were on the side wall. Only the $FeCl_3$ was directly pointed at the stage. Here a gas

feedthrough was used to direct the monomer flow towards rather than across the stage so as to not impede the C_{60} deposition. A diagram of the modified reactor setup is shown in Figure 5-1.
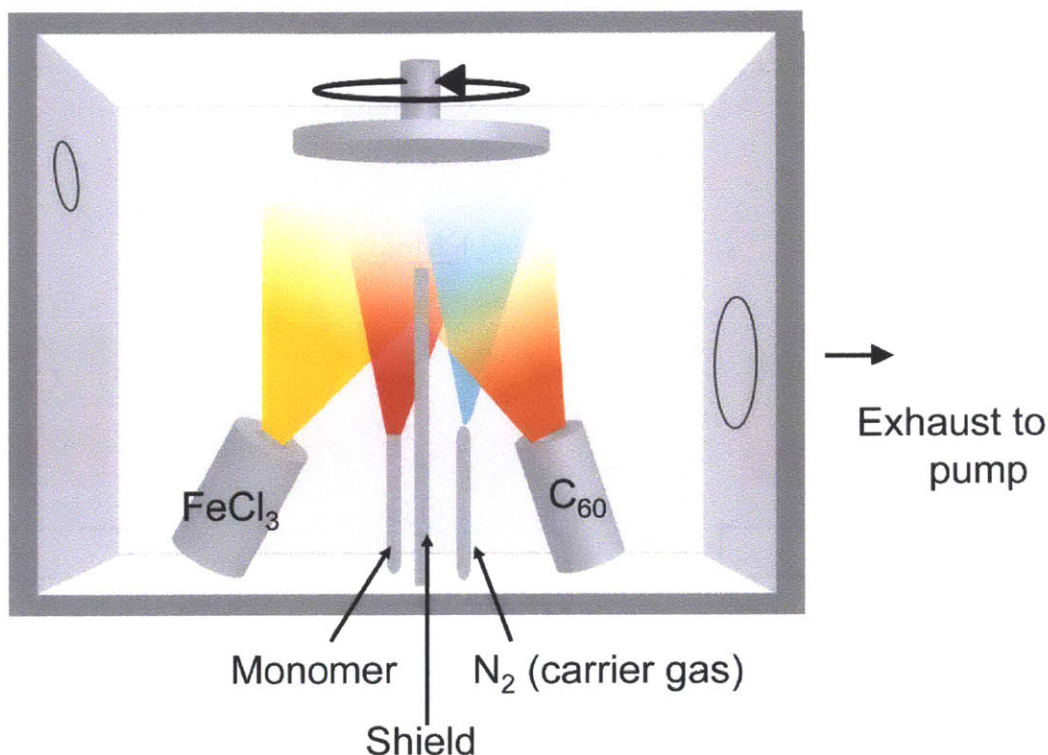
Figure 5-1. Modified oCVD reactor design for the co-deposition of an oCVD polymer and small molecule (C_{60}) with the aid of a carrier gas.

The PT and C_{60} were found to deposit at rates of ~0.8 nm/min and ~1 nm/min, respectively, for the conditions used.

Various device architectures were investigated as potential routes to improve device performance. As the materials used for this study were held fixed (PT and C_{60}), the improvement relative to the planar devices was anticipated to come mainly from increased absorption and thus higher J_{sc}. The device architectures investigated are shown in Figure 5-2. The planar mixed heterojunction (PMHJ) is essentially a planar heterojunction device with a thin mixed layer at the

middle. The bulk heterojunction (BHJ) is a complete mixing of the PT and C_{60} from co-evaporation of C_{60}, thiophene, and $FeCl_3$ during the entire deposition process. The multilayer structures were formed by alternating between depositions of oCVD PT and C_{60} by turning the N_2 carrier gas on and off for desired time intervals. The multilayer—PT (MLP) devices have a higher PT content, while the multilayer—C_{60} (MLC) devices have more C_{60}.
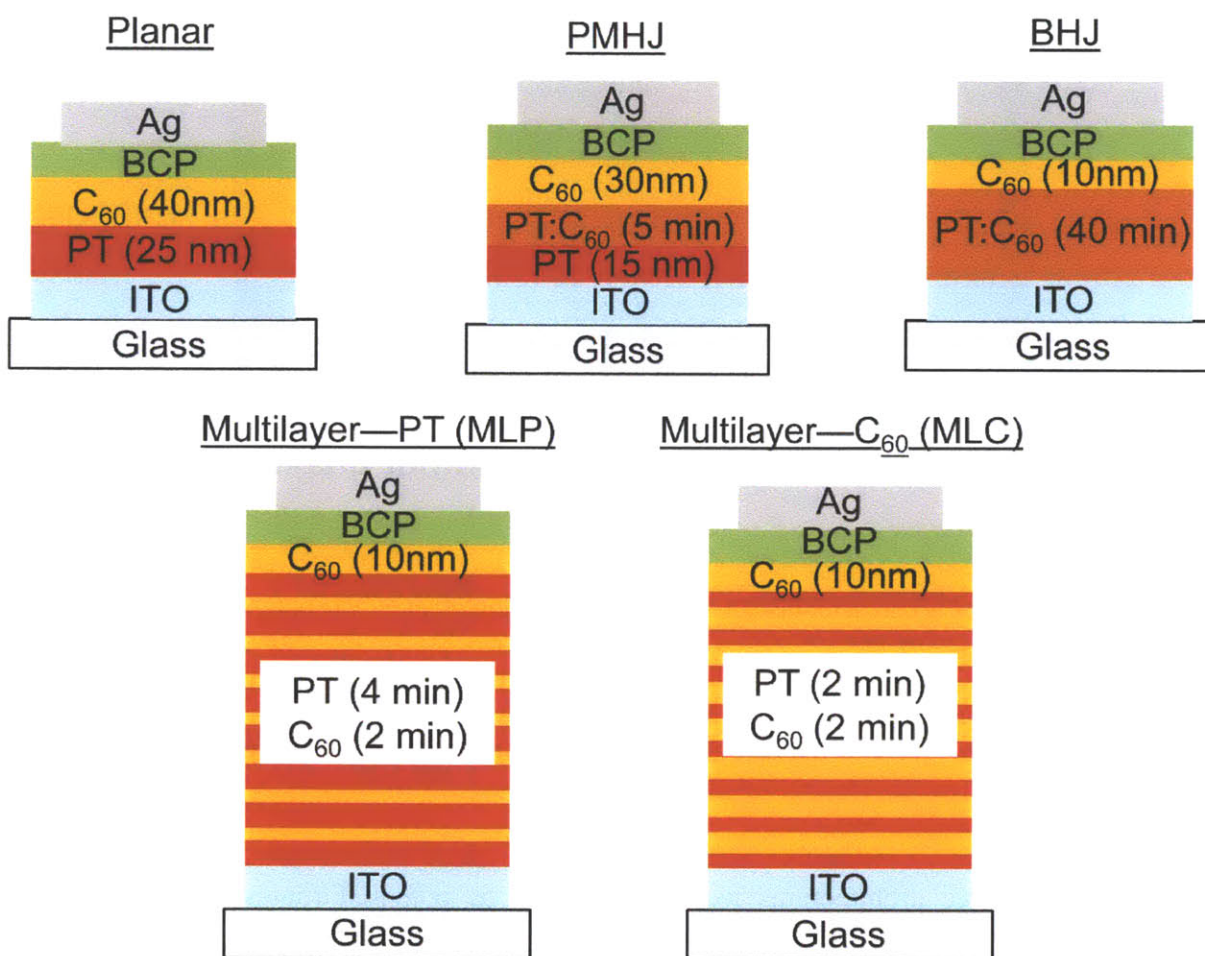
Figure 5-2. Device architectures used in this study using mixed films of oCVD PT and C_{60} deposited in an oCVD reactor chamber. Times shown represent material evaporation times for mixed or alternating layers.

All of these structures are analogous to those that have previously been used for thermally evaporated small molecule solar cells, including the alternating multilayer structure which was accomplished by rotating the stage through physically separated evaporation regions.[28]

The vapor deposition process offers unique control over the timing and thickness of the layers being deposited. This is in contrast to OPVs fabricated using solution-based methods in which the weight percentages of the initial solution can be accurately controlled but the active layer is deposited down in one step.

5.4.2 UV-Vis Absorption

The absorption spectra of the rinsed films deposited in the oCVD reactor (prior to the final C_{60} capping layer and electrodes) are shown in Figure 5-3. For reference, each figure also includes the spectra of oCVD PT and C_{60} deposited at 75 mTorr in the oCVD chamber. As expected, the absorption spectrum of the PMHJ films are dominated by PT, as only a thin mixed layer of PT:C_{60} exists at the top of the film prior to the C_{60} capping layer deposition (Figure 5-3a). However, there is still evidence of the C_{60} in the slightly increased absorption around 300 nm. Fully mixed BHJ, in which C_{60} was co-evaporated with $FeCl_3$ and thiophene for the entire deposition period, provided an extreme case for comparison. Despite efforts to make the films a mixture of roughly half PT and half C_{60}, the films did not appear to have a significant amount of PT in them. The resulting films were typically relatively thin and yellowish-orange in color, likely due to a composition of mostly C_{60} and $FeCl_3$. This is possibly due to the C_{60} and N_2 impeding the polymerization process between the $FeCl_3$ and thiophene. Upon rinsing, excess $FeCl_3$ was dissolved, which also physically removed some of the C_{60} it was embedded in. This resulted in thin films (~30nm) that showed very weak C_{60} absorption features and almost no indication of PT (Figure 5-3b). Because of this difficulty, an approach was taken in which PT and C_{60} were

alternatingly deposited on the substrates to allow the PT to polymerize. The two multilayered structures were deposited to have a higher mass percent of either PT (MLP) or C_{60} (MLC). This is evident in the absorption spectra of the films. The MLP film exhibits PT features most strongly and some features of C_{60} peaks, although they are not very well defined, as shown in Figure 5-3c. On the other hand, the MLC film shows very strong evidence of C_{60} with the characteristic peaks being well defined, while absorption due to PT is much weaker (Figure 5-3d).
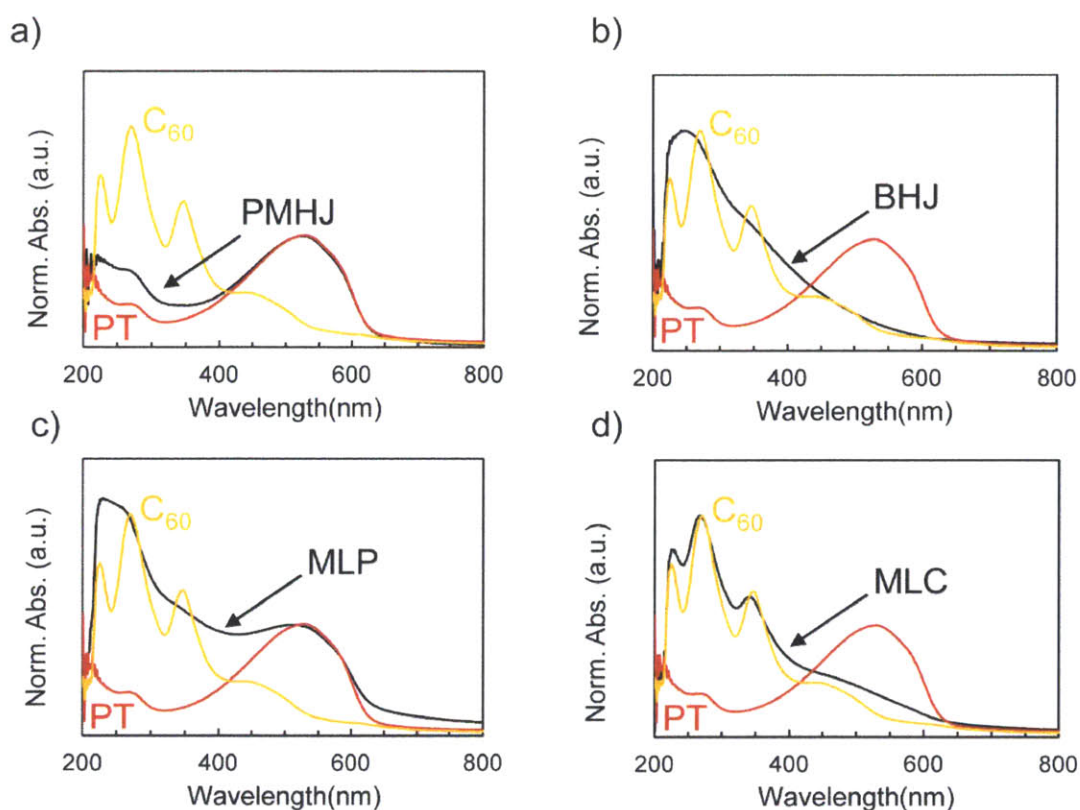
Figure 5-3. UV-vis absorption spectra of various device structures deposited by oCVD. The absorption spectra corroborate the film architectures inferred from the deposition steps, with the exception of the BHJ film that shows weak characteristic absorption peaks for both PT and C_{60}.

5.4.3 Film Morphologies

The surface morphology of the films were analyzed using tapping mode AFM (Figure 5-4). The films' surface features and roughness change significantly for the different film

110

architectures. The planar and BHJ films are the smoothest films (6.0 and 3.9 nm rms, respectively). The high pressures used to deposit the C_{60} likely makes its deposition more conformal and allows it to fill in any gaps in the polymer film to planarize the surface. This effect was previously observed for films of PTCBI deposited by organic vapor phase deposition (OVPD).[27] Interestingly, the PMHJ films exhibit quite large surface features and a high roughness of 20 nm rms. These growths may occur during the deposition of the mixed layer, in which the thiophene concentration is diluted by the C_{60} and N_2. Similar large features have been shown to occur when the thiophene concentration is diluted during deposition (Chapter 3). However, aside from these large features the PMHJ films are quite smooth (~2 nm rms). The MLP films exhibit much larger and pronounced surface features that more closely resemble those discussed in Chapter 3. This results in a surface roughness of 30.6 nm rms. In contrast, during the deposition of the MLC films, PT growth is limited, resulting in much smoother films (6.2 nm rms).
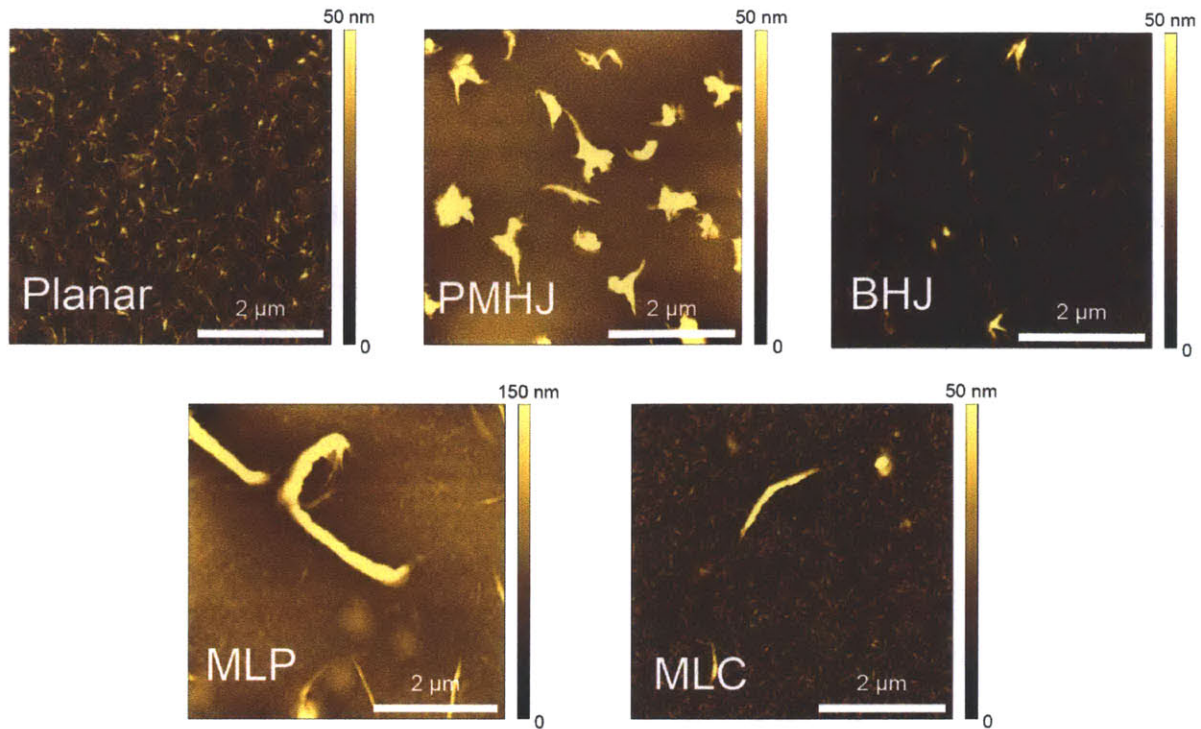
Figure 5-4. AFM topography images of various films deposited in oCVD chamber. Note the differences in scale for the MLP film.

5.4.4 Photovoltaic Device Performance

Devices were then fabricated using these films by thermally evaporating a capping C_{60} layer and then BCP and Ag under high vacuum ($\sim 10^{-6}$ Torr). The C_{60} capping layer generally slightly improved performance and yield, although the devices without this layer performed comparably. The current density-voltage (J-V) curves for the various devices obtained under one sun of air mass 1.5G (AM 1.5G) irradiation (100 mW cm^{-2}) are shown in Figure 5-5. The series resistance (R_{series}) and shunt resistance (R_{shunt}) were estimated from the inverse slope in the J-V curves near V_{oc} and J_{sc}, respectively (Table 5-1). Despite better mixing of the PT and C_{60} in these alternative architectures, none of the devices yield a higher short circuit current density (J_{sc}) than the planar device. The PMHJ device has a J_{sc} roughly half that of the planar device. This device

112

also has a 4x higher series resistance than the planar one. Thus, it appears as though there is poor charge transport through the mixed layer of oCVD PT and C_{60}, resulting in an increase in resistance across the device. The PMHJ device's lower J_{sc} may also partially be due to a thinner C_{60} layer on top (30 nm versus 40 nm in the planar device). As previously shown in external quantum efficiency measurements on the planar oCVD PT/C_{60} devices, the photocurrent in the planar PT/C_{60} devices is largely due to the C_{60}.[23] Thus, it may be possible to slightly increase the current of the PMHJ devices by optimizing the top C_{60} layer thickness further.

a)

b)
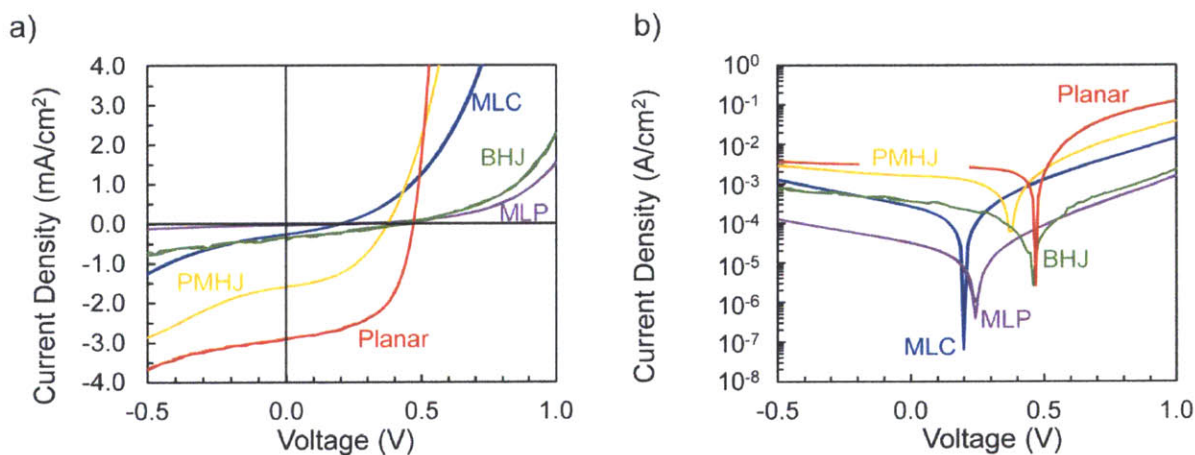
Figure 5-5. a) J-V curves of devices with various architectures utilizing mixed layers of oCVD PT and C_{60}. **b)** J-V curves of the same devices plotted with the absolute value of current density on a logarithmic scale.

The rest of the device architectures have even lower the J_{sc} values, with the MLP devices exhibiting the lowest current. Additionally, they all also exhibited very high series resistances. This suggests that the PT layers greatly add to the series resistance in the devices, which are at least partially responsible for the low currents. Increasing series resistance in the devices generally correlates with decreased J_{sc} and FF in these devices (Table 5-1). The slightly lower current in the MLC device, despite having a lower R_{series} versus the BHJ device, may be due to the much lower

shunt resistance in the MLC devices. Interestingly, the open circuit voltage (V_{oc}) of the BHJ device is quite close to that of the planar device despite having significantly higher series resistance.

Table 5-1. OPV device characteristics for the device architectures investigated in this study.

Device Structure	J_{sc} (mA/cm^2)	V_{oc} (V)	FF	PCE (%)	R_{series} (Ω-cm^2)	R_{shunt} (Ω-cm^2)
Planar PT/C$_{60}$	2.90	0.47	0.56	0.76	20	1020
PMHJ	1.57	0.39	0.46	0.28	90	720
BHJ	0.35	0.46	0.32	0.05	890	1550
MLP	0.03	0.25	0.29	0.002	5360	8150
MLC	0.27	0.20	0.31	0.02	490	120

Poor charge transport was suspected to be a dominant cause for the lower performance in the devices with mixed films. Two potential causes for this are: discontinuous percolation pathways of the PT and C$_{60}$ to their respective electrodes, and traps that serve as recombination sights. To obtain better pathways through the mixed films, various post-deposition annealing treatments were used. This has been shown to be effective for polymer bulk heterojunction solar cells and is now common practice.[29] MLP and MLC films were both thermally and solvent annealed. Thermal annealing was performed in a N$_2$ atmosphere at 120 °C for 20 minutes. Since unsubstituted PT is insoluble in almost all chemicals, 1,2-dichlorobenzene was used for the solvent annealing as C$_{60}$ is highly soluble in it.[30] The solvent annealing was carried out by placing the samples face up in a closed petri dish with 50 μL of solvent for various durations. None of the MLC films annealed at the various conditions functioned after treatment. However, the MLP films continued to function. A summary of the device characteristics after the various annealing conditions is given in Figure 5-6. The one thermal annealing condition attempted resulted in decreased device efficiency. For the solvent annealing treatments, the J_{sc} increases up until 10 minutes of solvent exposure before declining. The V_{oc} initially slightly increases after 1 minute of

solvent annealing, and then decreases before rising again. Changes in the V_{oc} were attributed to changes in the R_{shunt} in the devices at the different annealing time points. The FF remains essentially constant for all conditions. The resulting efficiencies reach a maximum after 1 minute of solvent annealing and then drop below that of the untreated device upon further annealing. However, after about 40 minutes of solvent annealing, efficiency is approximately equal to that of the untreated device. Thus, longer annealing times may provide further efficiency improvements.
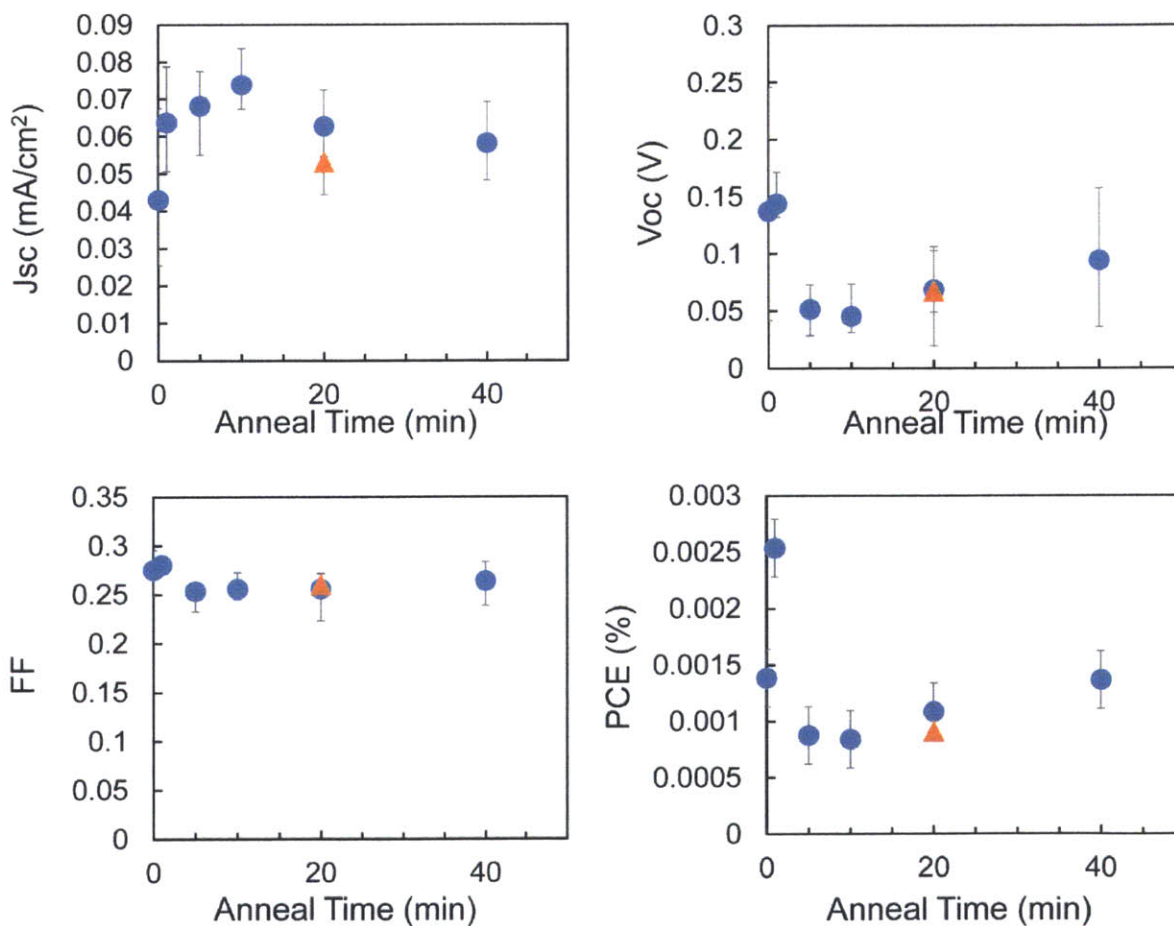

Figure 5-6. Device characteristics using MLP films after various annealing treatments. The blue circles are data from solvent annealing time points using 1,2-dichlorobenzene. The orange triangle represents the thermal annealing (120 °C) data point. Error bars represent maximum and minimum values recorded for functioning devices.

Aside from poor charge conduction pathways, it is possible that traps are introduced during the oCVD deposition in the form of chemical impurities from the $FeCl_3$ or reaction with C_{60}. Chemical purity is known to be an important factor in OPV performance.[31] Additionally, it has been shown that C_{60} can be chlorinated at high temperatures (+250 °C) with Cl_2 gas.[32] In the absence of Cl_2 gas, mixtures of $FeCl_3$ and C_{60} show little evidence of reaction and showed only a very weak C-Cl coupling in the IR absorption spectrum.[33] Although the stage temperature used during the oCVD deposition process is very low (25 °C), the C_{60} is heated to 470 °C to allow it to be evaporated at the high pressures used. Additionally, $FeCl_3$ evaporation is known to be a complicated process that involves several species, including Fe_2Cl_6 which decomposes to 2 $FeCl_2$ and Cl_2.[34, 35] Thus, it is possible that some of the C_{60} is chlorinated while being heated in the crucible and exposed to a low concentration of Cl_2 vapor from the $FeCl_3$ evaporation. Thus, future work should focus on further characterizing the C_{60} to determine if it is chemically altered and potentially identifying more suitable acceptor compounds to use.

5.5 Conclusions

Mixed heterojunction polymer OPVs deposited via the vapor phase were demonstrated by the co-evaporation of C_{60}, $FeCl_3$ and thiophene monomer. Various device architectures were investigated that were characterized by different levels of mixing and mass content of the oCVD PT and C_{60}. The UV-vis absorption spectra of these films confirmed that both PT and C_{60} were present in most of the films, with the exception of the completely co-evaporated film intended to be a BHJ. OPVs fabricated from these films successfully demonstrated a photovoltaic response in light. However, the mixed layers deposited in the oCVD reactor displayed a larger series resistance to charge transport than the pristine PT or C_{60} layers. This successfully demonstrates initial

attempts to make mixed heterojunction OPVs, and future work can build on these results to optimize device performance.

5.6 Acknowledgements

5.7 References

1.   S. Günes, H. Neugebauer and N. S. Sariciftci, *Chem. Rev.*, 2007, 107, 1324-1338.
2.   K. M. Coakley and M. D. McGehee, *Chem. Mater.*, 2004, 16, 4533-4542.
3.   B. C. Thompson and J. M. J. Fréchet, *Angew. Chem. Int. Ed.*, 2008, 47, 58-77.
4.   F. C. Krebs, *Sol. Energy Mater. Sol. Cells*, 2009, 93, 394-412.
5.   Y. Liang, Z. Xu, J. Xia, S.-T. Tsai, Y. Wu, G. Li, C. Ray and L. Yu, *Adv. Mater.*, 2010, 22, E135-E138.
6.   J. You, L. Dou, K. Yoshimura, T. Kato, K. Ohya, T. Moriarty, K. Emery, C.-C. Chen, J. Gao, G. Li and Y. Yang, *Nat Commun*, 2013, 4, 1446.
7.   H.-Y. Chen, J. Hou, S. Zhang, Y. Liang, G. Yang, Y. Yang, L. Yu, Y. Wu and G. Li, *Nat Photon*, 2009, 3, 649-653.
8.   Z. He, C. Zhong, S. Su, M. Xu, H. Wu and Y. Cao, *Nat Photon*, 2012, 6, 591-595.
9.   P. Peumans, S. Uchida and S. R. Forrest, *Nature*, 2003, 425, 158-162.
10.   S. Uchida, J. Xue, B. P. Rand and S. R. Forrest, *Appl. Phys. Lett.*, 2004, 84, 4218-4220.
11.   R. Pandey, A. A. Gunawan, K. A. Mkhoyan and R. J. Holmes, *Adv. Funct. Mater.*, 2012, 22, 617-624.
12.   J. Xue, B. P. Rand, S. Uchida and S. R. Forrest, *Adv. Mater.*, 2005, 17, 66-71.
13.   L. Chen, Y. Tang, X. Fan, C. Zhang, Z. Chu, D. Wang and D. Zou, *Org. Electron.*, 2009, 10, 724-728.
14.   R. Pandey and R. J. Holmes, *Adv. Mater.*, 2010, 22, 5301-5305.
15.   G. Chen, H. Sasabe, Z. Wang, X.-F. Wang, Z. Hong, Y. Yang and J. Kido, *Adv. Mater.*, 2012, 24, 2768-2773.
16.   Z. Wang, D. Yokoyama, X.-F. Wang, Z. Hong, Y. Yang and J. Kido, *Energy & Environmental Science*, 2013, 6, 249-255.
17.   M. Zhang, H. Wang, H. Tian, Y. Geng and C. W. Tang, *Adv. Mater.*, 2011, 23, 4960-4964.
18.   W. E. Tenhaeff and K. K. Gleason, *Adv. Funct. Mater.*, 2008, 18, 979-992.
19.   H. Park, R. M. Howden, M. C. Barr, V. Bulović, K. Gleason and J. Kong, *ACS Nano*, 2012, 6, 6370-6377.

20.	M. C. Barr, R. M. Howden, R. R. Lunt, V. Bulović and K. K. Gleason, *Advanced Energy Materials*, 2012, 2, 1404-1409.

21.	M. C. Barr, J. A. Rowehl, R. R. Lunt, J. Xu, A. Wang, C. M. Boyce, S. G. Im, V. Bulović and K. K. Gleason, *Adv. Mater.*, 2011, 23, 3500-3505.

22.	S. G. Im and K. K. Gleason, *Macromolecules*, 2007, 40, 6552-6556.

23.	D. C. Borrelli, M. C. Barr, V. Bulović and K. K. Gleason, *Sol. Energy Mater. Sol. Cells*, 2012, 99, 190-196.

24.	D. Bhattacharyya, R. M. Howden, D. C. Borrelli and K. K. Gleason, *J. Polym. Sci., Part B: Polym. Phys.*, 2012, 50, 1329-1351.

25.	S. R. Forrest, *Chem. Rev.*, 1997, 97, 1793-1896.

26.	M. Baldo, M. Deutsch, P. Burrows, H. Gossenberger, M. Gerstenberg, V. Ban and S. Forrest, *Adv. Mater.*, 1998, 10, 1505-1514.

27.	F. Yang, M. Shtein and S. R. Forrest, *Nat Mater*, 2005, 4, 37-41.

28.	J. W. Kim, H. J. Kim, H. H. Lee, T. Kim and J.-J. Kim, *Adv. Funct. Mater.*, 2011, 21, 2067-2071.

29.	G. Li, V. Shrotriya, Y. Yao and Y. Yang, *J. Appl. Phys.*, 2005, 98, -.

30.	R. S. Ruoff, D. S. Tse, R. Malhotra and D. C. Lorents, *The Journal of Physical Chemistry*, 1993, 97, 3379-3383.

31.	R. F. Salzman, J. Xue, B. P. Rand, A. Alexander, M. E. Thompson and S. R. Forrest, *Org. Electron.*, 2005, 6, 242-246.

32.	G. A. Olah, I. Bucsi, C. Lambert, R. Aniszfeld, N. J. Trivedi, D. K. Sensharma and G. K. S. Prakash, *J. Am. Chem. Soc.*, 1991, 113, 9385-9387.

33.	J. C. L. Chow, P. K. Ummat and W. R. Datars, *Mater. Res. Bull.*, 1999, 34, 1749-1756.

34.	S. Blairs, The Journal of Chemical Thermodynamics, 2006, 38, 1484-1488.

35.	L. E. Wilson and N. W. Gregory, *The Journal of Physical Chemistry*, 1958, 62, 433-437.

Chapter 6

Efficiency Enhancement Using DBP in Energy Cascade Polymer Solar Cells

6.1 Abstract

Ternary organic solar cells are a promising approach to improving the performance of organic photovoltaics (OPVs). Here we demonstrate a three-layer energy cascade OPV with dibenzotetraphenylperiflanthene (DBP) as the intermediate layer between a polymer donor and C_{60} acceptor layers. For this study, the donor polymer used is unsubstituted polythiophene (PT) deposited by a vapor-phase technique since it has favorable energy alignments. The PT/DBP and DBP/C_{60} heterojunctions were both shown to be photoactive through fabrication and testing of these devices. Addition of 10 nm intermediate DBP layer into the PT/C_{60} structure significantly improves the device efficiency, mainly through increases in the J_{sc} and V_{oc}. Device efficiencies up to 2.4% are achieved using this energy cascade device architecture.

6.2 Introduction

The power conversion efficiencies of organic solar cells have significantly increased since Tang discovered the effectiveness of the donor/acceptor interface for exciton dissocation.[1] These improvements have come from a combination of materials and device architecture engineering. The introduction of bulk heterojunction structures provided a large boost in device efficiency, mostly through improved current.[2-4] Additionally, tandem structures, in which multiple heterojunctions are stacked on top of each other have also provided a means to higher efficiencies. In fact, the highest reported efficiencies for organic photovoltaics (10.7% for solution-processed polymers and 12% for vacuum-deposited small molecules) were fabricated with tandem architectures.[5, 6] However, the open circuit voltage (V_{oc}) of bulk heterojunction devices is limited by the choice of donor and acceptor,[7] and the short circuit current (J_{sc}) of tandem devices is limited to that of the subcell with the smallest current.[8]

An alternative device architecture that is recently gaining interest is a ternary organic solar cell in which three active materials are used.[9] Absorption in this additional layer can lead to increased device photocurrent. Furthermore, the V_{oc} can also be simultaneously improved with careful materials selection. For polymer solar cells, ternary solar cells are typically fabricated by dissolving the three components in solution before casting the films.[10, 11] For thermally evaporated small molecule solar cells, ternary devices have been made by including an interfacial layer between a single heterojunction.[12, 13] Recently, researchers have achieved efficiencies up to 8.4% using fullerene-free ternary OPVs.[14] By selecting an intermediate layer with highest occupied molecular orbital (HOMO) and lowest unoccupied molecular orbital (LUMO) energy levels in between those of the donor and acceptor, a cascade-energy-level-alignment (CELA) structure is created.[15, 16] This effectively creates two charge-generating heterojunctions, which has been shown to increase J_{sc} and V_{oc} through enhanced absorption and reduced recombination.[17-19]

Here we investigate an energy cascade OPV with three active layers using a bottom donor layer of unsubstituted polythiophene (PT) prepared by oxidative chemical vapor deposition (oCVD). Dibenzotetraphenylperiflanthene (DBP) is used as an interlayer material and C_{60} is the top electron acceptor. Planar heterojunction OPVs with a DBP donor and a C_{60} acceptor are known to have a high V_{oc} (0.92 V) and be relatively efficient (η = 3.6% for optimized thicknesses).[20] By combining the PT/DBP and DBP/C_{60} heterojunctions in a three-layer cascade architecture, we show a larger photocurrent than in any of the constituent bilayer cells and a larger V_{oc} than the PT/C_{60} cell.

6.3 Experimental

oCVD PT films were deposited onto ITO-coated glass (Thin Film Devices, 50 Ω/sq) for device fabrication. Prior to use, the substrates were cleaned with detergent and solvents, followed by O_2 plasma for 30 seconds. The oCVD PT was deposited as previously described in a custom-designed vacuum chamber.[21] PT was simultaneously synthesized and deposited from vapor phase thiophene monomer (>99%, Sigma-Aldrich) and sublimed $FeCl_3$ oxidant (97%, Sigma-Aldrich) over a 30-minute deposition period to form solid polymer films. A chamber pressure of 75 mTorr and substrate temperature of 25 °C were used. After deposition, the films were rinsed in methanol ($\geq$99.9%, Sigma-Aldrich) for 20 minutes, 0.2M HCl in methanol for 10 minutes, followed by 1 minute in methanol to remove reacted and excess oxidant. The OPV devices were then completed in a separate high-vacuum chamber ($\sim$10^{-6} Torr) by thermal evaporation of organic materials and metal top electrode at a rate of 0.1 nm/s. C_{60} (99.9%, sublimed, Sigma-Aldrich) was purified once by vacuum train sublimation prior to loading,[22] while DBP (Luminescence Technology Corp.), bathocuproine (BCP, Luminescence Technology Corp.) and Ag (99.9999%, 1-3 mm shot, Alfa Aesar) were used as purchased. The cathode films were deposited through a shadow mask, defining an active device area of 1 x 1.2 mm^2 from the overlap of all electrodes and organic materials. There were 10 devices per substrate. The OPV current-density-voltage (J-V) measurements were recorded by a Keithley 6487 picoammeter and 100 ± 10 mW cm^{-2} illumination was provided by a nitrogen-glovebox-integrated 1kW xenon arc-lamp (Newport 91191) equipped with an AM1.5G filter. The solar simulator intensity was measured with a calibrated silicon photodiode.

6.4 Results and discussion

Figure 6-1a shows the absorbance spectra of 50 nm films of the materials used in this work and their molecular structure.
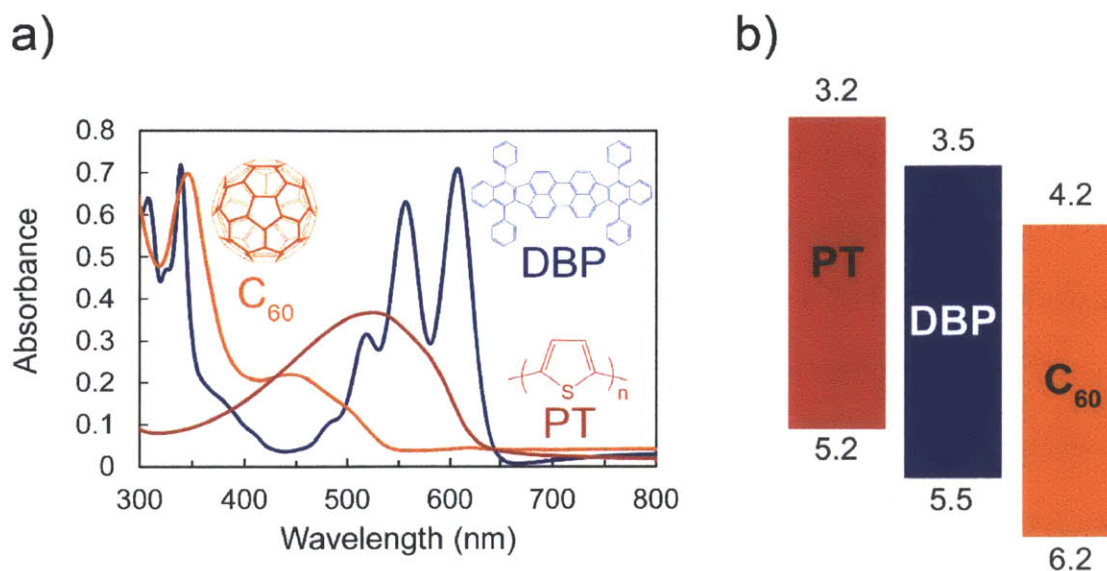
Figure 6-1. a) Absorbance spectrum of 50 nm films of oCVD PT, DBP, and C_{60} with their respective molecular structures. **b)** energy levels of oCVD PT, DBP, and C_{60}.

PT absorbs more strongly than DBP between 400 nm until slightly past the peak in the PT absorption spectrum around 530 nm. Between ~550 and 650 nm, DBP absorbs more strongly than PT and exhibits two strong absorption peaks in this region at 607 and 557 nm. Thus, addition of the DBP layer could augment the PT absorption. DBP and C_{60} both absorb strongly at low wavelengths of ~350 nm. The energy level diagram for the energy cascade device structure is shown in Figure 6-1b. Energy values for DBP and C_{60} were taken from the literature.[20, 23] The oCVD PT HOMO energy level was calculated from previously published cyclic voltammetry measurements and an absolute redox potential energy value of ferrocene/ ferrocenium of -4.76 eV.[21, 24] The PT LUMO was calculating by adding the optical bandgap to the HOMO. The lower-

lying HOMO (5.5 vs 5.2 eV) and LUMO (3.5 vs 3.2 eV) energy levels of DBP compared to PT makes hole and electron transport in the desired directions energetically possible.

Planar bilayer heterojunction PT/DBP and DBP/C_{60} OPVs were first fabricated to verify that all heterojunctions effectively separate charge. The current density-voltage (J-V) curves for these devices are shown in Figure 6-2. The J-V curve for a PT/C_{60} device is also included for comparison. All devices give a photovoltaic response under light. Both PT/DBP and DBP/C_{60} heterojunctions result in higher V_{oc} values than for the PT/C_{60} device. The PT/DBP devices have a particularly high V_{oc} of 1.02 V. This is likely due to the large offset in energy levels between the HOMO of PT and the LUMO of DBP of 1.7 eV (Figure 6-1b). It should also be noted that the layer thicknesses were not fully optimized for device performances. For example, using a thinner DBP layer for the PT/DBP devices should lead to higher efficiencies through increased current and fill factor (FF). The low current and FF in these devices is likely due to relatively low electron mobility through the 40 nm DBP layer. Additionally, for the DBP/C_{60} devices, a thicker DBP layer should result in higher efficiencies. However, devices using 10 nm of DBP were included as it is helpful for comparison to the optimized energy cascade structure, as described below.
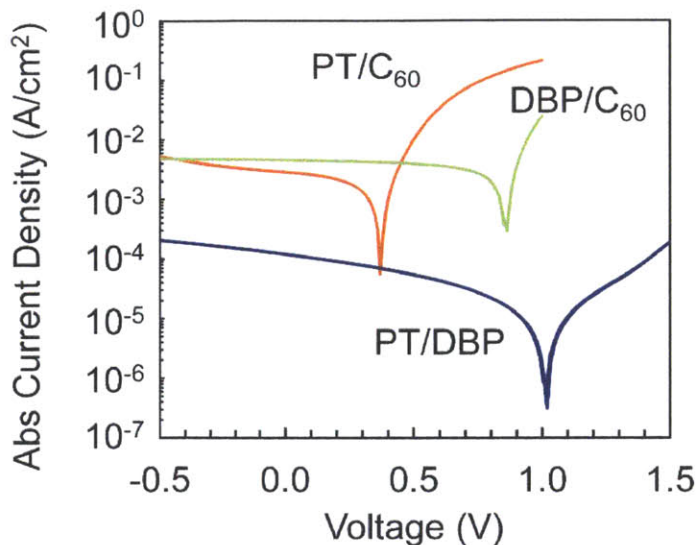
Figure 6-2. J-V curves for OPVs with oCVD PT (30nm)/C_{60} (40nm), oCVD PT (30 nm)/DBP (40nm) and DBP (10nm)/C_{60} (40 nm).

Ternary energy cascade devices were then fabricated with an architecture of PT/DBP/C_{60}. In order to optimize the performance of these devices, a series of OPVs with a range of DBP thicknesses were fabricated. For this optimization, the PT and C_{60} layer thicknesses were kept constant at 30 nm and 40 nm, respectively. Figure 6-3 shows the J-V curves of devices using various DBP layer thicknesses. Device efficiency achieves a maximum for a DBP thickness of 10 nm.

Figure 6-3. J-V curves for energy cascade devices using various intermediate DBP layer thicknesses in PT(30 nm) /DBP (x nm)/C_{60}(40 nm) devices. Efficiency is optimized for a DBP thickness of 10 nm.

Figure 6-4 provides a detailed summary of how the device characteristics evolve with variations in the DBP layer thickness. Inse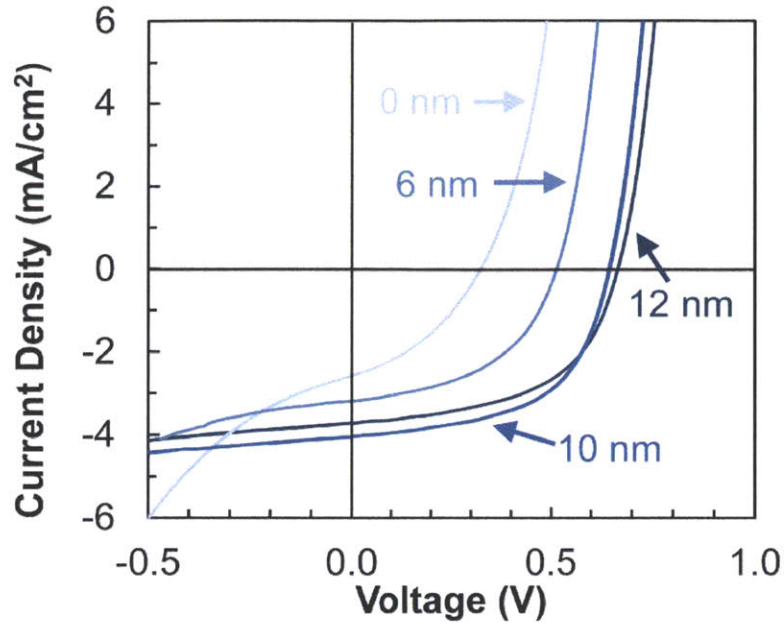rtion of even a 4 nm thin DBP layer increases the device photocurrent, likely through added absorption by the DBP layer. Additionally, the V_{oc} increases as the DBP thickness increases. This is potentially from reduced recombination of electrons in the C_{60} with holes in the PT. It is also expected that the V_{oc} of CELA devices is set by the V_{oc} of the lowest voltage heterojunction (DBP/C_{60} in this case).[25] Due to the PT roughness (~6 nm rms) and the DBP film growth process, thin layers of DBP likely provide incomplete coverage that leaves some area for PT/C_{60} interfaces to occur. Increasing the DBP thickness results in more complete coverage of the PT, converting all C_{60} interfaces to DBP/C_{60} and thus increasing the total V_{oc}. Beyond 10 nm of DBP, the low electron mobility of DBP adds extra resistance through the device, lowering the FF and efficiency. Thus the three-layer devices reach a maximum efficiency for 10 nm of DBP.
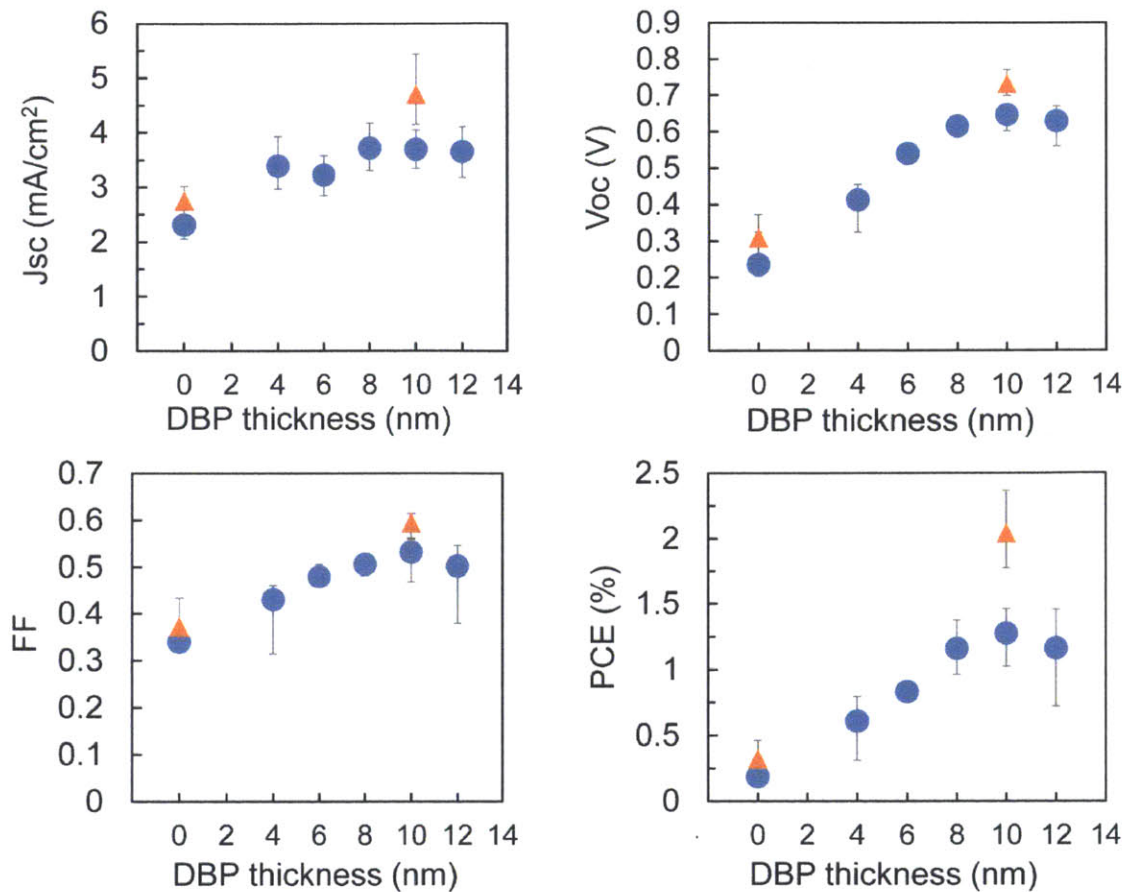
Figure 6-4. Summary of J_{sc}, V_{oc}, FF, and power conversion efficiency (PCE) for three-layer energy cascade OPVs for various intermediate layer DBP thicknesses. Orange triangles represent data points data using an oCVD PT film prepared from a separate deposition.

Additional devices were made using PT from a separate deposition that resulted in higher efficiency PT/C_{60} control devices (orange triangles in Figure 6-4). This resulted in increased device efficiency for the optimized CELA devices to 2.4%. This is a significant increase compared to the 0.46% efficiency for the PT/C_{60} devices. Both the J_{sc} and V_{oc} are roughly doubled in comparison to the PT/C_{60} device. The J-V curves of the optimized PT/DBP/C_{60} device are shown in Figure 6-5, along with the J-V curves of PT/C_{60} and DBP/C_{60} for comparison. The device performance characteristics are summarized in Table 6-1.

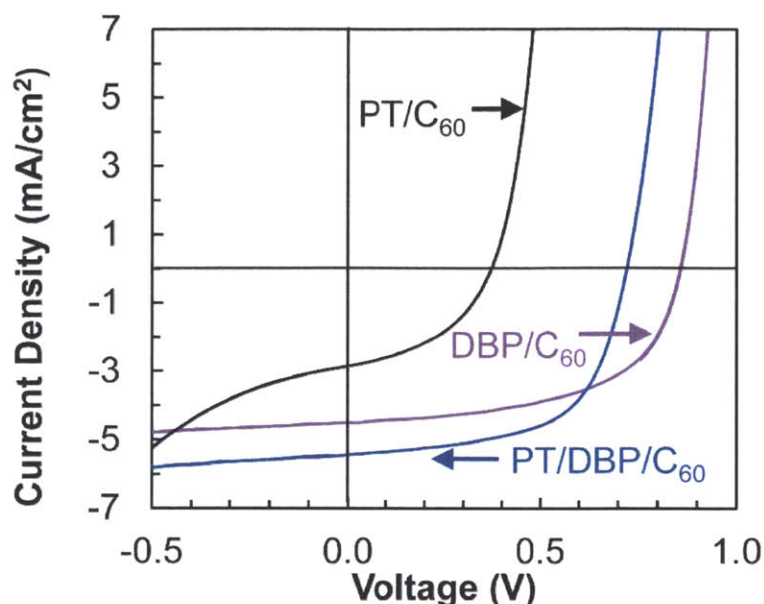**Figure 6-5.** J-V curve for the optimized energy cascade OPVs having a structure of PT(30 nm)/DBP(10 nm)/C_{60}(40 nm). Also shown are the J-V curves for PT(30 nm)/C_{60}(40 nm) and DBP(10 nm)/C_{60}(40 nm) devices.

Table 6-1. Summary of device characteristics for control devices of constituent heterojunctions and optimized three-layer energy cascade device.

Structure (thickness in nm)	J_{sc} (mA/cm^2)	V_{oc} (V)	FF	PCE (%)
ITO/PT(30)/C_{60}(40)	2.86	0.37	0.43	0.46
ITO/PT(30)/DBP(40)	0.12	1.02	0.22	0.03
ITO/DBP(10)/C_{60}(40)	4.49	0.86	0.57	2.21
ITO/PT(30)/DBP(10)/C_{60}(40)	5.44	0.72	0.60	2.37

6.5 Conclusions

A three-layer energy cascade OPV was demonstrated with DBP as the intermediate layer between a PT polymer donor and C_{60} acceptor layers. PT/DBP and DBP/C_{60} devices were both shown to be photoactive. Addition of an intermediate DBP layer into the PT/C_{60} structure significantly improves the device efficiency, mainly through increases in the J_{sc} and V_{oc}. The increase in J_{sc} is likely due to increased active layer absorption from the added DBP. The optimal intermediate DBP layer thickness is 10 nm, after which the FF begins to drop. This optimized

structure resulted in power conversion efficiencies up to 2.4%, which is a significant improvement over the planar heterojunction PT/C_{60} device efficiency of 0.5%. Thus, we have shown that DBP can effectively be used in vapor-deposited energy cascade OPVs. Furthermore, since DBP is soluble in solvents commonly used for solution-processed polymers, such as chlorobenzenes,[26] mixing DBP in with solution-processed bulk heterojunction polymer solar cells could help improve efficiency.

6.5 Acknowledgments

6.6 References

1. C. W. Tang, *Appl. Phys. Lett.*, 1986, 48, 183-185.
2. P. Peumans, S. Uchida and S. R. Forrest, *Nature*, 2003, 425, 158-162.
3. Z. Wang, D. Yokoyama, X.-F. Wang, Z. Hong, Y. Yang and J. Kido, *Energy & Environmental Science*, 2013, 6, 249-255.
4. Y. Liang, Z. Xu, J. Xia, S.-T. Tsai, Y. Wu, G. Li, C. Ray and L. Yu, *Adv. Mater.*, 2010, 22, E135-E138.
5. J. You, L. Dou, K. Yoshimura, T. Kato, K. Ohya, T. Moriarty, K. Emery, C.-C. Chen, J. Gao, G. Li and Y. Yang, *Nat Commun*, 2013, 4, 1446.
6. 12.0% efficienct vacuum-deposited molecular OPV (Heliatek), http://www.heliatek.com/newscenter/latest_news/neuer-weltrekord-fur-organische-solarzellen-heliatek-behauptet-sich-mit-12-zelleffizienz-als-technologiefuhrer/?lang=en, Accessed April 14, 2014.
7. M. C. Scharber, D. Mühlbacher, M. Koppe, P. Denk, C. Waldauf, A. J. Heeger and C. J. Brabec, *Adv. Mater.*, 2006, 18, 789-794.
8. A. Yakimov and S. R. Forrest, *Appl. Phys. Lett.*, 2002, 80, 1667-1669.
9. T. Ameri, P. Khoram, J. Min and C. J. Brabec, *Adv. Mater.*, 2013, 25, 4245-4266.
10. M. C. Chen, D. J. Liaw, Y. C. Huang, H. Y. Wu and Y. Tai, *Sol. Energy Mater. Sol. Cells*, 2011, 95, 2621-2627.
11. J.-S. Huang, T. Goh, X. Li, M. Y. Sfeir, E. A. Bielinski, S. Tomasulo, M. L. Lee, N. Hazari and A. D. Taylor, *Nat Photon*, 2013, 7, 479-485.
12. K. Cnops, B. P. Rand, D. Cheyns and P. Heremans, *Appl. Phys. Lett.*, 2012, 101, -.
13. J. Dai, X. Jiang, H. Wang and D. Yan, *Appl. Phys. Lett.*, 2007, 91, -.
14. K. Cnops, B. P. Rand, D. Cheyns, B. Verreet, M. A. Empl and P. Heremans, *Nat Commun*, 2014, 5.

15. C. W. Schlenker, V. S. Barlier, S. W. Chin, M. T. Whited, R. E. McAnally, S. R. Forrest and M. E. Thompson, *Chem. Mater.*, 2011, 23, 4132-4140.

16. G. Zhang, W. Li, B. Chu, L. Chen, F. Yan, J. Zhu, Y. Chen and C. S. Lee, *Appl. Phys. Lett.*, 2009, 94, -.

17. T. D. Heidel, D. Hochbaum, J. M. Sussman, V. Singh, M. E. Bahlke, I. Hiromi, J. Lee and M. A. Baldo, *J. Appl. Phys.*, 2011, 109, -.

18. S. Sista, Y. Yao, Y. Yang, M. L. Tang and Z. Bao, *Appl. Phys. Lett.*, 2007, 91, -.

19. J. C. Wang, S. Q. Shi, C. W. Leung, S. P. Lau, K. Y. Wong and P. K. L. Chan, *Appl. Phys. Lett.*, 2012, 100, -.

20. D. Fujishima, H. Kanno, T. Kinoshita, E. Maruyama, M. Tanaka, M. Shirakawa and K. Shibata, *Sol. Energy Mater. Sol. Cells*, 2009, 93, 1029-1032.

21. D. C. Borrelli, M. C. Barr, V. Bulović and K. K. Gleason, *Sol. Energy Mater. Sol. Cells*, 2012, 99, 190-196.

22. S. R. Forrest, *Chem. Rev.*, 1997, 97, 1793-1896.

23. P. I. Djurovich, E. I. Mayo, S. R. Forrest and M. E. Thompson, *Org. Electron.*, 2009, 10, 515-520.

24. B. W. D'Andrade, S. Datta, S. R. Forrest, P. Djurovich, E. Polikarpov and M. E. Thompson, *Org. Electron.*, 2005, 6, 11-20.

25. A. Barito, M. E. Sykes, D. Bilby, J. Amonoo, Y. Jin, S. E. Morris, P. F. Green, J. Kim and M. Shtein, *J. Appl. Phys.*, 2013, 113, -.

26. J. D. Debad, J. C. Morris, V. Lynch, P. Magnus and A. J. Bard, *J. Am. Chem. Soc.*, 1996, 118, 2374-2379.

Chapter 7

Conclusions

7.1 Summary

The first objective of this thesis was to investigate the use of oCVD for the deposition of semiconducting polymers. After successfully accomplishing this with various thiophene-based monomers, I turned my focus to studying how the oCVD deposition conditions impacted the resulting polymer properties. During the course of my thesis, I also designed and constructed a new oCVD reactor that provided significant new benefits. The new reactor provided improved control and reproducibility over the film properties and uniformity across a larger stage area. Additionally, it enabled the co-evaporation of multiple materials.

Chapters 2 and 3 investigate the dependence of oCVD polymer optoelectronic properties on stage temperature and chamber pressure during deposition, respectively. In Chapter 2, I demonstrate a one-step process to deposit films of low bandgap polyisothianaphthene (PITN) using oCVD. Typical reaction schemes for obtaining films of PITN are otherwise long and difficult. Monotonic variation in the optical and electrical properties of PITN occurred as the substrate temperature was raised from 70 °C to 130 °C. The position of the absorption maxima in the UV-Vis-NIR spectra of dedoped films was considerably red-shifted by over 100 nm with increasing deposition temperature, resulting in a lowering of the bandgap from 1.14 eV to 1.05 eV. Additionally, trends in the FTIR and Raman spectra confirm greater conjugation with increasing temperature. In Chapter 3, I study how the pressure of the oCVD process affects the optoelectronic properties of PT films. Shifts in the Raman and UV-vis absorption spectra suggest that films deposited at the lowest pressure deposition conditions (1 mTorr) have shorter conjugation. Additionally, relative Raman peak intensities suggest that the polymer chains in these films contain more distortions than films deposited at higher pressures. Organic thin film transistors (TFTs) fabricated using oCVD PT as the active channel layer showed that films deposited at 150 mTorr demonstrate the greatest field effect carrier mobility of 4×10^{-3} cm^2 V^{-1}sec^{-1}. Thus, it was identified

that higher pressure conditions (~150 mTorr) are better-suited for depositing absorbing semiconducting films for organics photovoltaics.

The second main goal of this research was to then integrate these semiconducting polymers into OPVs. As a first demonstration of this, I successfully integrated oCVD PT into planar heterojunction OPVs as the electron donor layer in Chapter 4. This was accomplished by depositing the PT directly onto ITO, followed by thermal evaporation of a C_{60} electron acceptor layer and top electrode. Power conversion efficiencies up to 0.8% were achieved using this device architecture. The absorption edge of the PT at ~620 nm closely matches the edge present in the external quantum efficiency spectra, indicating that the oCVD PT contributes to the device photocurrents. Chapter 5 discusses the first demonstration of vapor-deposited mixed heterojunction polymer solar cells. These are accomplished by simultaneously evaporating thiophene monomer, iron(III) chloride oxidizing agent, and C_{60} in a modified oCVD chamber to result in mixed films of oCVD polythiophene (PT) and C_{60}. Various film compositions were deposited and OPVs made using these films were investigated.

Lastly, in Chapter 6 I demonstrated a promising alternative OPV device architecture using a three-layer energy cascade. An intermediate DBP layer was added in between PT donor and C_{60} acceptor layers to result in two active heterojunctions physically in series in the PT/DBP/C60 devices. This architecture is shown to significantly improve device performance through increased current and voltage. Addition of 10 nm intermediate DBP layer into the PT/C_{60} structure results in device efficiencies up to 2.4% using this energy cascade device architecture.

7.2 Concluding Remarks

This thesis successfully demonstrates the use of oCVD for the deposition of semiconducting polymers and their application to organic photovoltaics. Although most of this

thesis focuses on unsubstituted polythiophene and polyisothianaphthene, this technique can easily be extended to the deposition of other semiconducting polymers by changing the monomer used. By utilizing oCVD, the selection of the monomer is no longer constrained by the requirement that the resulting conjugated polymer must be soluble for solution-processing or stable at high temperatures for thermal evaporation. Thus, this opens up a range of materials with potentially desirable properties that can be considered for an active layer material with the goal of improving device efficiency and stability.

The many proof-of-concept ideas demonstrated in this thesis should serve as a solid starting point for future researchers. For example, only homopolymers were explored in this work. A potentially fruitful research direction is in depositing copolymers via oCVD. By carefully selecting the constituent monomers, the energy levels of the semiconducting polymer film can be fine-tuned. This would provide an additional knob for optimizing the OPV efficiencies of devices employing an oCVD donor layer. Additionally, by exploiting the unique ability to conformally coat surfaces with oCVD polymers, it should be possible to create devices with much higher surface area than planar heterojunction devices to increase device photocurrent.

In conclusion, I have shown that oCVD is a viable technique that can combine the benefits of vacuum processing and the use of semiconducting polymers for organic photovoltaics.

Appendix A

oCVD Reactor and Accessory Designs

Note: Figures A-1 through A-19 reprinted with permission from Kurt J. Lesker Company.
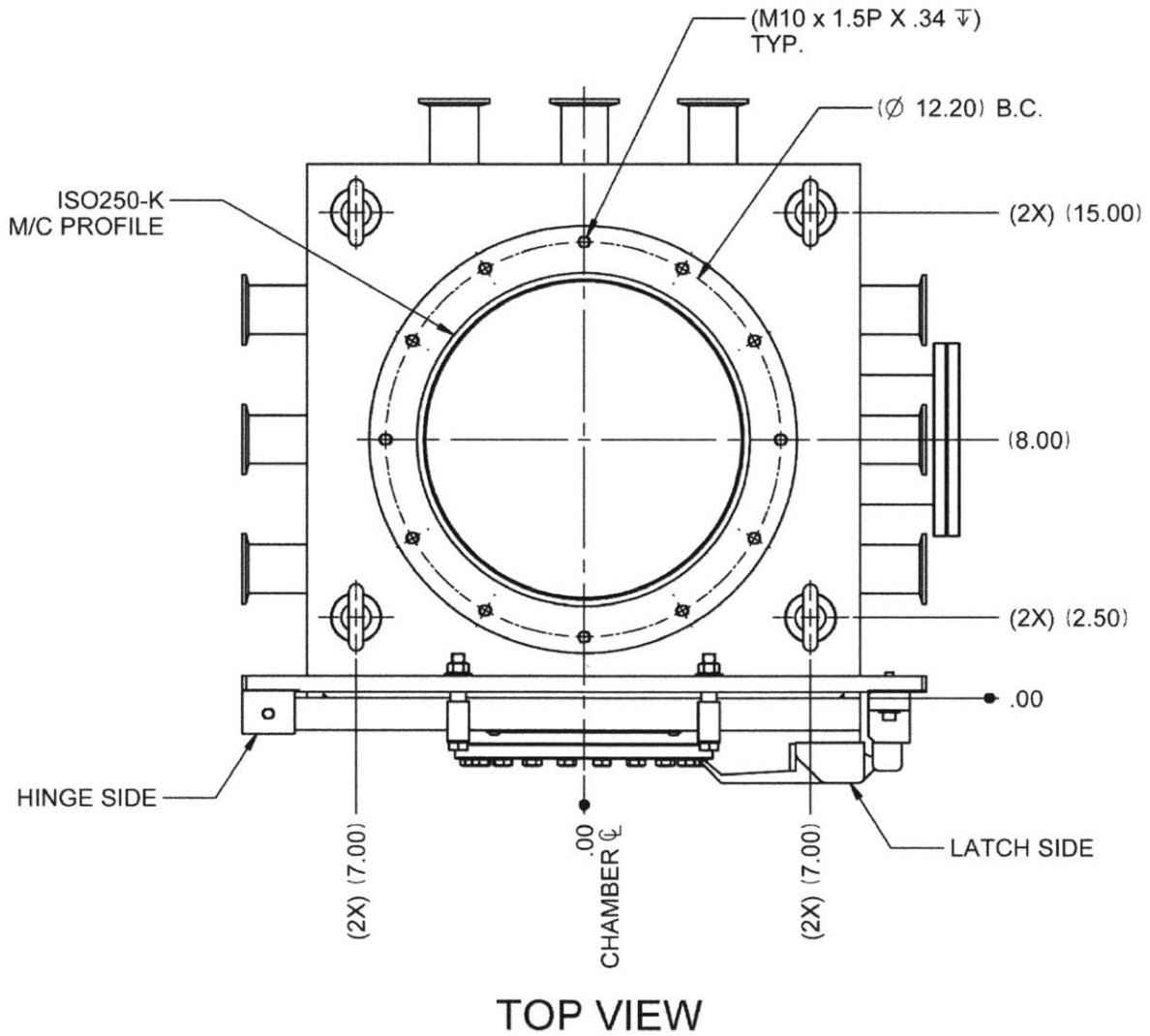

Figure A-1. oCVD reactor chamber engineering drawing—top view. Dimensions in inches.
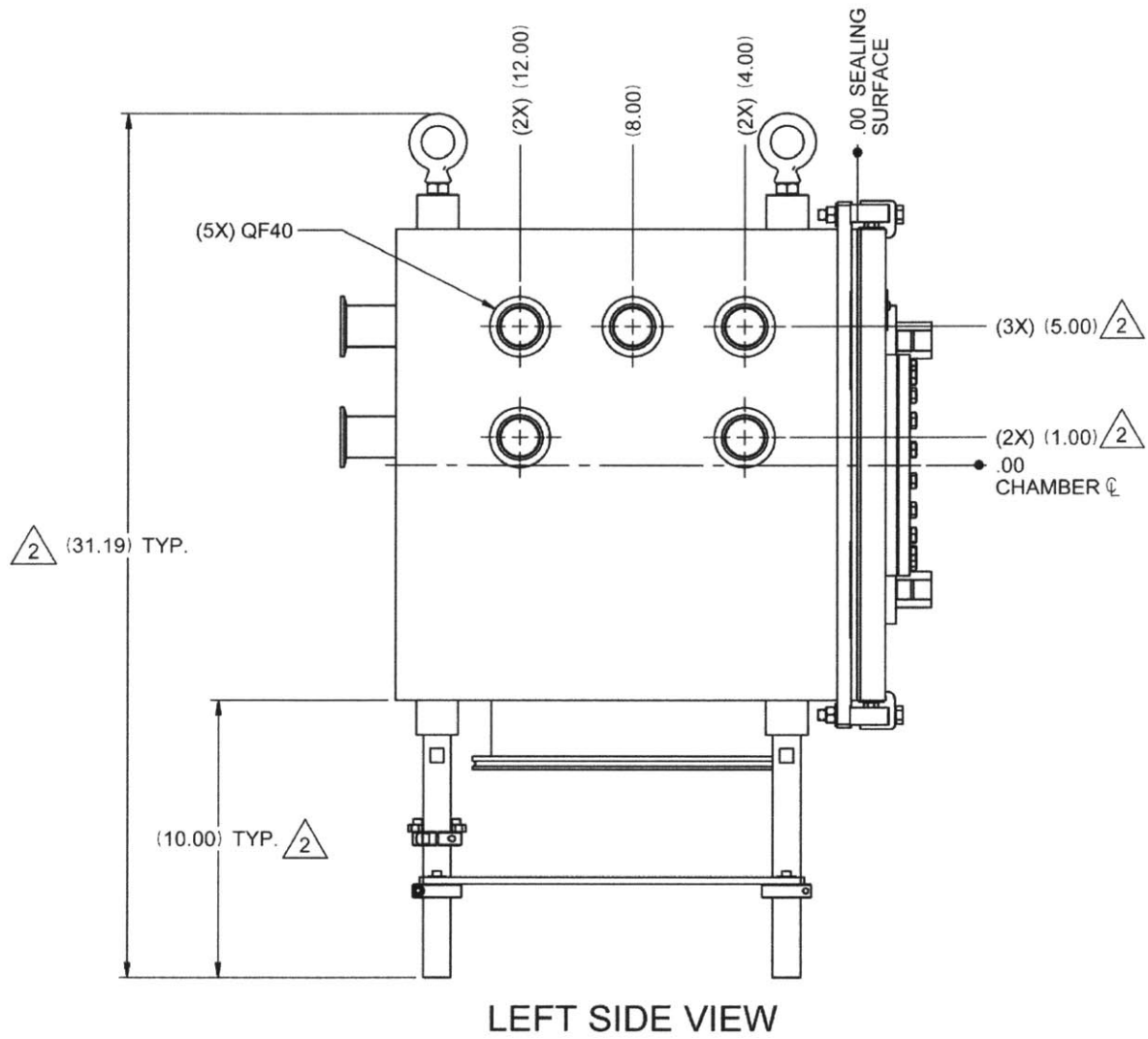
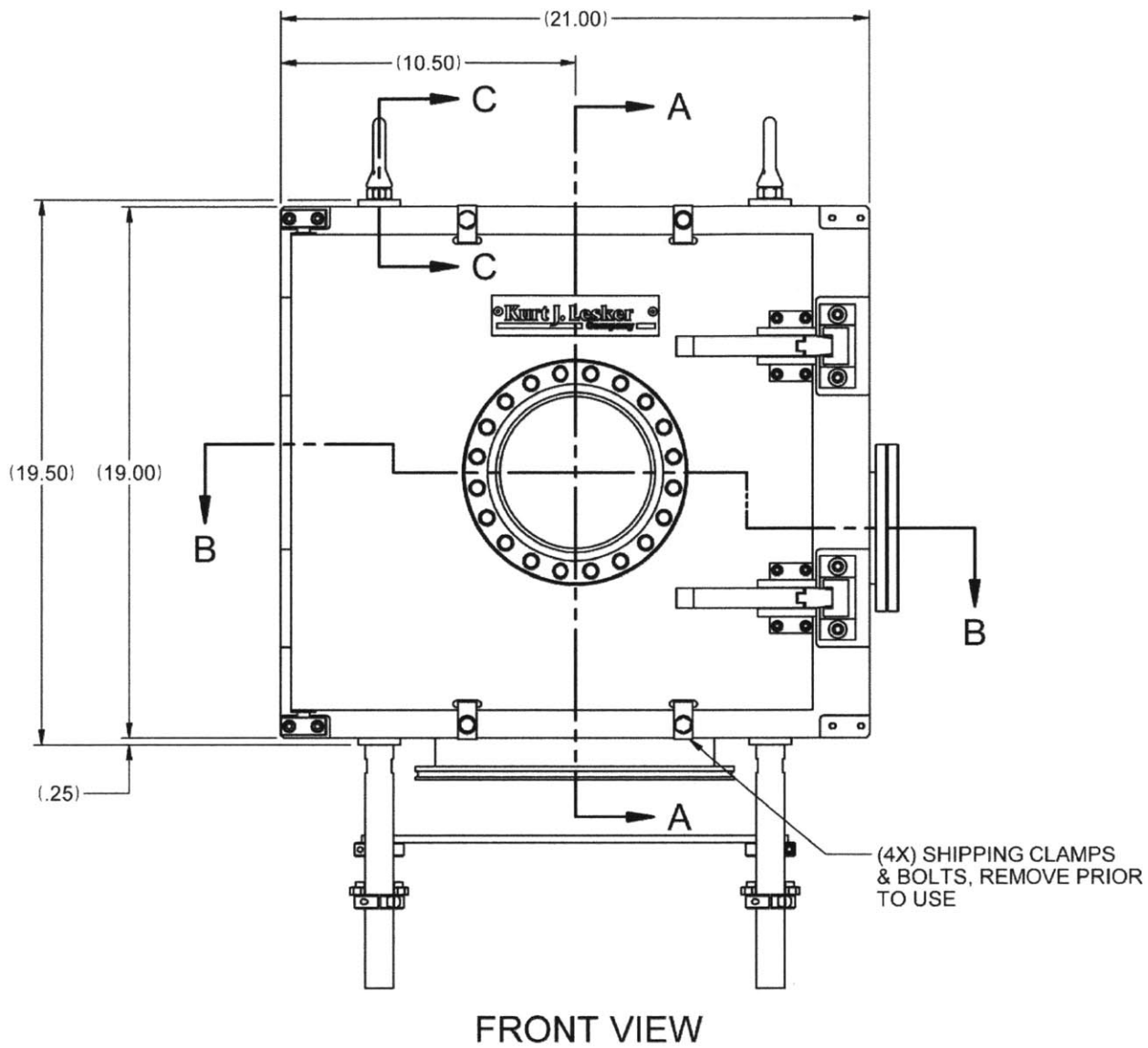**Figure A-2.** oCVD reactor chamber engineering drawing—left view. Dimensions in inches.

137

FRONT VIEW

Figure A-3. oCVD reactor chamber engineering drawing—front view. Dimensions in inches.
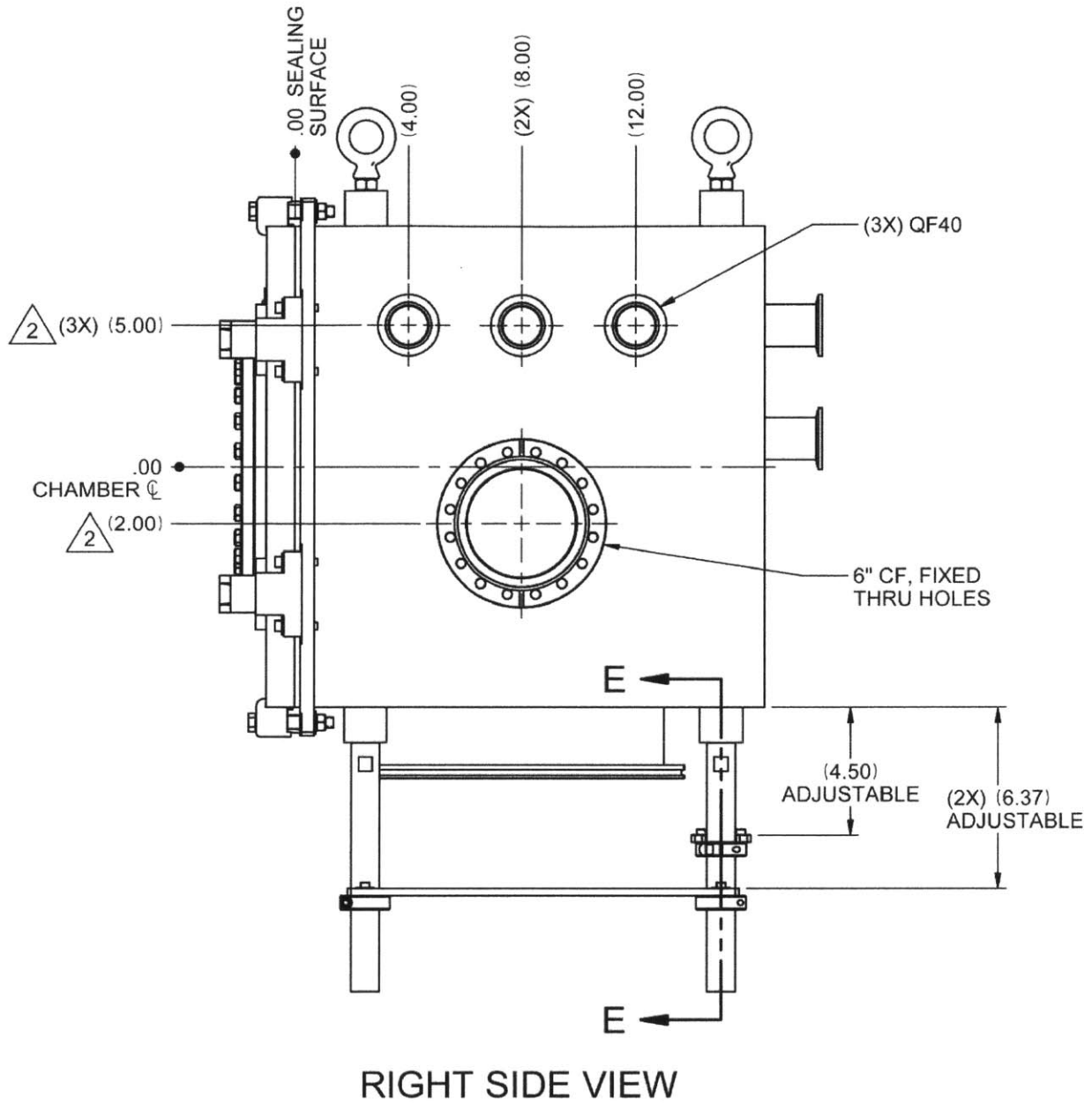
Figure A-4. oCVD reactor chamber engineering drawing—right view. Dimensions in inches.
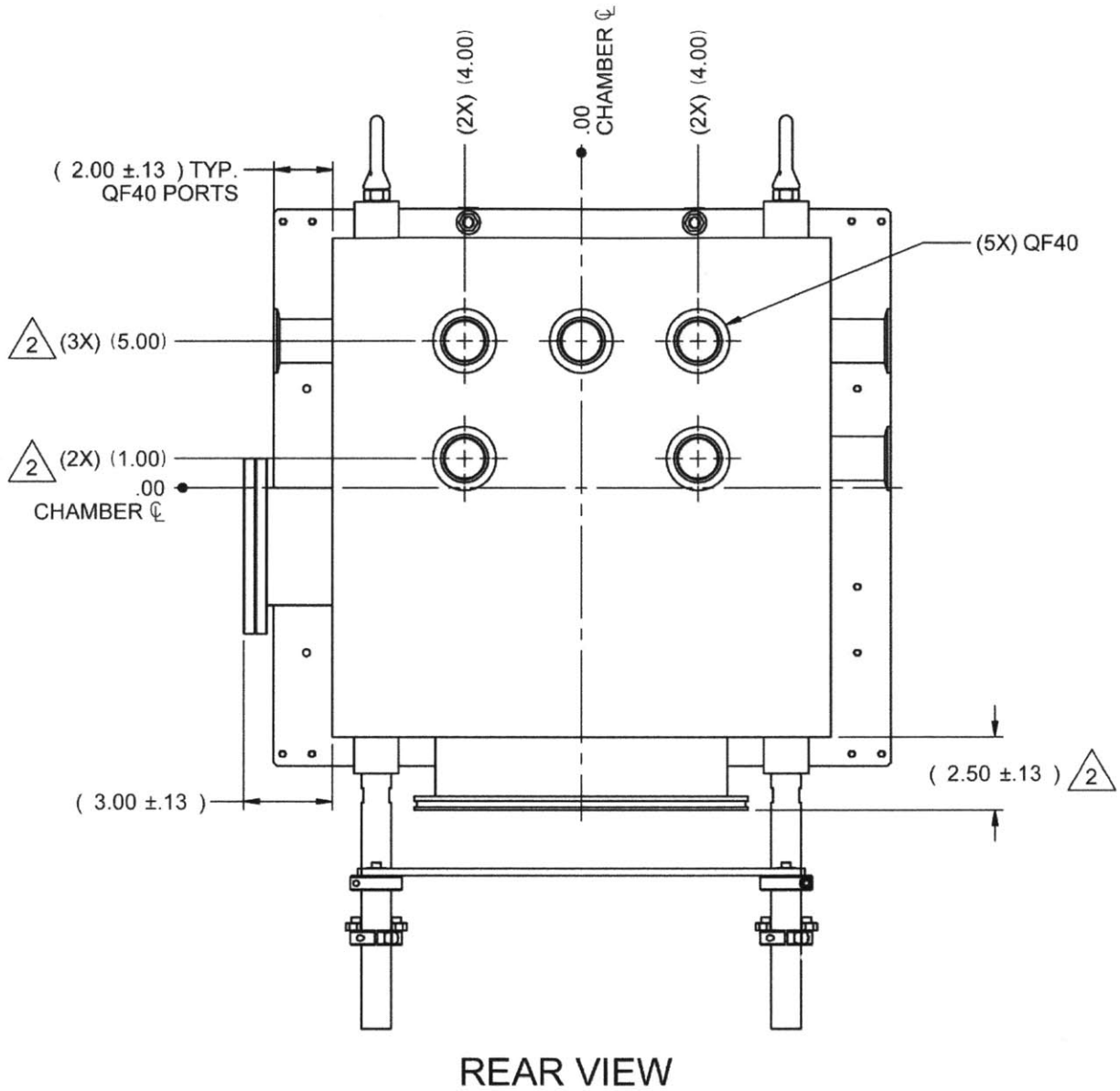
Figure A-5. oCVD reactor chamber engineering drawing—rear view. Dimensions in inches.
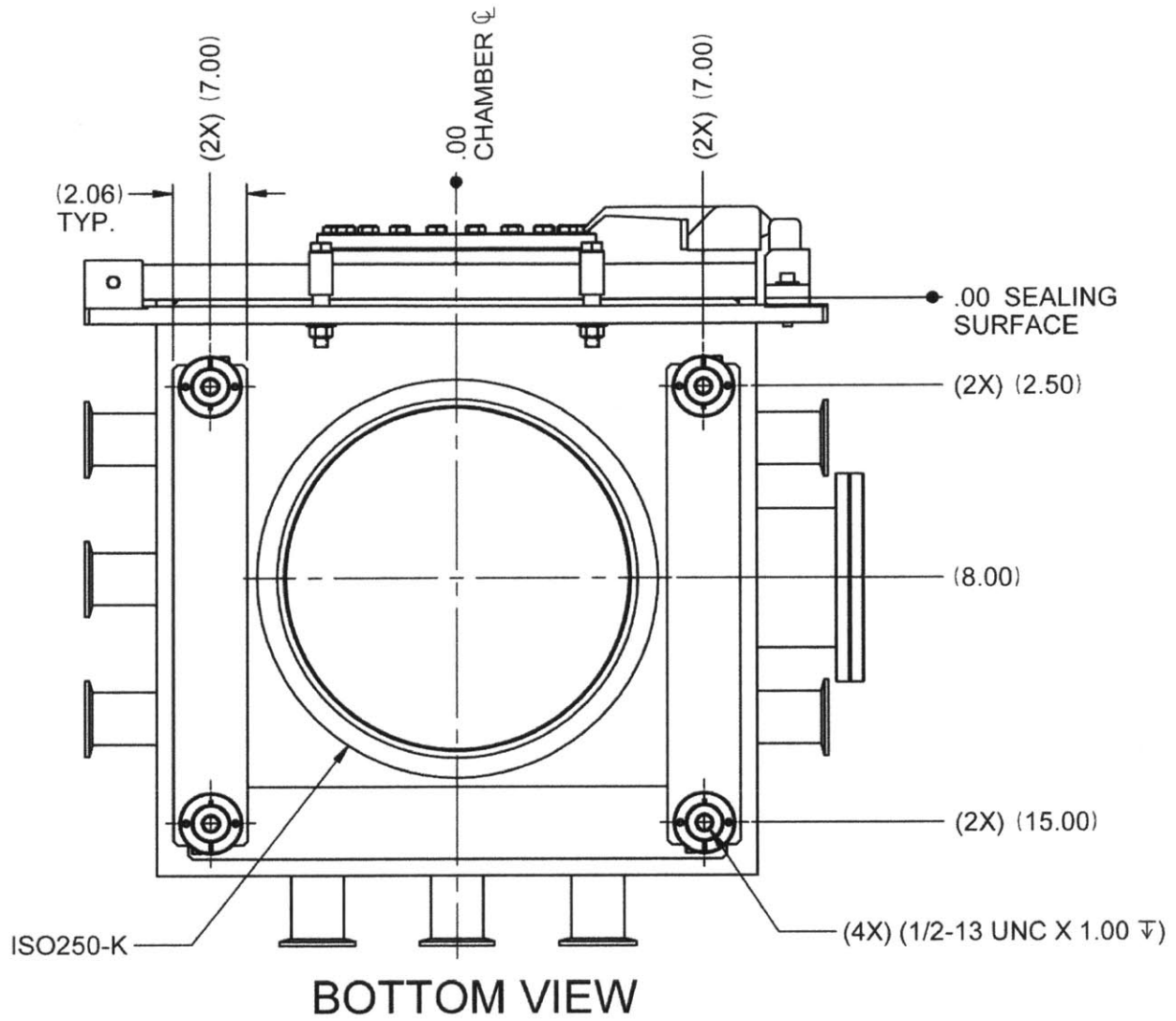
Figure A-6. oCVD reactor chamber engineering drawing—bottom view. Dimensions in inches.

(4X) (1/4-20 UNC)
INTERNAL MOUNTING
BOSSES

16.00
CHAMBER I.D.

(2X) (14.00)

(2X) (2.00)

.00 SEALING
SURFACE

8.00
CHAMBER I.D.

(2X) (6.00)

.00
CHAMBER ℄

(2X) (6.00)

8.00
CHAMBER I.D.
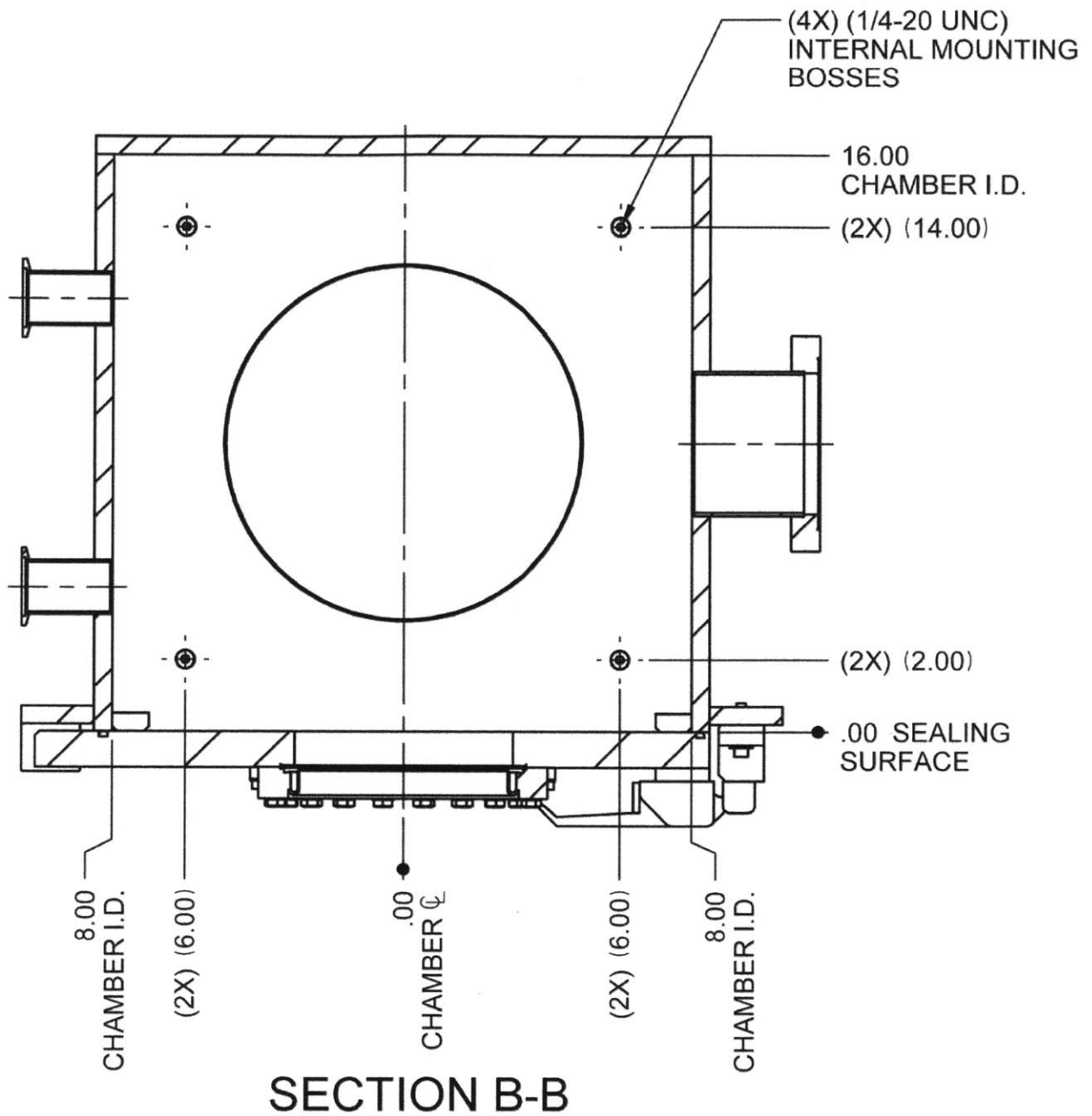
SECTION B-B

Figure A-7. oCVD reactor chamber engineering drawing—cross sectional view from top.

(.63) TOP PLATE THK.
INCREASED TO SUIT
ISO250 M/C PROFILE

SS304L DOOR
BRUSH FINISH

VPZL-800, GASKET
& HARDWARE

(15.88)
CHAMBER I.D.

SS304L CHAMBER
BRUSH FINISH
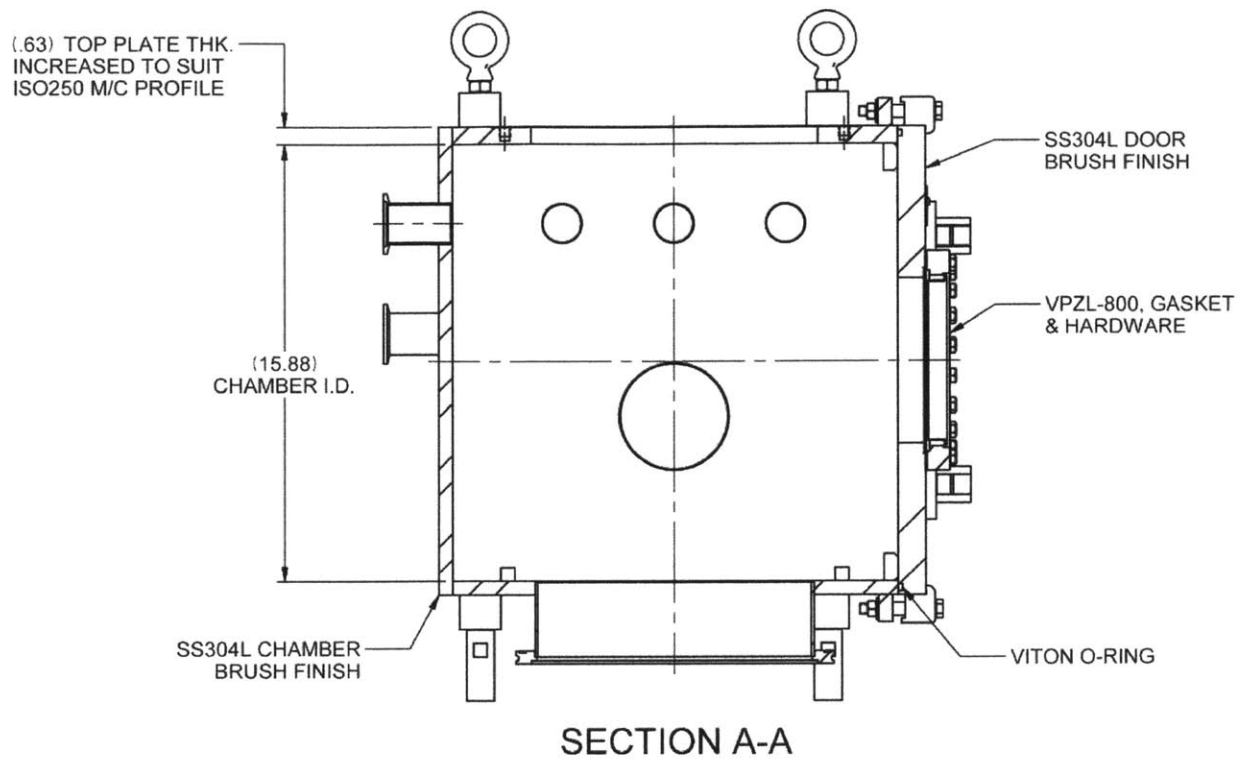
VITON O-RING

SECTION A-A

Figure A-8. oCVD reactor chamber engineering drawing—cross sectional view from left side.

BILL OF MATERIALS

| NO.	PART NUMBER	DRAWING NUMBER	DESCRIPTION	QTY	U/M
01	D-PRD095534-0500	PRD095534-0500	CHAMBER FINAL MACHINING FOR BX1616C00138	1	EA
02	D-PRD095534-66S001	PRD095534-66S001	DOOR MACHINING FOR BX1616C00138	1	EA
03	BXDRHWASSYAA	BXDRHWASSYAA	HARDWARE KIT,BOX CHAMBER DOOR ASSY	1	EA
04	O-V20/210		O-RING,VITON,20"ID X .210" CS, SPLICED	1	EA
05	DRS-27S005	DRS-27S005	LATCH MOUNTING BRACKET	1	EA
06	HCHU1032-050S4		SCREW,SOCKET HEAD CAP,SS, 10-32 X 1/2" * 50 MIN ORDER *	8	EA
07	D-A0031140	A0031140	MODIFIED LATCH ASSEMBLY	2	EA
08	BXCOMMONAH	BXCOMMONAH	LATCH CATCH MTG BLOCK	1	EA
09	WPNU010S4		WASHER,FLAT,18-8SS,#10,SAE	2	EA
10	HCHU1032-175S4		SCREW,SOCKET HEAD CAP,SS, 10-32 X 1-3/4"	2	EA
11	WPNU025S4		WASHERS, 18-8 SS, 1/4" SAE	2	EA
12	HCHU2520-125S4		SCREW,SOCKET HEAD CAP,SS 1/4-20 X 1-1/4"	2	EA
13	VPZL-800		VIEWPORT, ZERO-LENGTH, SS, 5-3/8" VIEW AREA, 8" FLANGE	1	EA
14	VZCUA150		GASKET,ANNEALED,CU,FOR 8"OD UHV FLANGE,5/PKG	1	PK
15	WPAU031S4		WASHER,FLAT,5/16", 18/8,SS, SMALL PATTERN	20	EA
16	HHBU3124-125S4		HEX BOLT,5/16-24 X 1-1/4, 18/8 SS,HHCS	20	EA
17	3067T55		LIFTING EYEBOLT W/SHOULDER, BLACK OXIDE STEEL,1/2"-13 THREAD,1-1/2"SHANK,2600# WLL	4	EA
18	NHFU5013S4		HEX NUT,1/2-13,18-8SS 3/4 WD-FLATS,7/16 HEIGHT	4	EA
19	U-ETKG1.00-L8.75-T0.50-U0.50-SC0.50		CIRCULAR POST, BLACK OXIDE STEEL, 1" OD X 8.75" LG, 1/2-13 M-F	4	EA
20	U-SCSW1.00-B0.50		SHAFT COLLAR, BLACK OXIDE STEEL, 1" BORE, 2 #10-32 TAPS	6	EA
21	D-PRD095534-01S001	PRD095534-01S001	SIDE CROSS MEMBER FOR BX1616C00138	2	EA
22	D-PRD095534-01S002	PRD095534-01S002	REAR CROSS MEMBER FOR BX1616C00138	1	EA
23	96025A147		WASHER, D-SHAPE, STEEL, NO. 10 SCREW SIZE, .63" OD, .02"-.04" THK.	12	EA
24	HCHU1032-075S4		SCREW,SOCKET HEAD CAP,SS 10-32 X 3/4"	12	EA
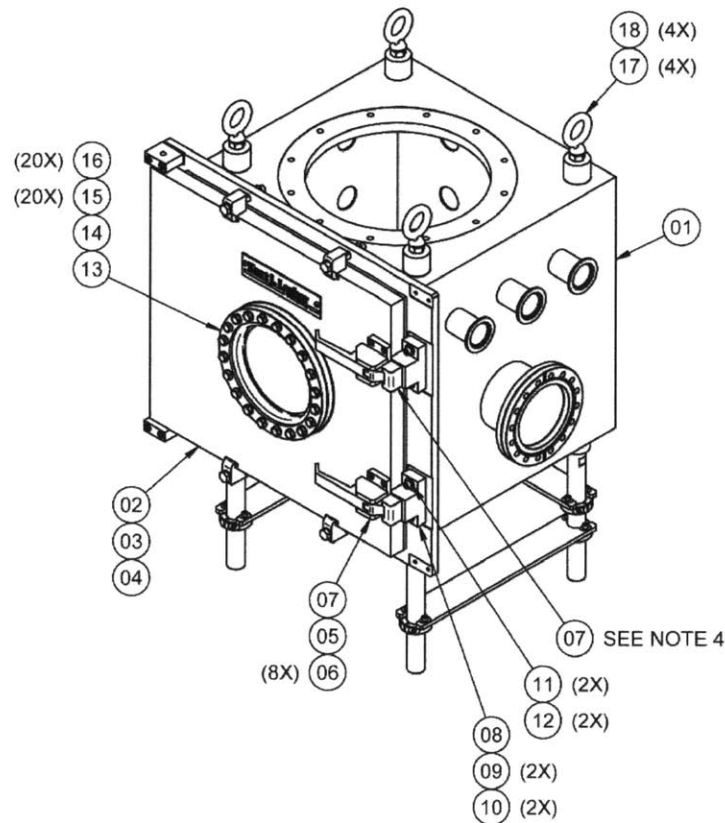
Figure A-9. oCVD react chamber engineering drawing—bill of materials.
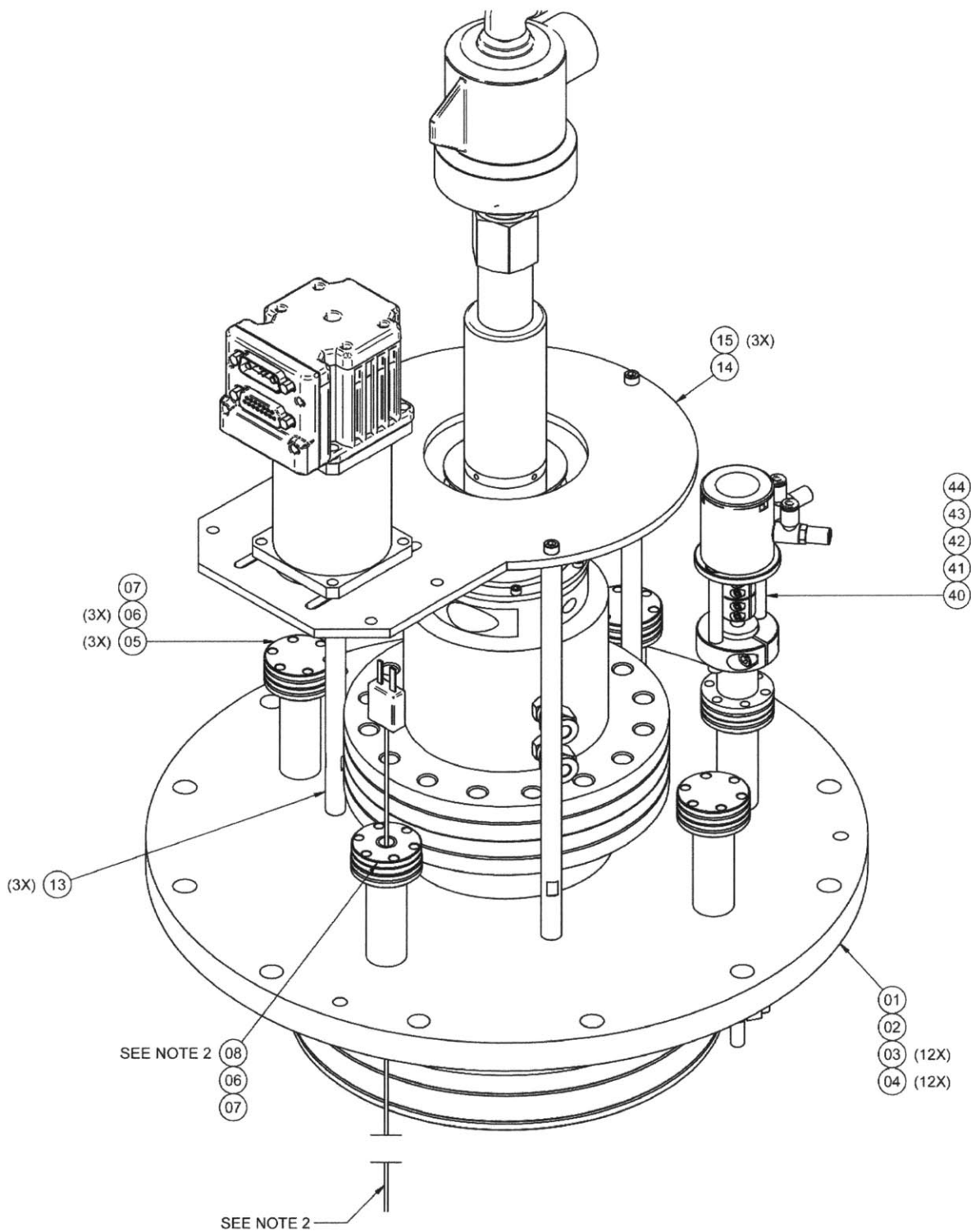
Figure A-10. Engineering drawing of top flange for oCVD reactor for rotating stage.
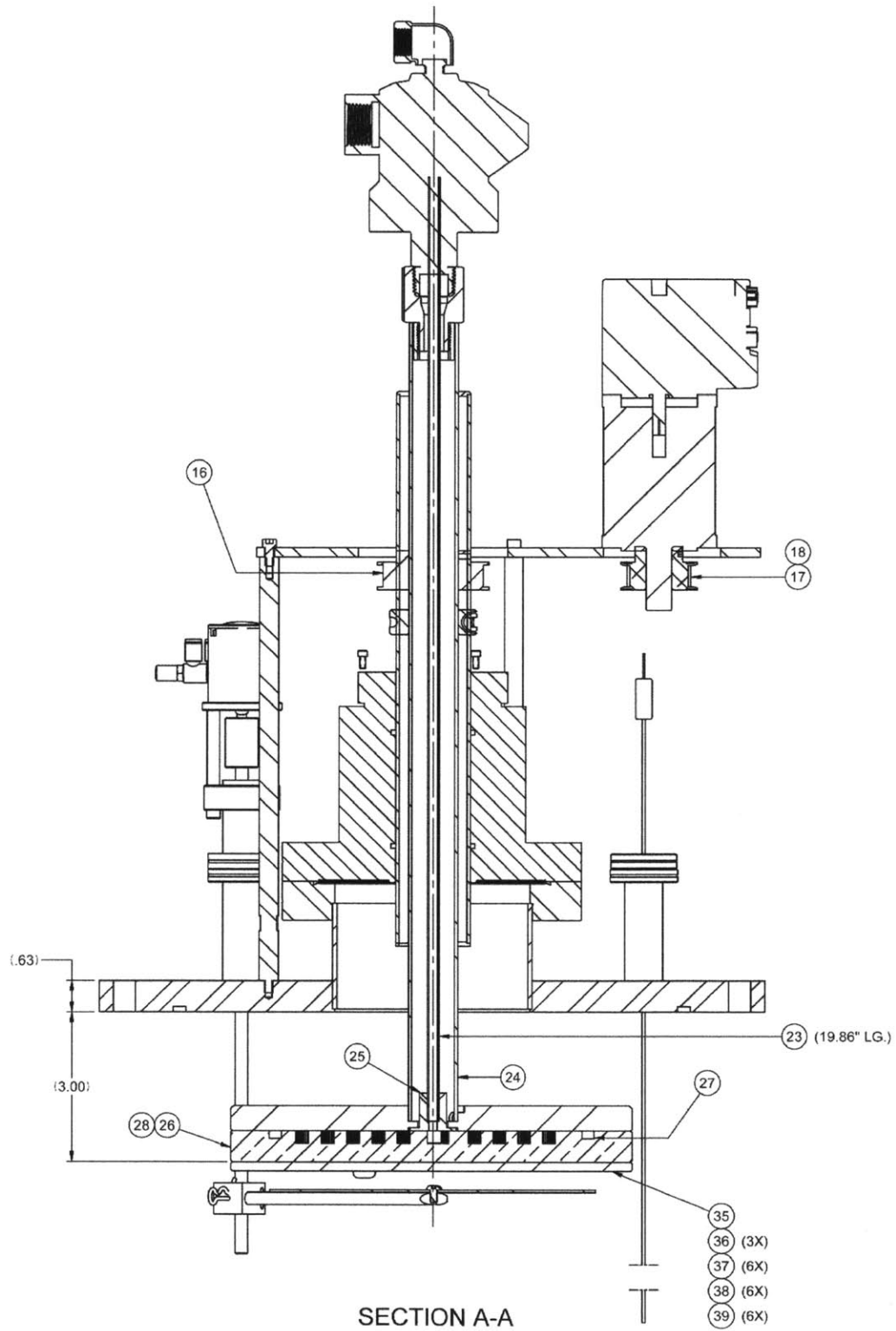
SECTION A-A

Figure A-11. Engineer drawing of top flange of oCVD reactor chamber—cross section from side.

146
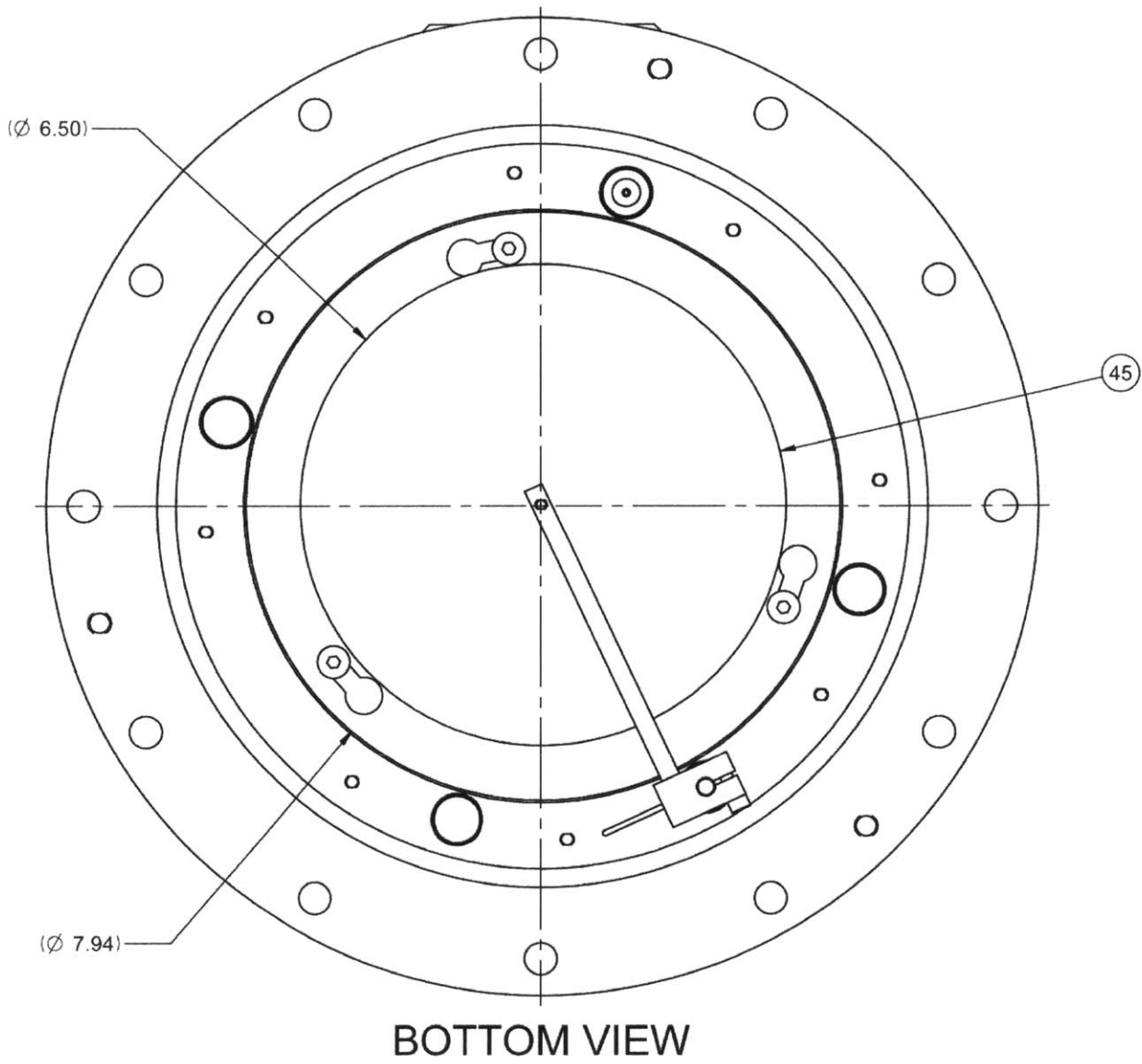
(⌀ 6.50)

(⌀ 7.94)

45

BOTTOM VIEW

Figure A-12. Engineering drawing of top flange of oCVD reactor chamber for stage—bottom view.
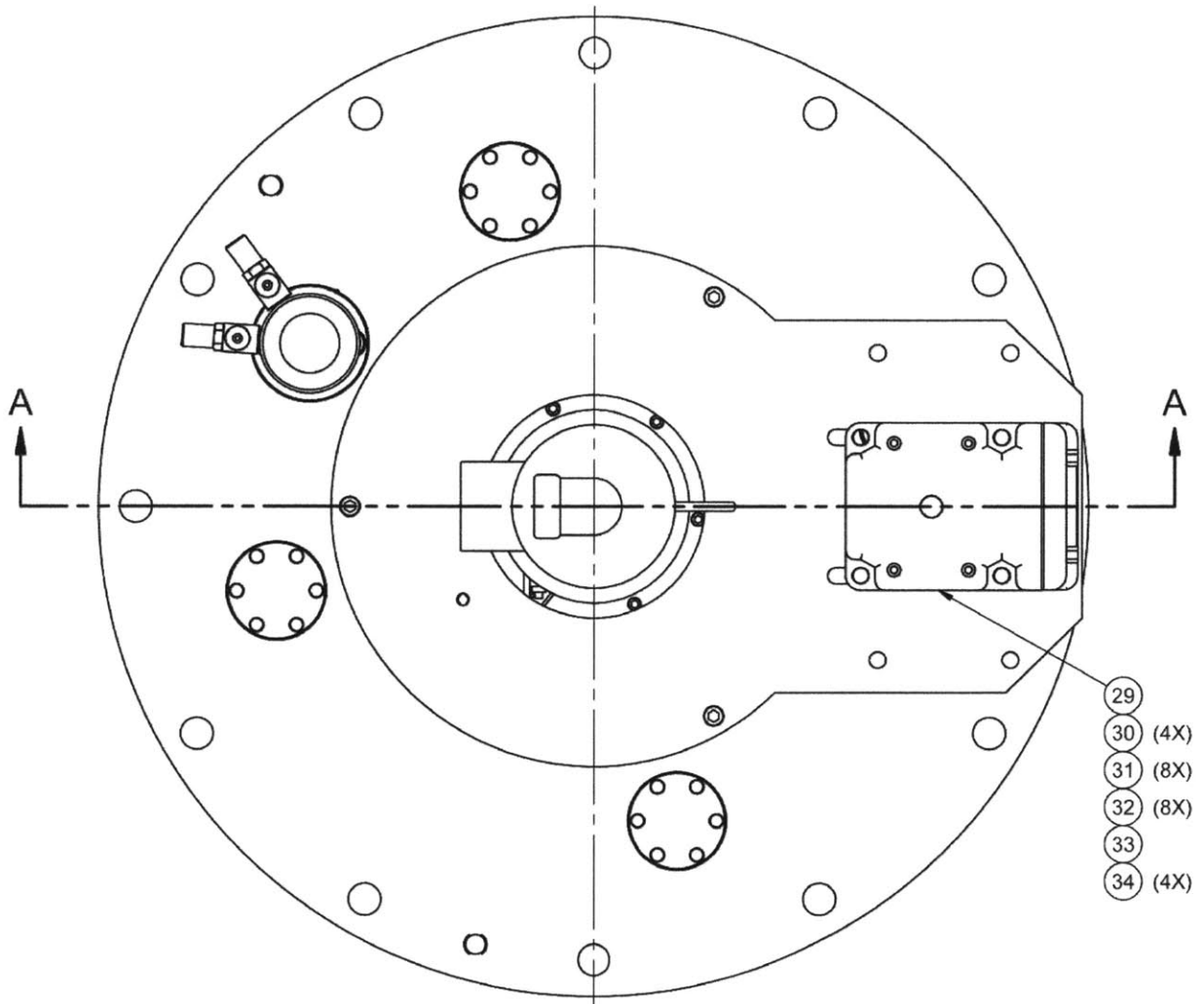
147

Figure A-13. Engineering drawing of top flange of oCVD reactor chamber for stage—top view.

BILL OF MATERIALS

NO.	PART NUMBER	DRAWING NUMBER	DESCRIPTION	QTY	U/M
01	D-A0041245	A0041245	TOP PLATE WELDMENT	1	EA
02	QF250-AAVR		CENTERING RING, QF250, AL INNER, AL OUTER, VITON O-RING	1	EA
03	HHBM1015-030S4		HEX BOLT, SS, M10 X 30 1.5 PITCH	12	EA
04	WPNM100S4		WASHER,FLAT,M10,18-8 SS, DIN 433	12	EA
05	F0133X000N	P0000036	FLANGE,UHV,SS,BLANK,FIXED, 1.33"OD	3	EA
06	GA-0133I	P0001073	COPPER GASKET FOR MINI FLANGE GA-0133	5	EA
07	PNB-0133		PLATE N & B SET, (24) 8-32X.75 SS SHCS, (12) PLATE NUTS	2	EA
08	TFP1KYSS122	A0035104	T/C PROBE,(1)TYPE K,SS SHEATH,1.33"UHV,12"LG	1	EA
09	KLFDHCF150600W		F/T, ROTARY, 1-1/2" HOLOOW SHAFT, 6"UHV FLANGE	1	EA
10	GA-0600I	P0001080	GASKET, COPPER, 6" FLANGE, 4.743"OD,4.006"ID,1/PKG	1	EA
11	HBS31224225		HEX B,N,&W SET,(25)5/16-24 X 2-1/4 FOR 6R,6-3/4",8"FLANGES	1	PK
13	L0018819		CIRCULAR POST,3/8"OD X 9.35"LG 8-32 M-F	3	EA
14	D-PRD095536-07S005	PRD095536-07S005	MOTOR MOUNTING PLATE	1	EA
15	HCHU0832-038S4		SCREW,SOCKET HEAD CAP,SS 8-32 X 3/8"	3	EA
16	PLA-28S020	PLA-28S020	PULLEY,XL,32 TEETH,0.37" BELT, W/HUB, 1.00"DIA THRU BORE,2FL	1	EA
17	PLA-28S073		PULLEY,TIMING,AL,20 GROOVES,1/2" BORE,KEYED	1	EA
18	A6G3-070037		TIMING BELT, 0.2" PITCH, 3/8" WIDE, 70 GROOVES	1	EA
19	U-SSCDN1.00		SHAFT COLLAR,"D"SHAPE,SPLIT, 1.00 BORE,8-32 TAPPED HOLES	1	EA
20	D-A0033929	A0033929	ROTATION HOME SWITCH ASSEMBLY, 1/4" POST	1	EA
21	4064832SS0		STANDOFF,SS,M/F 8-32,1/4"OD X 2-3/4"LG	1	EA
22	N12-023-214-701		FEEDTHROUGH, LIQUID, ROTARY DEUBLIN/1/2"NPT, DUOFLOW	1	EA
23	SST-0025CI		TUBING,316L SST,RIGID,1/4"OD, .035"WALL,ELECTROPLSH,PER INCH	19.86	IN
24	D-PRD095536-07S001	PRD095536-07S001	PLATEN WELDMENT	1	EA
25	PLA-A-0827	PLA-A-0827	SUPPLY TUBE GUIDE	1	EA
26	D-PLA-B-0825	PLA-B-0825	WATER COOLED PLATEN BLOCK	1	EA
27	O-V361		O-RING,VITON,5.975"ID X .210"W (ACT),6"ID X 3/16"W (NOM)	1	EA
28	HCHU2528-100S4		SCREW,SOCKET HEAD CAP,SS 1/4-28 X 1.0"	3	EA
29	SM2315D		SMARTMOTOR	1	EA
30	HCHU1032-075S4		SCREW,SOCKET HEAD CAP,SS 10-32 X 3/4"	4	EA
31	NHFU1032S4		NUT, HEX, 18-8, SS, 10-32 X 3/8 WD-FLATS, 1/8 HEIGHT	8	EA
32	WSSU010S4		WASHER, LOCK, SS, #10	8	EA
33	23PN0100		CGI PARAGON, PLANETARY GEARHEAD, SIZE 23, 10:1 RATIO	1	EA
34	HBHU1032-075S4		SCREW, BUTTON HEAD CAP, SS, 10-32 X 3/4"	4	EA
35	D-P0034004	P0034004	PVD75 SINGLE SUBSTRATE HOLDER, WATER COOLED	1	EA
36	HBHU2528-050S4PV		SCREW,BUTTON HEAD CAP,SS, 1/4-28 X 1/2",VENTED,AG PLATED	3	EA
37	SHA-08S003	SHA-08S003	SUBSTRATE CLIP	6	EA
38	HCHU0440-013S4P0		SCREW,SOCKET HEAD CAP,SS, 4-40 X 1/8",AG PLATED	6	EA
39	WPNU004S4		WASHER,FLAT,18-8,SS,SM PATTERN 4.0 X 1/8 ID,5/16 OD, 1/32 NO	6	EA
40	D-A0031598	A0031598	FERRO / ROTARY ACTUATOR ASSEMBLY, 1/4" SHAFT,1.33" CF, SMC	1	EA
41	GA-0133I	P0001073	COPPER GASKET FOR MINI FLANGE GA-0133	1	EA
42	PNB-0133		PLATE N & B SET, (24) 8-32X.75 SS SHCS, (12) PLATE NUTS	1	EA
43	S51FCZ-250250		COUPLING,SS,1/4" X 1/4"BORE, 1PC,RIGID,LOW PROFILE, FAIRLOC	1	EA
44	U-SSFR0.25-L7.00	P0037732	ROTARY SHAFT,304SS,1/4"OD X 7"LG	1	EA
45	D-A0041247	A0041247	SHUTTER ASSEMBLY, SS, A-6.50", B-4.38", C-.25", PVD75	1	EA

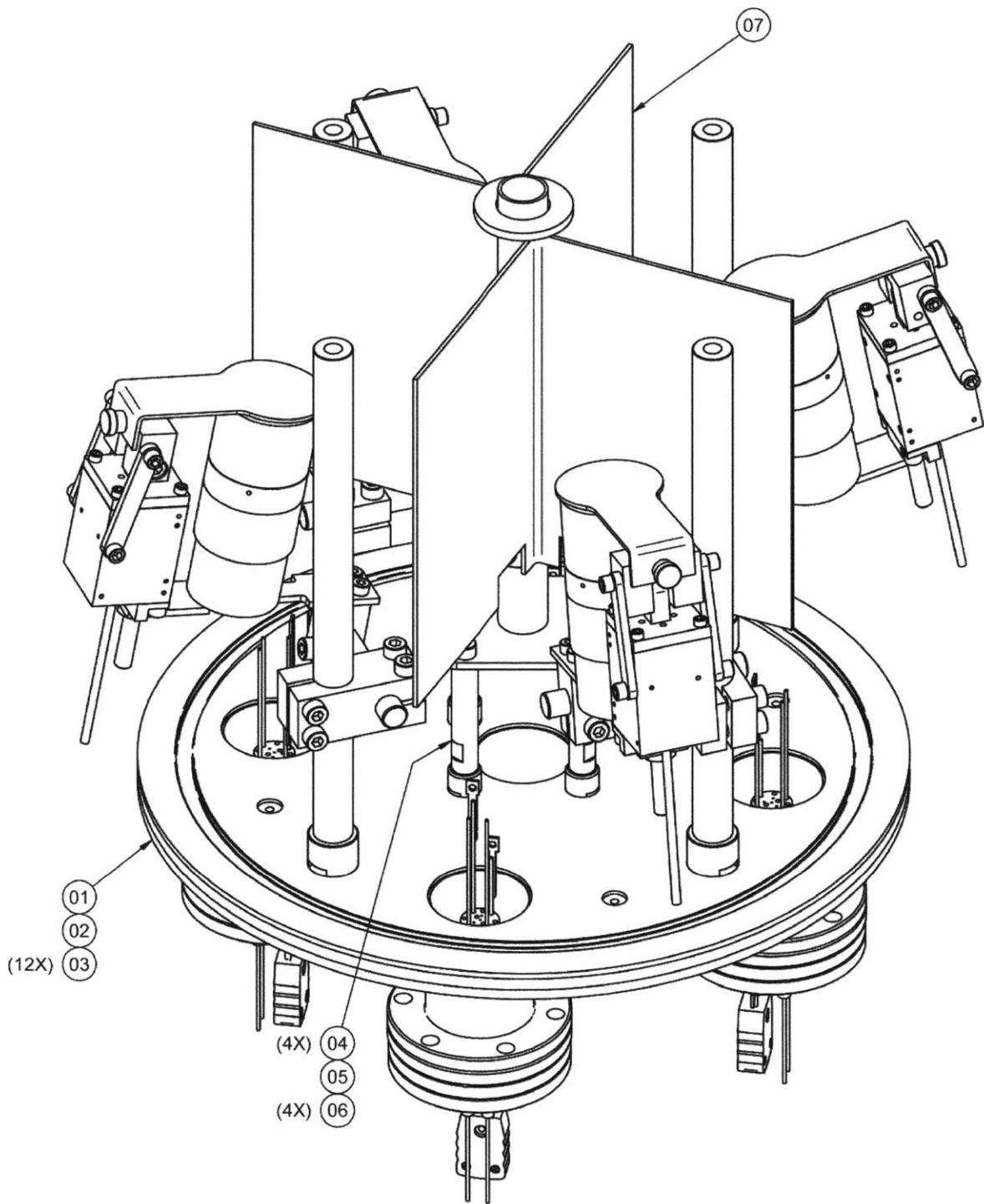**Figure A-14.** Bill of materials for top flange of oCVD reactor chamber for stage.

Figure A-15. Engineering drawing of oCVD reactor bottom flange evaporation sources.
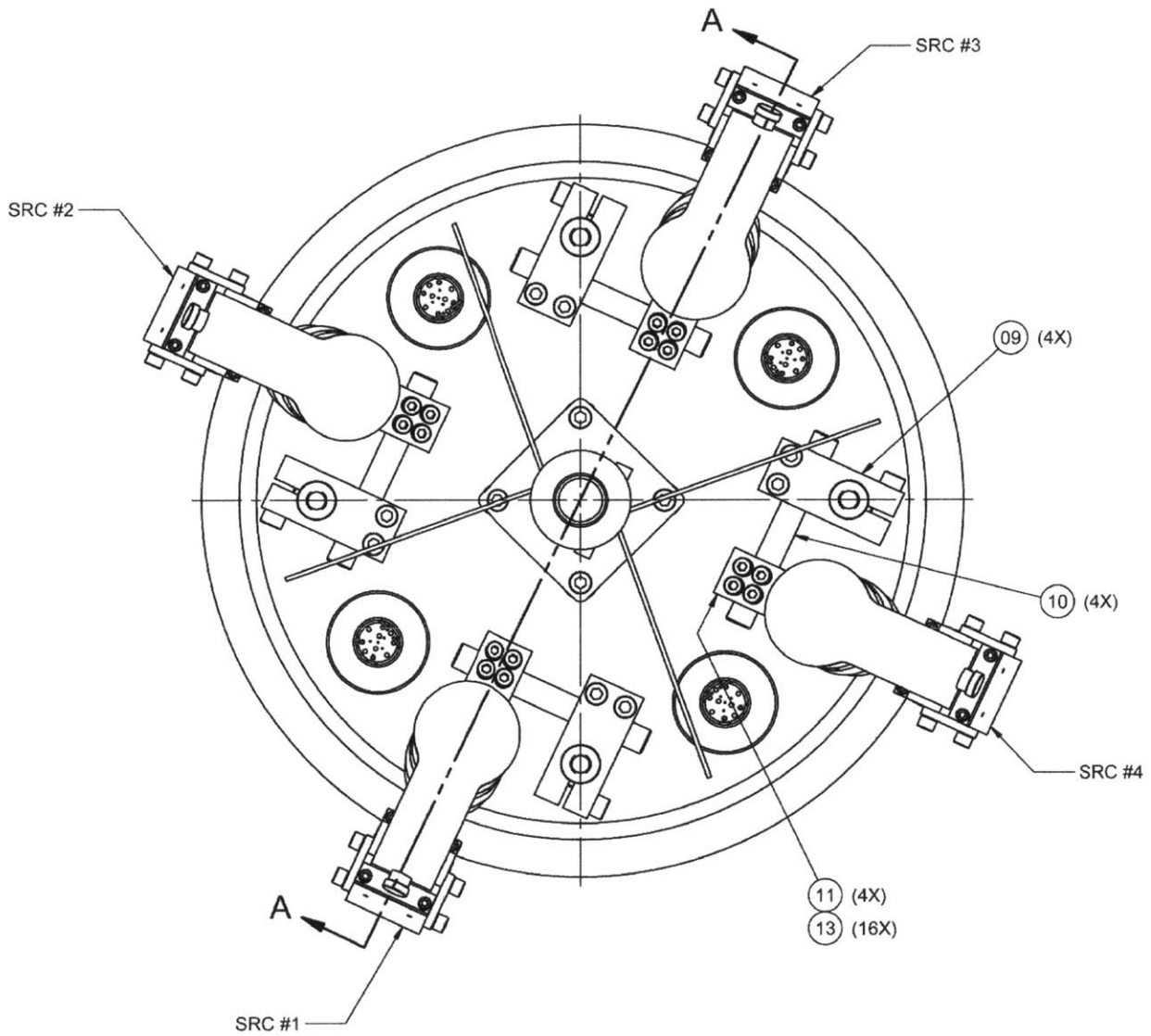
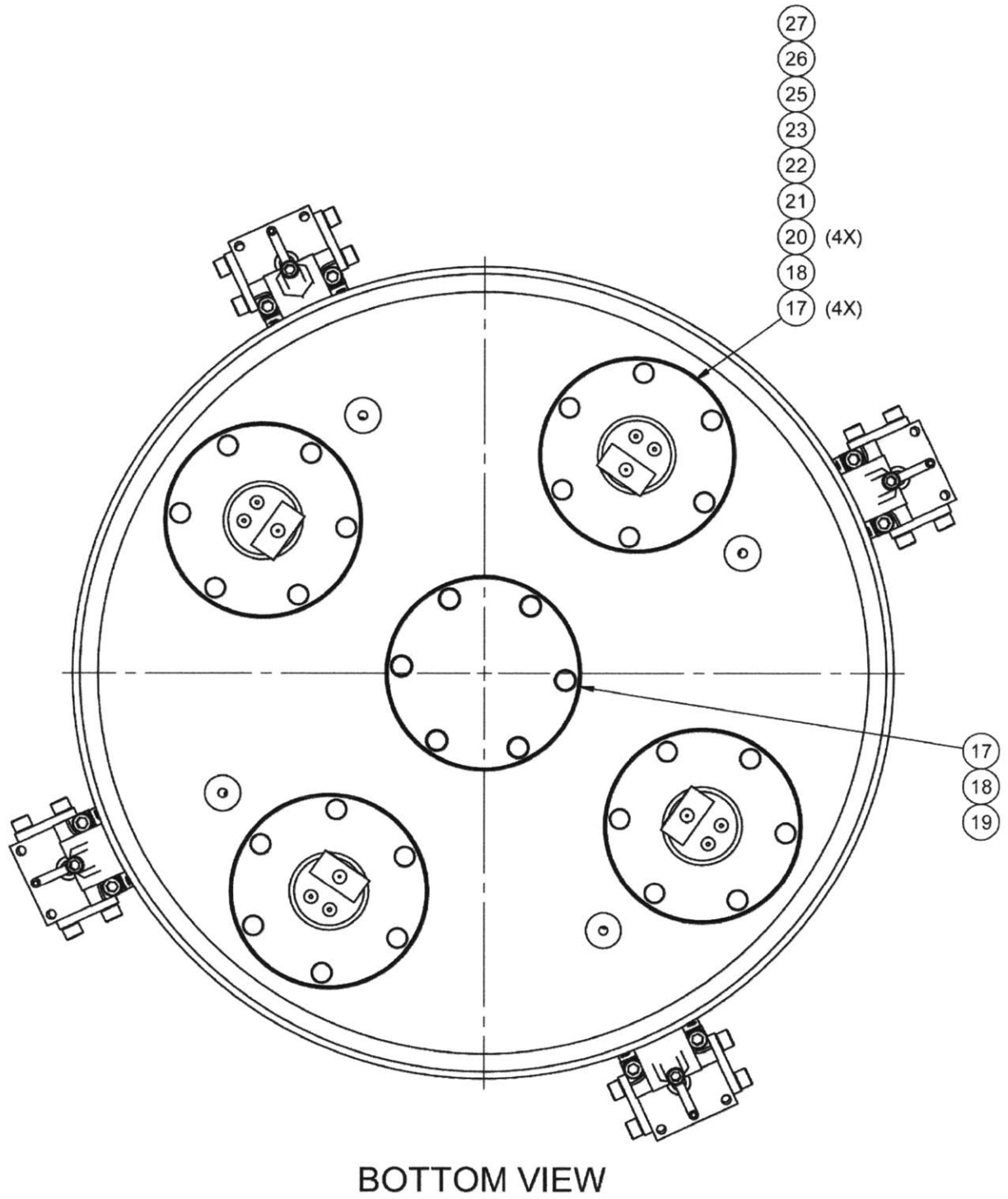**Figure A-16.** Engineering drawings for oCVD reactor bottom flange with evaporation sources—top view.

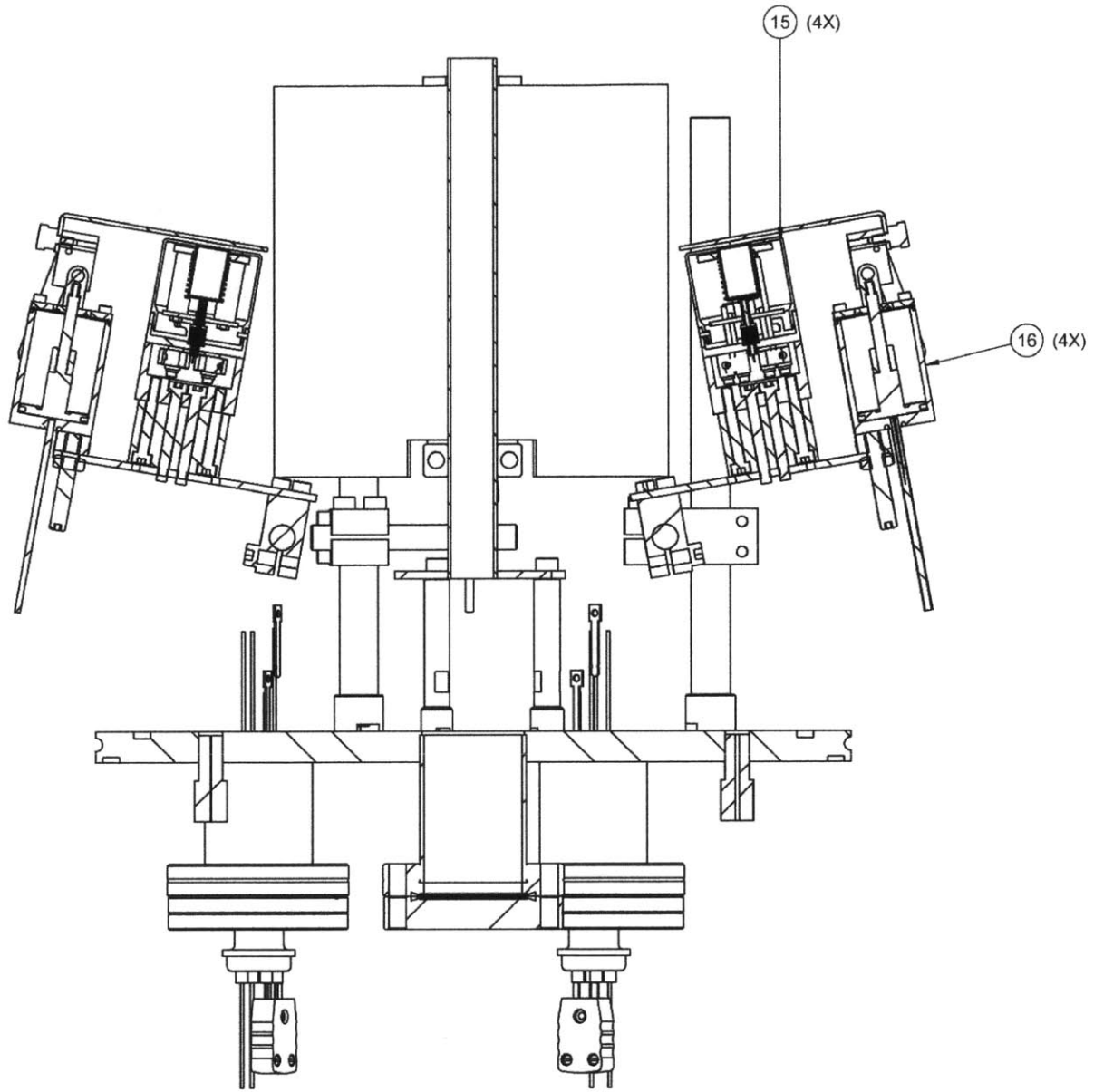**BOTTOM VIEW**

Figure A-17. Engineering drawing for oCVD reactor bottom flange with evaporation sources—bottom view.

SECTION A-A

Figure A-18. Engineering drawing of oCVD chamber bottom flange with evaporation sources—cross sectional view.

BILL OF MATERIALS

NO.	PART NUMBER	DRAWING NUMBER	DESCRIPTION	QTY	U/M
01	D-A0041260	A0041260	LTE FLANGE WELDMENT	1	EA
02	QF250-AAVR		CENTERING RING, QF250, AL INNER, AL OUTER, VITON O-RING	1	EA
03	QF-SDC-AL2	PMF-HARD-264	CLAMP, DOUBLE CLAW, ALUMINUM, FOR 160-250 ISO FLANGES	12	EA
04	SETGR10-50		STANDOFF,10MM OD X 50MM LG,M5 MXF THREADS,SS	4	EA
05	D-A0015256	A0015256	CENTER ROD WELDMENT	1	EA
06	HCHM0508-012S4PV		SCREW,SOCKET HEAD CAP,SS, M5 X 12,VENTED,AG PLATED	4	EA
07	D-A0015016	A0015016	CENTER SHIELD WELDMENT	1	EA
08	SETGRF15-225		STANDOFF,15MM OD X 225MM LG,M8 MXF THREADS,SS	4	EA
09	SLKLN15-10		STRUT CLAMP,15MM X 100MM HOLE CROSS TYPE,SS	4	EA
10	SSFJ10-80		SHAFT,10MM OD X 80MM LG,SS,G6	4	EA
11	SQM10		STRUT CLAMP,10MM HOLE,PARALLE TAP,M4,SS	4	EA
12	PVD75RMBRH	P0015253	BRACKET,REAR MOUNTING,1CC, 10CC AND 35CC LTE HEAD, SHUTTER M	4	EA
13	HCHM0407-010S4PV		SCREW,SOCKET HEAD CAP,SS, M4 X 10,VENTED,AG PLATED	16	EA
15	LTE01CC		1CC LTE SOURCE AND BASE COMP. TO DRG OLED002000 R2 ECN 1803	4	EA
16	D-A0041292	A0041292	SHUTTER ASSEMBLY, 1cc (5cc) LTE	4	EA
17	GA-0275I	P0001075	GASKET, COPPER, 2-3/4" FLANGE, 1.895"OD, 1.451"ID	5	EA
18	HBS25028138		HEX B,N,&W SET,(25)1/4-28X1.38 FOR 2-1/8 AND 2-3/4" FLANGES	2	EA
19	F0275X000N	P0000084	FLANGE,UHV,SS,BLANK,FXD,2.75" OD	1	EA
20	TFT1KY2C303	A0004581	T/C F/T,1PR TYPE K,W/CONN PLUG (2).094"CU COND,30A,2.75"UHV	4	EA
21	VZTT-K-24		WIRE,T/C,SOLID,TYPE K,TEFLON INSULATED,24 AWG,PER FOOT	6	FT
22	FTATC062A		CRIMP-PUSH TYPE THERMOCOUPLE CONNECTOR,ALUMEL,5/PKG	1	EA
23	FTATC062C		CRIMP-PUSH TYPE THERMOCOUPLE CONNECTOR, CHROMEL, 5/PKG	1	EA
25	FTACERB116		CERAMIC BEADS,STEATITE,BALL & SOC.260"OD,.116"ID,54/PKG PER	3	PK
26	FTAIBC120		INLINE BARREL CONNECTOR,10/PKG .120"ID,.56" LONG,25A,Be-CU	1	EA
27	18798		HEAT SHRINK TUBING, PTFE 2:1, EXPANDED I.D. .140, RECOVERED	2	EA
28	D-PRD095535-1800	PRD095535-1800	CONNECTION DIAGRAM	1	EA

Figure A-19. Bill of materials for bottom flange of oCVD chamber for evaporation sources.
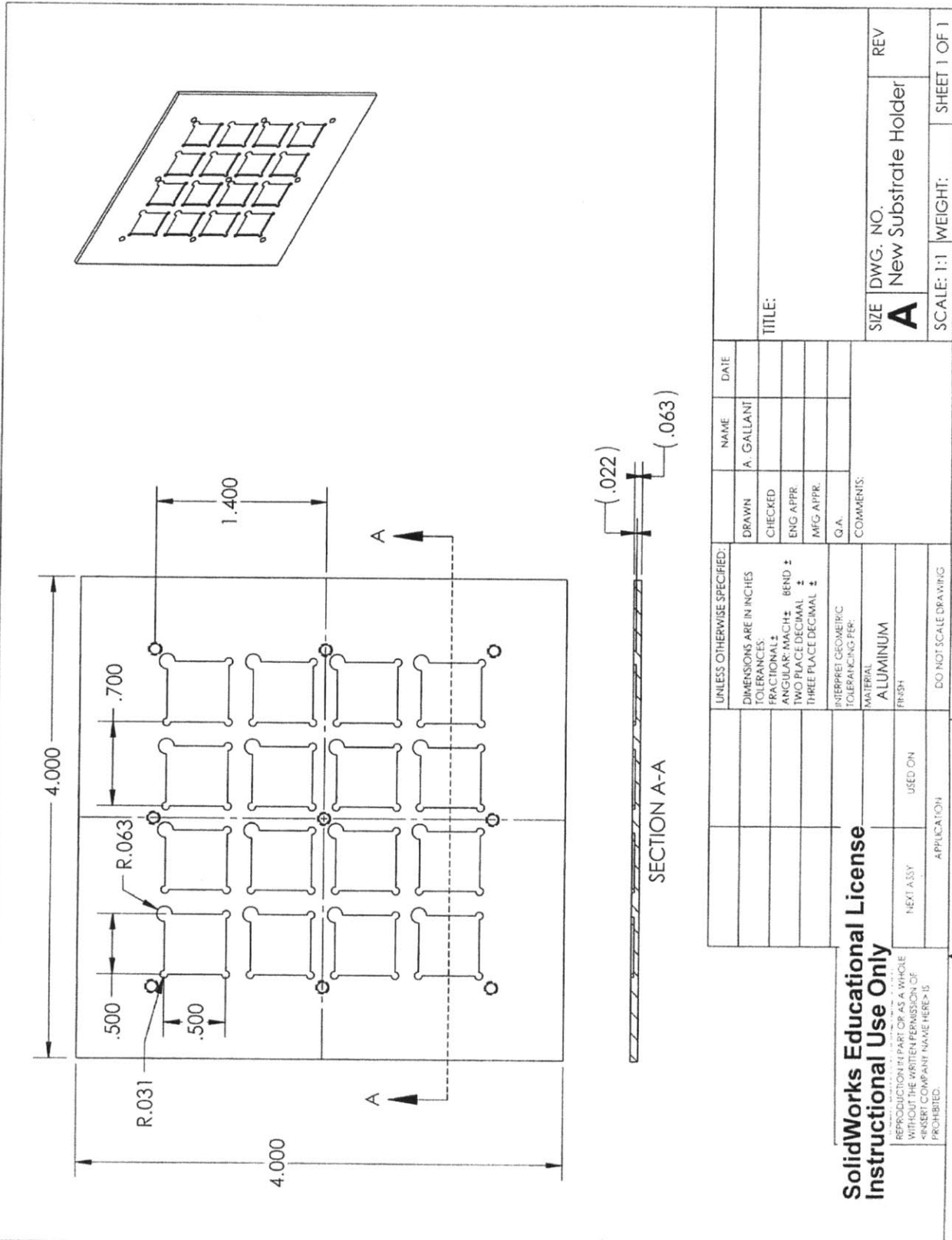
Figure A-20. Engineering drawing for ITO sample holder for oCVD semiconductor polymers.